PhD Thesis

Determination of the molecular architecture and the mechanism of self-assembly of Dynamin1 protein machine

Javier Vera Lillo

Supervisor: Dr. Vadim Frolov Buyanov

Leioa 2021

(c)2021 Javier Vera Lillo

Contents

List of abbreviations

<I>	Average fluorescence intensity
AFM	Atomic Force Microscopy
$AlCl_3$	Aluminium Chloride
BCA	Bicinchoninic Acid
Biotin PC	1-oleoyl-2-[12-biotinyl(aminododecanoyl)]-sn-glycero-3-phosphocoline
BSA	Bovine Serum Albumin
BSE	Bundle signaling element
CCPs	Clathrin coated pits
Chol	Cholesterol
CME	Clathrin-mediated endocytosis
Cryo-EM	Cryo Electron Microscopy
CVD	Chemical vapor deposition
DOPC	1,2-dioleoyl-sn-glycero-3-phosphocholine
DOPS	1,2-dioleoyl-sn-glycero-3-phospho-L-serine
DRP	Dynamin-related protein
Dyn1	Dynamin1
Dyn1-mEGFP	Dynamin1-monomeric Enhanced Green Fluorescent Protein
Dyn2	Dynamin2
Dyn3	Dynamin3
EDTA	Ethylenediaminetetracetic acid solution
EGTA	Ethylene glycol-bis(2-aminoethylether)-N,N,N’,N’-tetraacetic acid

EM	Electron microscopy
FP	Fluorescent protein
FRAP	Fluorescence Recovery After Photobleaching
GDP AlF_{4-}	Guanosine 5’-diphosphate aluminium fluoride
GDP	Guanosine 5’-diphosphate
GED	GTPase effector domain
GFP	Green Fluorescent Protein
GMPPCP	β,γ-Methyleneguanosine 5’-triphosphate
GSBs	Giant Suspended Bilayers
GTP	Guanosine 5’-triphosphate
GTPγS	Guanosine 5'-O-[gamma-thio]triphosphate
GUVs	Giant Unilamellar Vesicles
HEPES	4-(2-hydroxyethyl)-1-piperazineethanesulfonic acid
HS-AFM	High Speed Atomic Force Microscopy
HyD	Hybrid Detector
KCl	Potassium Chloride
LUVs	Large Unilamellar Vesicles
mEGFP	monomeric Enhanced Green Fluorescent Protein
$MgCl_2$	Magnesium Chloride
MLVs	Multilamellar vesicles
N&B	Number and Brightness
NaF	Sodium Fluoride
NTs	Lipid Nanotubes
PBS	Phosphate-buffered saline

PDMS	Poly-(dimethyl)siloxane
PET	Photo-induced electron transfer
PH domain	Pleckstrin homology domain
$PI(4,5)P_2$	L-α-phosphatidylinositol-4,5-bisphosphate
Pi	Inorganic Phosphate
PNTs	Peptoid Nanotubes
PRD	Proline-rich domain
Qdots	Quantum dots
r^2	Square displacement
ROI	Region of interest
SH3 domain	Src Homology 3 Domain
SiNW	Silicon NanoWires
SLBs	Supported Lipid Bilayers
SM	Single-Molecule
SMrTs	Supported membrane tube assay system
SPT	Single particle tracking
SUPER	Supported bilayers with excess membrane reservoir
SUVs	Small unilamellar vesicles
TIR-FM	Total Internal Refelection Fluorescence Microscopy
TR-DHPE	Texas Red™ 1,2-Dihexadecanoyl-sn-Glycero-3-Phosphoethanolamine
usNT	Ultra-short lipid nanotubes
VL	Variable loop
WT	Wild type
ε	Molar extinction coefficient

λ	Wavelength
σ^2	Fluorescence intensity variance
ϕ	Quantum yield

Chapter 1:

Introduction

We are all born in the deepest darkness. As we grow up, the first flashes appear. Later on, these flashes become our first lights. These lights represent the knowledge acquired from what surrounds us. Some people just stay in the light. Others, however, go into the shadows trying to light a candle. These people in charge of lighting up the world are scientists.

I have spent the last four years in the dark, trying to find a candle. I think I lighted it. Do you want to see what is in the light?

Dynamin1, the membrane fission machinery of endocytosis.

The plasma membrane is a highly dynamic structure that functions as a selective barrier between the intracellular space and the extracellular environment (Goñi, 2014). This smart interface is responsible for the regulation and organization of the material fluxes going in and out of the cell (Cheung and De Vries, 2008). How the molecular nutrients, solutes and particles enter the cell depends on their size. Protein pumps and channels integrated into the plasma membrane let sugars, ions, and amino acids in (Singh and Bal, 2017). The internalization of bigger molecular structures and the solute uptake is generally driven by membrane-bound vesicles, which, upon formation, have to be pinched-off the plasma membrane. This transport pathway utilizing membrane vesicles is called endocytosis (Conner and Schmid, 2003). Operating at a cellular level, endocytosis is deeply integrated in the tissue functionalities, playing a fundamental role in the immune response, neurotransmission, intercellular communication, and, ultimately, in the development and homeostasis of the whole organism (Mettlen *et al*., 2009). To date, various and often complex endocytic pathways have been identified. Out of them, clathrin-mediated endocytosis (CME) is the best understood (Liu *et al*., 2011a).

This endocytic pathway is characterized by the formation of a protein cage around the emerging vesicle. The cage is formed by clathrin triskelia self-assembled into a polyhedral lattice. The clathrin subunits are recruited from cytosol during the vesicle formation. Exactly how the clathrin cage deforms and stabilizes membrane invaginations, known as clathrin coated pits (CCP), remains a subject of active research (Wang *et al*., 2020). However, it is generally recognized that clathrin on its own cannot robustly produce CCP and relies on the specialized assembly proteins (APs) (Brodsky *et al*., 2001; Kirchhausen, 1999). These two coat constituents are both necessary and sufficient for the membrane invagination and vesicle formation. Once the CCP formation is completed, the nascent clathrin-coated vesicle (CCV) remains connected to the parent membrane through a thin lipid structure or membrane neck (Frolov *et al*., 2015). To complete the process of the vesicle formation this lipid structure has to be broken (Figure 1.1. A). The breakage, or scission of the neck, requires a dedicated protein machinery because of the following reasons. First, the scission is to be coordinated with the maturation of the CCP, completion of the coat formation and cargo packaging (Wang *et al*., 2020). Second, in various membrane processes the scission has to happen instantly and hence is to be enforced by a protein machinery (Schmid and Frolov, 2011). Third, the membrane remodelling during scission is to respect the membrane barrier function, that is, membrane poration and leakage are to be avoided (Schmid and Frolov, 2011).

All of these requirements are met by Dynamin1 scission machinery, the main subject of this work. Dynamin1, the 100 kDa GTPase, is the founding member of a family of large GTPases, the multidomain proteins deeply implicated in membrane remodelling processes, both fusion and fission, inside the cell (Antonny *et al*., 2016; Ferguson and De Camilli, 2012; Schmid and Frolov, 2011). This superfamily can be divided into two groups, dynamin-related proteins (DRPs), and classical dynamins (Praefcke and McMahon, 2004). Three different, tissue-specific isoforms of classical dynamins (Dynamins hereafter) are present in mammalian cells, Dynamin 1 (Dyn1), Dynamin 2 (Dyn2), and Dynamin 3 (Dyn3) (Cook *et al*., 1996; Urrutia *et al*., 1997). Dyn1 is mainly expressed in neurons and is primarily implicated in clathrin-mediated endocytosis (Ferguson *et al*., 2007). Dyn1 is associated with CCPs from the very beginning of their emergence and controls their further progress to CCV (Figure 1.1 A, (Wang *et al*., 2020)). It performs the scission only when the curvature of the CCV neck becomes high, signalling the readiness of the CCV (Mettlen *et al*., 2018; Schmid and Frolov, 2011). The high curvature of the neck triggers self-assembly of Dyn1 into a mechano-active helical complex surrounding the neck (Figure 1.1A, B, (Antonny *et al*., 2016)). GTP hydrolysis fuels constriction of the helix causing fast and robust membrane scission ((Antonny *et al*., 2016), Figure 1.1 B). The helix constriction is organized in time and space to direct the membrane remodelling to the leakage-free hemi-fission pathway of lipid rearrangements (Campelo and Malhotra, 2012; Mattila *et al*., 2015). This functional understanding of Dyn1, yet uncomplete, took several decades of intense research to obtain. Before highlighting the remaining problems, we will briefly outline the history of dynamin research.

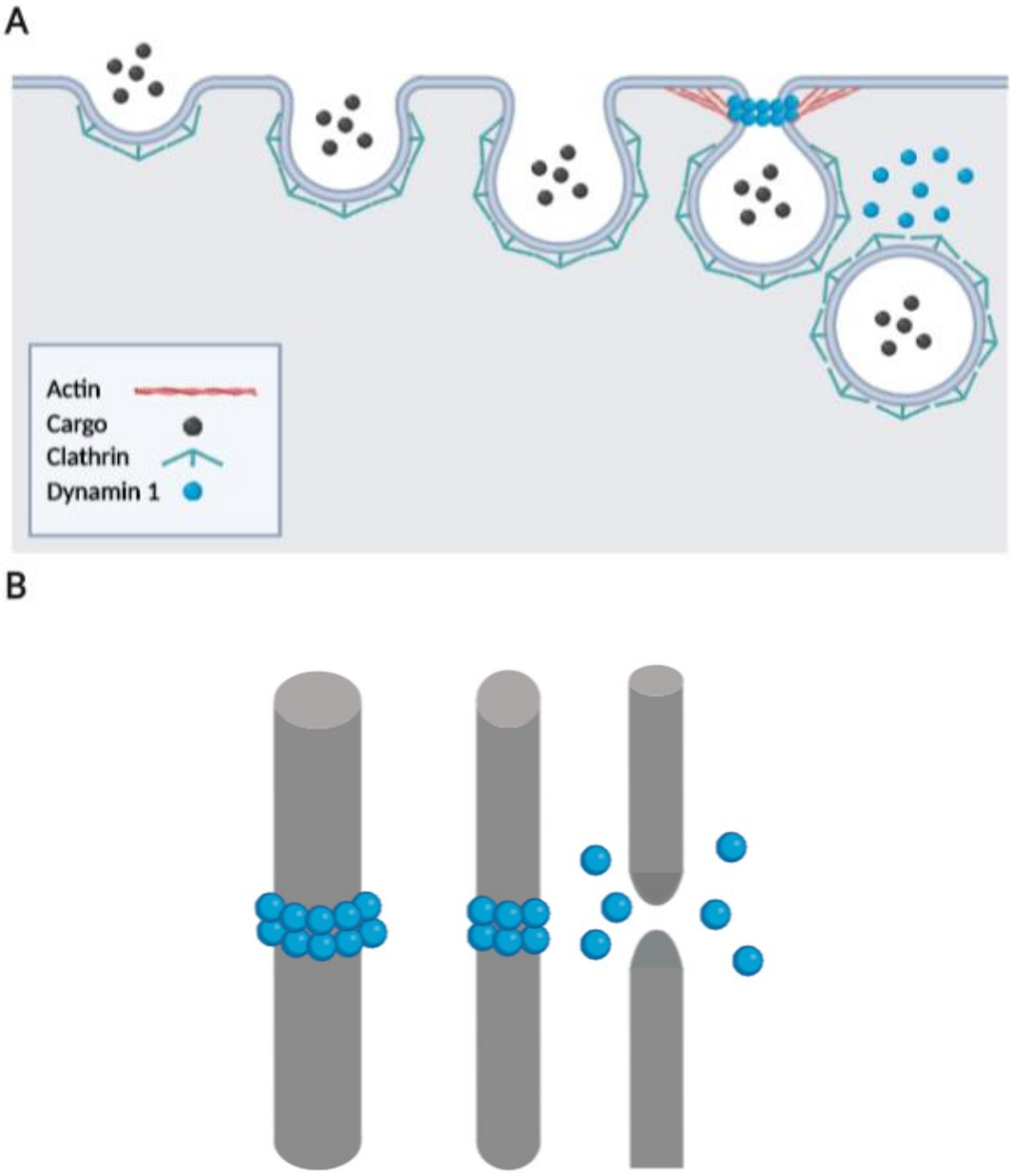

Figure 1.1 Clathrin-mediated endocytosis (CME) and Dyn1-mediated fission schemes. (A) Representation of the vesicle formation process and scission. (B) Schematic representation of a Dyn1 polymer around a membrane neck, constriction, and fission.

Originally, dynamin was described as a microtubule-binding protein that was released in presence of ATP and exhibited microtubule-dependent ATPase activity (Mettlen *et al*., 2009). However, few years later, cloning, and sequencing experiments revealed dynamin is a GTPase and not an ATPase as it had been proposed previously (Obar *et al*., 1990). Dynamins were next linked to the *Drosophila melanogaster shibire* mutation causing rapid paralysis at nonpermissive temperatures (Van Der Bliek and Meyerowrtz, 1991; Chen *et al*., 1991). This mutation was

associated with the defect in synaptic vesicle recycling and endocytosis seen as the accumulation of arrested "collared" endocytic pits at the presynaptic plasma membrane (Koenig and Ikeda, 1989). Similar formations were found at mammalian presynaptic plasma membranes upon exposure to non-hydrolysable GTP analogues (Takei *et al*., 1995). The immunostaining revealed that the protein "collars" contained dynamin (Takei *et al*., 1995). Those findings became the first indication of the dynamin involvements in the scission of the vesicle necks, as well as for the importance of GTP hydrolysis in the process.

The research that followed have touched upon almost every aspect of dynamin functionality, from its role as a hub protein in cellular signalling and transport networks to molecular details of GTP-driven conformational rearrangements of dynamin helix. The variety of the subjects is covered by several scholarly reviews (Antonny *et al*., 2016; Ferguson and De Camilli, 2012; Schmid and Frolov, 2011). One surprising unknown which persists through the years, and on which the current study is focused, is the identity of the very Dyn1 machinery, that involved in the scission and that involved in the preceding regulatory activities. While we know the Dyn1 protein in greatest details, there is no general agreement on the stoichiometry, structure, and mechanism of action of the minimal Dyn1 machinery required to perform the scission or regulatory function(s). The long-standing controversy can be routed to extremely dynamic, elusive nature of the machinery, seen in all classical dynamins studied. It was first appreciated by the lifetime fluorescence microscopy observation of Dyn2, labelled by green fluorescent protein (GFP), dynamics during CCP emergence and maturation. Total Internal Reflection Fluorescence Microscopy (TIR-FM) revealed that Dyn2 is recruited to clathrin coated pits at two differentiated phases (Merrifield *et al*., 2002). At the first phase, which corresponds to the early stages of CCP development, low levels of labelled dynamin were detected. At these early stages of endocytosis dynamin was proposed to function as a regulator of the clathrin coated pit (CCPs) maturation (Loerke *et al*., 2009; Macia *et al*., 2006; Narayanan *et al*., 2005). The exact mechanisms of this regulatory activity remain poorly understood. The second phase, corresponding to the late stages of CCP maturation, is characterized by a sharp increase in the amount of dynamin associated with CCPs (Macia *et al*., 2006; Merrifield *et al*., 2002). This dynamin burst precedes the moment of vesicle scission. Single-molecule quantification of the burst revealed that the fluorescence increase corresponded to on average 26 dynamins accumulating at the CCP prior to the scission, providing the first stoichiometric assessment of the dynamin fission machinery (Cocucci *et al*., 2014; Grassart *et al*., 2014a). Similar two-phase recruitment dynamics was later found for Dyn1 (Wang *et al*., 2020). The fluorescence microscopy observations provide no information about the spatial arrangement of the dynamin

oligomer(s) at any particular moment of time. The situation is further complicated by the involvement of multiple protein partners interacting with dynamin, the recognized hub protein in the endocytosis-associated interactome (Rosendale *et al*., 2019). Hence, the structure and the mechanism(s) of action of the Dyn1 machinery have been deduced from *in vitro* reconstitution assays and ultra-structural analyses. Classical *in vitro* approaches and the new assays used to examine dynamin will be reviewed in the next sections.

Dynamin 1 structure

Classical dynamins share a common 5-domain organization. These 5 common domains are the following (Figure 1.2.):

- ***G or GTPase domain*:** This N-terminal domain is responsible of the GTP hydrolysis (Raimondi *et al*., 2011; Schmid and Frolov, 2011).
- ***The stalk*:** consisting of a long four helix bundle, composed by the middle and the N-terminal region of the GTPase effector domain (GED) (Antonny *et al*., 2016). At this region are present most of the interfaces responsible of the protein self-assembly (Ramachandran *et al*., 2007).
- ***Bundle signaling element (BSE)*:** flexible connector between the GTPase domain and the stalk, composed by the N- and C-terminal regions of the G domain and the C-terminal region of the GED (Antonny *et al*., 2016).
- ***Pleckstrin homology domain (PH domain)*:** Domain responsible for the interaction between the protein and negatively charged lipid species, especially with phosphoinositide-4,5-bisphosphate (PIP_2) (Raimondi *et al*., 2011; Schmid and Frolov, 2011). This domain is composed by three variable loops (VLs), VL1, VL2, and VL3 (Ferguson *et al*., 1994; LEMMON and FERGUSON, 2000). From those, VL1 is partially inserted into the lipid bilayer (Ramachandran and Schmid, 2008; Ramachandran *et al*., 2009a), being important for curvature generation, and postulated as crucial for membrane destabilization (Shnyrova *et al*., 2013).
- ***Proline-rich domain (PRD)*:** responsible for the interaction with Dynamin binding partners that have SH3 domains. This unstructured domain is connected to the BSE and extends beyond the GTPase domain (Antonny *et al*., 2016).

PRD and PH domains differentiate classical dynamins from the rest of the superfamily. The PH domain has been specifically implicated in the targeting of classical dynamins to the plasma membrane (Schmid and Frolov, 2011) and, lately, in the catalysis of the membrane scission (Dar and Pucadyil, 2017; Shnyrova *et al*., 2013). Structural studies underwent with Dyn1 PH domain showed that it presents a well-defined β-sandwich core with three variable loops (VL1, 2, and

3), constituting a PIP_2-binding pocket (Lemmon and Ferguson, 2000). From those, the VL1 has been shown to insert partially into the hydrophobic core of the lipid bilayer and play an important role in the fission catalysis (Ramachandran and Schmid, 2008).

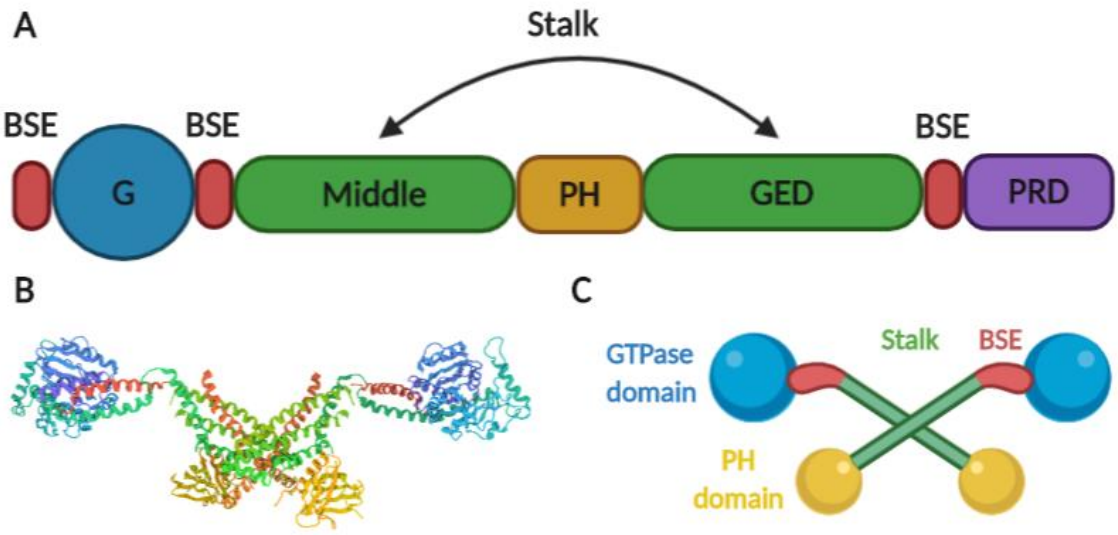

Figure 1.2 Dyn1 domain organization and structure. (A) Domain organization of a classical dynamin. (B) Crystal structure of nucleotide-free human Dyn1 (PDB 3SNH). (C) Schematic representation of the crystal structure showing the disposition of the different domains.

In 2011 the first crystal structures of the full-length dynamin were published, revealing the self-folded architecture of the protein monomer shown in Figure 1.2 (Faelber *et al*., 2011; Ford *et al*., 2011). The X-shaped dynamin dimer forms via conserved self-assembly interface at the middle of the stalk region (Figure 1.2 B, C). Further research revealed that the dynamin dimers are the elementary building blocks of larger dynamin assemblies.

Dynamin self-assembles into a helical polymer sensing and creating membrane curvature.

In the cell, Dyn1 resides predominantly in the cytosol, as an equilibrium mixture of dimers and tetramers. Large dynamin oligomers forming on the plasma membrane was first detected as electron-dense collar-like structures forming around the neck of endocytic vesicles (Takei *et al*., 1995). In the same year, negative-staining electron microscopy (EM) experiments revealed that purified dynamin self-assembled into ordered 3D structures in the bulk under low salt conditions. The dynamin rings and stacks of interconnected rings closely resembled the *in vivo* collar-like structures, suggesting for the first time the membrane-constriction activity of dynamin polymer (Hinshaw and Schmid, 1995) (Figure 1.3. A). The ability of dynamin to create

membrane curvature was firmly established when the purified protein was mixed with negatively charged large unilamellar vesicles (LUVs). Dynamin quickly transformed the vesicles into tubes covered by the protein coat, the phenomenon now known as tubulation (Sweitzer and Hinshaw, 1998; Takei *et al*., 1999). Importantly, initial association of purified dynamin with negatively charged lipid membranes was found sharply dependent on membrane curvature (Ramachandran and Schmid, 2008; Roux *et al*., 2010; Yoshida *et al*., 2004), in agreement with increased association of dynamin with CCV necks. Thin negatively charged lipid nanorods were found most effective in stimulating formation of dynamin coat (Marks *et al*., 2001; Stowell *et al*., 1999), explaining the protein association with microtubules (Shpetner and Vallee, 1989), and lipid nanorods.

Negative staining followed by high resolution cryo-EM analyses of the tubulated liposomes revealed that the dynamin self-assembles into a regular helix densely covering the membrane (Stowell et al., 1999; Zhang and Hinshaw, 2001). The helical polymer is composed by dimers, which present their G domains facing outside the helix, and the PH domains inside, interacting with the lipid membrane (Figure 1.3 A) (Chen *et al*., 2004; Mears *et al*., 2007; Zhang and Hinshaw, 2001). The helical self-assembly is mediated by two additional self-assembly interfaces at the end of the stalk region (Faelber *et al*., 2011; Ford *et al*., 2011). In the absence of nucleotide, the helical coat has an outer diameter of 50 nm, with a helical pitch between 10 and 20 nm, and creates a moderate ($0.1 nm^{-1}$) membrane curvature (Chen *et al*., 2004; Danino *et al*., 2004; Sweitzer and Hinshaw, 1998; Takei *et al*., 1998). The *in vitro* membrane tubes decorated with dynamin in the absence of GTP (Chen *et al*., 2004; Danino *et al*., 2004; Sweitzer and Hinshaw, 1998) closely resembled deeply invaginated membrane necks observed in cells treated with GTPγS (Takei *et al*., 1995). In both situations the tubes were stable as the tube lumen needs to be more constricted to trigger hemifission transformations (Bashkirov *et al*., 2008a; Mattila *et al*., 2015; Shnyrova *et al*., 2013). Additional force input required to achieve sufficiently high membrane curvatures comes from the GTP hydrolysis.

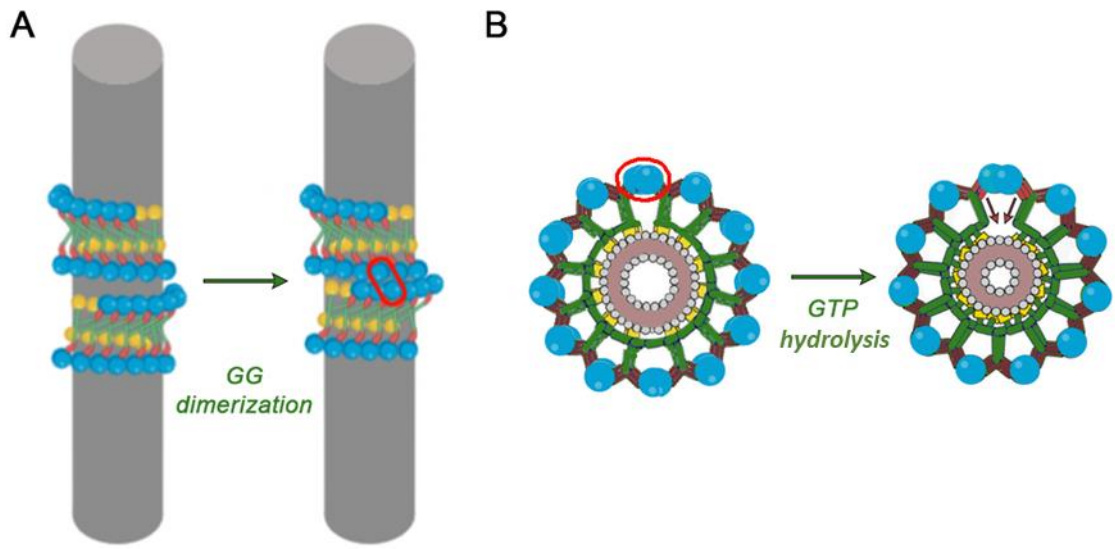

Figure 1.3 Schematic representation of the self-assembled Dyn1 polymer. (A) The helical polymer positions the G domains from adjacent rungs, allowing their dimerization. The red circle highlights the formation of a GG dimer between the adjacent rungs of the Dyn1 helix. (B) GTP hydrolysis by the dimer produces bending and kinking of the BSE and G domains of Dyn1 with respect to the stalk, resulting in production of constriction force (arrows).

Helical self-assembly stimulates GTPase activity of Dynamin via G-G dimerization

Small dynamin oligomers residing in the cytosol hydrolyse GTP relatively slow: the rate of the basal GTP hydrolysis was estimated as ~0.4-1 min^{-1} (Binns *et al*., 1999; Marks *et al*., 2001; Sever *et al*., 1999; Shpetner and Vallee, 1992; Warnock *et al*., 1996). However, the GTPase activity increases as much as 100-fold when assayed in presence of liposomes or lipid nanotubes (Leonard *et al*., 2005; Praefcke and McMahon, 2004), indicating that dynamin helices forming on the membrane substrate are mechano-active. The stimulation of the GTPase activity was linked to the GTP-driven dimerization between the G domains from the adjacent helical rungs (Chappie *et al*., 2011). The dimerization is required for the catalysis GTP hydrolysis by dynamins (Chappie *et al*., 2010). The helix prepositions the G domains for fast and efficient dimerization (Figure 1.3 A, B), explaining the increase of the hydrolysis rate upon helical self-assembly.

Besides creating the unique catalytic machinery of the hydrolysis, the GG dimerization, under specific circumstances, mediates self-assembly of dynamin into rings and helices. The GG dimer is stabilized when the hydrolysis cycle is arrested in/near the transition state using the transition state mimics, such as mixtures of AlF_4^- and BeF_3^- with GDP (Bigay *et al*., 1985, 1987). These

substances promote helical self-assembly of the full-length dynamin in the bulk, without membrane substrate (Carr and Hinshaw, 1997). Furthermore, recent cryo-EM mapping identified a putative self-assembly interface between the G domains (Kong *et al*., 2018). Though this interface is obviously too weak to drive high-order self-assembly of dynamin in cytosol, in the constant presence of GTP, it might contribute to transient oligomerization of dynamin on the membrane. This oligomerization mechanism, alternative to the stalk-driven self-assembly described above, will be important for the interpretation of the results obtained here.

The GTP hydrolysis causes constriction of the dynamin helix

While the helical self-assembly sets up the G domains of dynamin for the effective GTP hydrolysis, the energy of hydrolysis comes back to the helix driving its constriction. EM imaging of the membrane tubules coated by dynamin helices showed that the tube lumen is considerably reduced upon GTP addition (Danino *et al*., 2004; Kong *et al*., 2018; Sweitzer and Hinshaw, 1998). The luminal radius decrease from 10 nm in the apo state (Chen *et al*., 2004; Danino *et al*., 2004; Sweitzer and Hinshaw, 1998) to <2 nm at the super-constricted state (Kong *et al*., 2018; Sundborger *et al*., 2014). The dynamics of progressive membrane constriction triggered by addition of GTP to a Dyn1 helix preassembled on a lipid membrane tube was resolved by fluorescence microscopy and HS AFM assays (Colom *et al*., 2017a; Dar *et al*., 2015). The fluorescence microscopy measurements also revealed extremely high final curvatures achieved through the constriction (luminal radius <2 nm, (Dar *et al*., 2015)). Such high curvatures have long been linked to membrane instability and fission (Bashkirov *et al*., 2008b; Chernomordik and Kozlov, 2003; Kozlovsky and Kozlov, 2003). Indeed, GTP-driven membrane constriction universally caused fission, seen as a breakup on the constricted membrane tubules into progressively smaller pieces (Pucadyil and Schmid, 2008). Importantly, while the fission was seen upon addition of GTP, the non-hydrolysable analogues, such as GMPPCP or GTPγS, failed to produce fission and instead stabilized the highly constricted membrane tubes (Kong *et al*., 2018; Zhang and Hinshaw, 2001), evoking *in vivo* effect of GTPγS (Takei *et al*., 1995). The physiological relevance of the *in vitro* fission reaction was further verified by mutagenesis, with various dominant-negative mutations identified in cellular systems causing prominent inhibitory effect on the helical self-assembly and GTP-driven membrane constriction and fission by purified dynamin (Schmid and Frolov, 2011).

Initially, the constriction was linked to various rearrangements of dynamin helix (Sever *et al*., 2000). However, during the last decade crystallographic and ultra-structural analyses identified the molecular mechanism of constriction. The forces generated in the GG dimer upon the hydrolysis are translated to asymmetric bending and kinking of BSE with respect to the stalk

region leading to the constriction of the helix ((Chappie *et al*., 2011; Kong *et al*., 2018), Figure 1.3 B). Progressive constriction was shown in details by recently published cryo-EM maps of ΔPRD Dyn1 in the nucleotide bound "ground" state (mimicked by GMPPCP analogue of GTP) and in the GTP-bound state directly preceding membrane scission (Kong *et al*., 2018). Those structures revealed that, through the progression of the GTP cycle, the dynamin polymers are more conformationally restricted, and showed that BSE movement forced the stalk and the PH domain towards and inside the underlying membrane thus enforcing membrane constriction. The number of helical subunits (dimers) per turn decreases as well, from 14 in the *apo* (nucleotide-free) state (Chen *et al*., 2004) to 11 in the super-constricted state (Sundborger *et al*., 2014). The single rung of the helix thus contains 22-28 dynamin molecules, matching to the average number (26) of dynamins associated with CCP prior to fission (Cocucci *et al*., 2014; Grassart *et al*., 2014a).

This correspondence between structural and *in vivo* analyses established the shortest 1-rung dynamin helix as a minimal fission machinery (Antonny *et al*., 2016).

The constriction ratchet mechanism of fission

To explain how this machine works the constriction-ratcheting mechanism was proposed (Figure 1.4, (Antonny *et al*., 2016)). It postulates that at any particular moment only few GG dimers, randomly distributed over the helix (Galli *et al*., 2017) are engaged and active while the remaining GG pairs remain passive and disengaged. The active dimers produce the local power-strokes driving twisting/constriction motion of the helix while the passive dimers let the helix slide (Antonny *et al*., 2016; Chappie *et al*., 2011; Morlot *et al*., 2012). After completion of the GTPase cycle, the active dimers dissociate while new active GG pairs form in different places. Several rounds of GTP association, hydrolysis, and G domains dissociation lead to the constriction of the helix causing membrane fission. This dynamin mechanism of action is analogous to the mechanism of myosin-V movement on actin, but with dynamin acting as myosin-V and actin at the same time. That is why it has been proposed that both enzymes could have a common ancestor (Antonny *et al*., 2016).

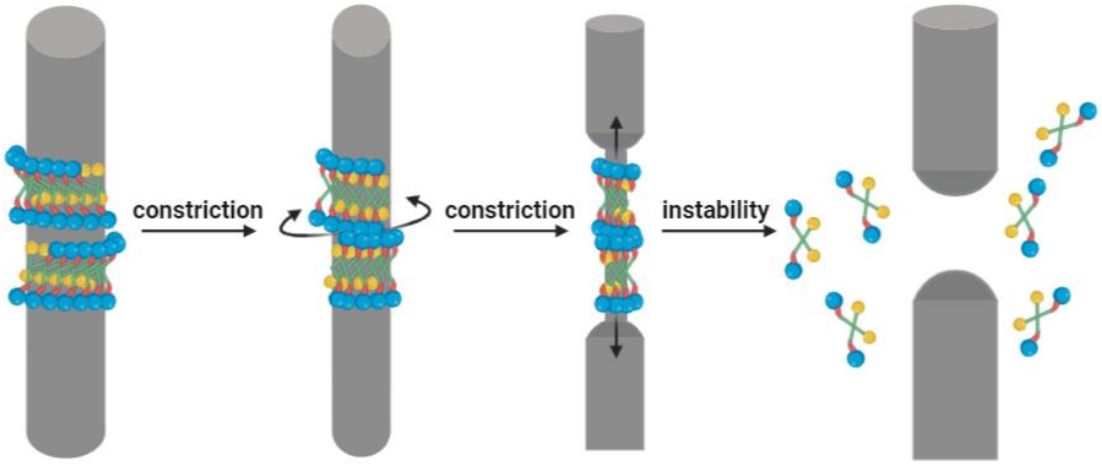

Figure 1.4 Constriction ratchet mechanism of Dyn1-driven fission. Black arrows illustrate the radial force produced by the active sliding between adjacent rungs of the Dyn1 helix, leading to the spontaneous formation of the hemifission intermediate, and fission.

Despite its overall attractive nature and solid foundation of this model, its main assumption that helical constriction shall eventually trigger fission is problematic. First, stable dynamin helices failed to produce membrane scission even at extremely high membrane curvatures (>0.5 nm^{-1}) generally associated with the scission (Schmid and Frolov, 2011). Such curvatures were detected with Dyn1 in the *apo* state operating on membrane nanotubes pre-constricted by high lateral tension (Bashkirov *et al*., 2008b) and, in the presence of GTP, with K44A mutant of Dyn1 defective in GTP hydrolysis (Sundborger *et al*., 2014). In both cases, the scission was not detected, with dynamin helices seemingly stabilizing the highly tensed lipid tubes. Second, linear radial constriction failed to produce membrane scission in computer simulations performed by different groups (Fuhrmans and Müller, 2015; Pannuzzo *et al*., 2018). The simulations, as well as experimental analyses revealed that the helical scaffold is to disassemble or somehow loosen its grip on the membrane to let it go fission (Bashkirov *et al*., 2008b; Fuhrmans and Müller, 2015; Pannuzzo *et al*., 2018; Sweitzer and Hinshaw, 1998; Warnock *et al*., 1996). The link between hydrolysis and disassembly, generic for filamentous GTPases (Gudimchuk *et al*., 2020), was recently revealed for dynamin helices (Kadosh *et al*., 2019; Kong *et al*., 2018). Third, the computer simulations indicate that to ensure robust membrane fission dynamin helical filament has to go beyond simple radial constriction and apply local torque and/or tensile force (Fuhrmans and Müller, 2015; Pannuzzo *et al*., 2018). Experiments identified the PH domain of dynamin as the mediator of that force action concomitant with radial constriction.

The GTP hydrolysis affects membrane interaction of the PH domain of dynamin

Dynamin interacts with cellular membranes via a dedicated protein domain (Ferguson and De Camilli, 2012). Classical dynamins PH domain specifically recognizes PI(4,5)P_2 lipid species present in the plasma membrane of mammalian cells (Figures 1.2, 1.3, (Schmid and Frolov, 2011)). *In vitro* analyses of the PH domain functions revealed that besides targeting dynamins to PI(4,5)P_2-enriched membranes it is also deeply implicated in the membrane scission process (Antonny *et al*., 2016). While replacing of the PH domain with an artificial membrane linker did not completely abolish its membrane scission activity, it severely slowed down the scission process (Dar and Pucadyil, 2017). This catalytic action was linked to the ability of PH domain to facilitate and accelerate local lipid rearrangements during the scission process (Dar and Pucadyil, 2017; Shnyrova *et al*., 2013).

The catalytic activity of the PH domain is based upon i) its insertion into the hydrophobic core of the lipid bilayer (Mattila *et al*., 2015; Ramachandran *et al*., 2009b), ii) its flexible orientation on the membrane surface owing to multiple membrane-binding surfaces and flexible connexion to the stalk region of dynamin (Figure 1.5). Direct involvement of the PH domain into the fission catalysis was first indicated by site-directed mutagenesis in the PH domain VL1, altering its membrane insertion capability (Ramachandran *et al*., 2009b). Since then, multiple experimental techniques have revealed that changes in the insertion and orientation of the PH domain are linked to the GTPase activity of dynamin. The insertion variation during the GTPase cycle was initially revealed by the Fluorescence Resonance Energy Transfer (FRET) between the fluorophores residing on the PH domain and in the hydrophobic membrane core (Ramachandran and Schmid, 2008). Few years later, using the short- and long-distance FRET approaches, (Mehrotra *et al*., 2014) showed that the Dyn1 PH domain presents two alternate orientations. Those different orientations depend on the stage of the GTP cycle, switching between the GTP-sensitive hydrophobic mode, characterised by the insertion of the VL1 into the lipid bilayer, and the GTP-insensitive electrostatic mode, responsible for the Dyn1 retainment on the membrane, and characterised by the VL1 retraction. The switching between the two orientation is seen as the PH domain tilting with respect to the stalk region of the protein (Figure 1.5 B).

In parallel, variable orientations of the PH domain were detected in cryo-EM maps of ΔPRD Dyn1 GMPPCP- and GTP-bound polymers (Kong *et al*., 2018) as well as in the super-constricted state, observed in the GTP-loaded Dyn1 K44A mutant (Sundborger *et al*., 2014). Furthermore, the cryo-EM imaging revealed distinct differences between the neighbouring PH domain in the dynamin dimer: one of the two domains becomes more proximal to the lipid monolayer and more distinct in electron density map, indicating restricted mobility due to tighter interaction with the

membrane (Kong *et al*., 2018). The difference in the PH domain orientation suggested that the PH domain tilting might result in the long-range twisting of the membrane binding surface of the dynamin helix, implying generation of the mechanical torque (Pannuzzo *et al*., 2018).

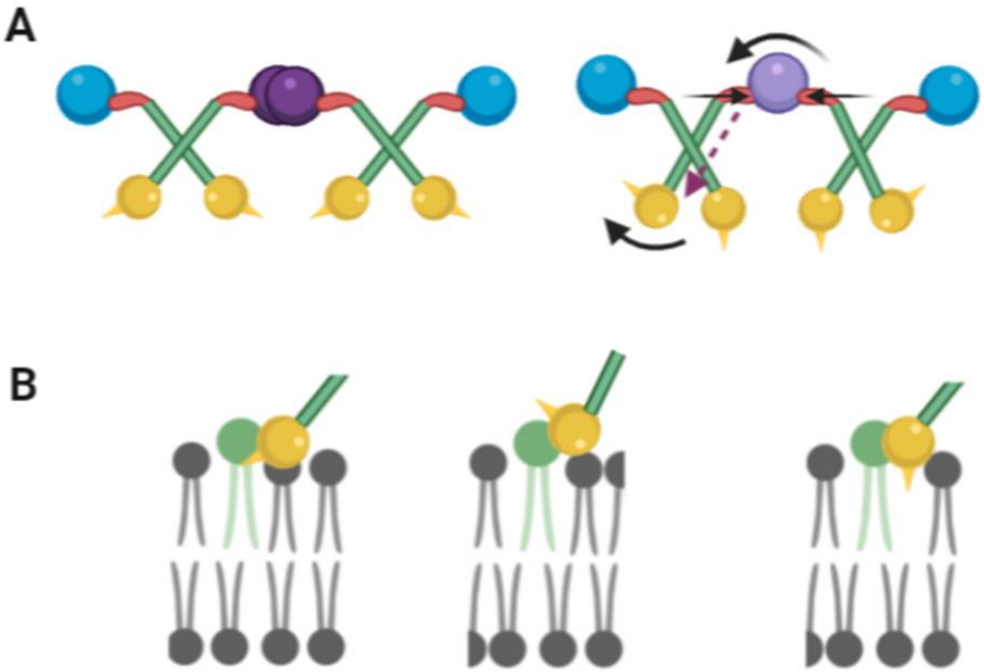

Figure 1.5 Schematic representation of the energy transduction and the alternate PH domain conformations. (A) Illustration of the conformational changes produced in the protein architecture along the GTP cycle. Dark purple represents the GTP-bound form. Light purple represents the transition state. Black arrows in the BSE illustrate the pivotal movement at these regions upon GTP hydrolysis. The dashed purple arrow shows the transduction of the energy through the stalk to the PH domain and the black arrow in the PH domain shows the orientation change at this region. The short spikes in the PH domains represents the VL1. (B) Illustration of the orientation of the PH domain at different stages of the GTP cycle. PIP_2 molecules are highlighted in green.

The dynamics of the energy transduction from the G domain to PH domain was analysed by combined photo-induced electron transfer (PET) and FRET approaches using genetically re-engineered Dyn1 (Mattila *et al*., 2015). This work showed that the BSE movement causing the constriction of Dyn1 helix indeed happens in the full length Dyn1 protein, in agreement with the structural analyses described above. Crucially, it also revealed that the helical constriction is coupled with progressive insertion of the PH domain into the membrane core. Furthermore,

arresting the Dyn1 in the transition state of GTP hydrolysis by inter-molecular cross-linking revealed that the insertion is maximal in this state (Mattila *et al*., 2015), which was also associated with maximal narrowing of the dynamin helix (Kong *et al*., 2018).

Overall, the above *in vitro* analyses of dynamin structural dynamics firmly established that the G domain and the PH domain are conformationally coupled, although structurally separated. This long-distance communication between the dynamin domains is likely bidirectional as the PH domain affects the dynamin self-assembly in solution (Kenniston and Lemmon, 2010; Schmid and Frolov, 2011). More importantly, these studies caused a paradigm shift in our understanding of the mechanical action of dynamin. The loss of cylindrical symmetry seen in the PH domain displacements during the GTPase cycle confirmed that dynamin action goes beyond simple radial constriction and led to a new class of fission mechanisms combining the constriction and torque action of the dynamin polymer.

The constriction-stretching mechanism of fission

These mechanisms could be summarized by the constriction-swinging mechanism of fission (Antonny *et al*., 2016). This model explicitly considers two modes of dynamin action (Figure 1.6): radial constriction due to narrowing of the dynamin helix and the torque and associated axial force generation due to the PH domains tilting and membrane insertion. At the initial stage of the fission process the radial constriction mode dominates, essentially replicating the early constriction-ratcheting model. Near the maximal constriction the second mode associated with the PH domain reorientation picks up and becomes dominating (Figure 1.6). The importance of the second mode is clearly illustrated by K44A mutant of Dyn1. In this mutant, the GTP hydrolysis cycle is disrupted before the transition state (Schmid and Frolov, 2011) so that it remains in the ground state characterized by the minimal PH domain insertion into the membrane core. While capable of creating extremely high membrane constriction, K44A mutant fails to produce fission (Sundborger *et al*., 2014). On the other hand, the transition state conformer of Dyn1 stabilized by inter-molecular crosslinking drives membrane transformation past the super-constriction towards hemifission (Mattila *et al*., 2015). The hemifission is driven by the cooperative insertion of the PH domain deeper into the membrane core in the transition state (Figure 1.6, (Mattila *et al*., 2015; Shnyrova *et al*., 2013)). Importantly, however, structural and functional analyses of the conformer arrested in the transition state showed that the hemifission configuration remained stable and did not spontaneously progress to complete fission (Mattila *et al*., 2015). The transition to complete fission was associated with tilting of the PH domains away from the lipid monolayer driven by the GTP hydrolysis (Mehrotra *et al*., 2014) (Figure 1.6). The torque

(Pannuzzo *et al*., 2018) and/or the stretching force (Mattila *et al*., 2015) produced by the tilting causes rupture of the hemifission intermediate thus finalizing the fission process (Figure 1.6).

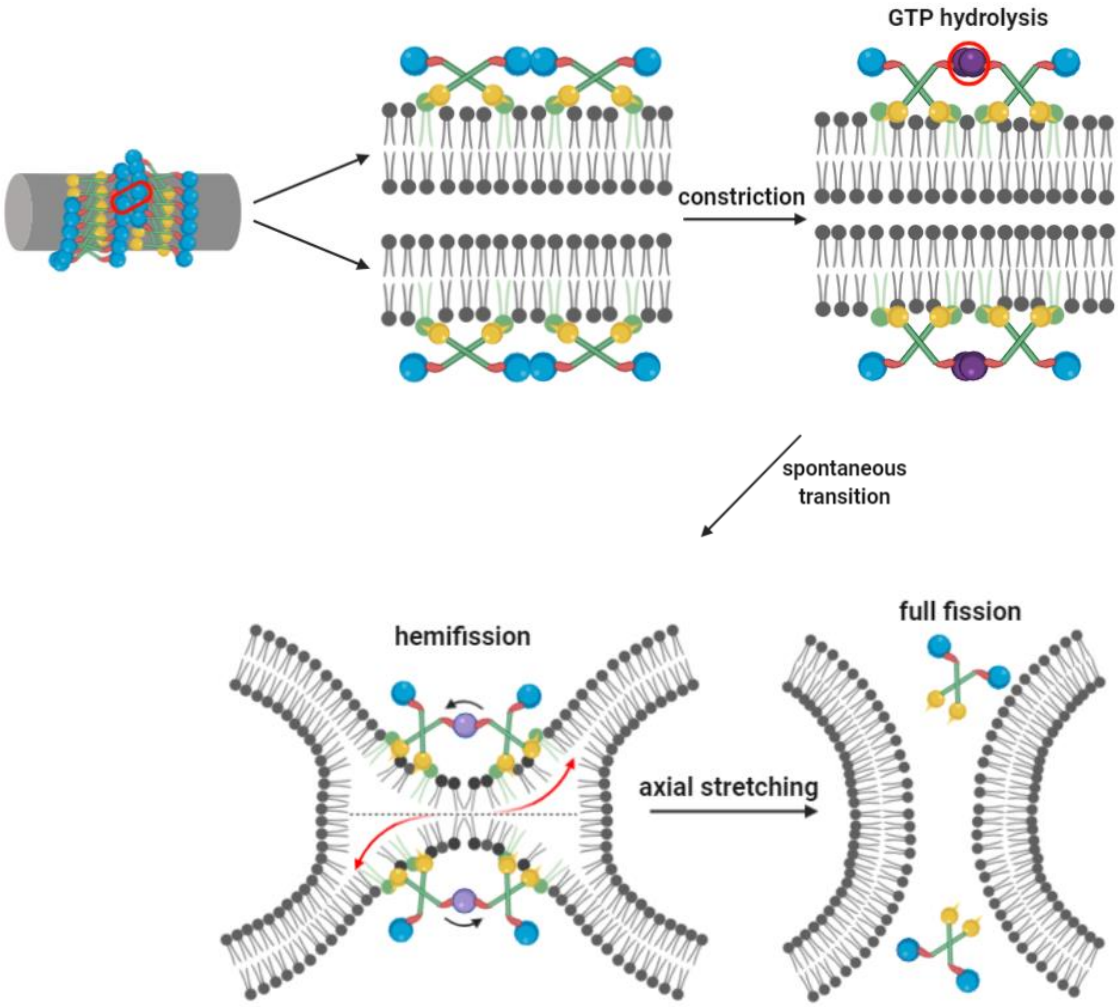

Figure 1.6 Constriction-stretching mechanism of Dyn1-driven fission. The top row illustrates the first mode of Dyn1 action when the radial constriction force dominates. Dark purple G domains represent the GTP-bound form. The bottom row illustrates the second mode of action when the axial force starts dominating. Light purple G domains represent the transition state, and the red arrows illustrate the axial force produced by the PH domains tilting upon GTP hydrolysis. PIP_2 molecules are highlighted in green. Black dashed line marks the hemifission mid-plane.

While full understanding of the PH domain dynamics requires further experimental efforts, the constriction-stretching mechanism predicts that constraining the PH domains should inhibit fission. Indeed, it was demonstrated that fission happens predominantly near the edges of long dynamin helices, where the PH domains are least constrained (Morlot *et al*., 2012). More

importantly, it has been revealed that GTP hydrolysis causes disassembly and reassembly of dynamin helix (Zhang *et al*., 2020), optimizing its size and structure for the PH domain action.

The GTP hydrolysis drives assembly-disassembly cycle of the Dyn1 helix

Under physiological conditions dynamin fission machinery is to rapidly recycle upon completion of the fission reaction. The rapid recycling is especially important for Dyn1 machinery responsible for the rapid turnover of synaptic membrane (Ferguson and De Camilli, 2012). Accordingly, several *in vitro* studies reported that Dyn1 helices rapidly disassemble upon nucleotide hydrolysis (Bashkirov et al., 2008a; Pucadyil and Schmid, 2008; Warnock et al., 1996). Recent advances in the *in vitro* techniques enabled looking at the disassembly process with high spatio-temporal resolution. Membrane deformations produced by elementary subunits of dynamin helices, the dynamin dimers, were resolved using the approach analogous to the molecular detection in solid state and protein nanopores (Bashkirov *et al*., 2020). The technique revealed that under constant GTP turnover Dyn1 produces periodic changes in membrane curvature associated with rapid assembly and disassembly of short Dyn1 helices (Shnyrova *et al*., 2013).

Molecular details of the assembly-disassembly process were later revealed by high speed atomic force microscopy (HS-AFM) (Colom *et al*., 2017b; Takeda *et al*., 2018). HS AFM imaging showed that pre-assembled dynamin polymer experiences changes in its helical structure upon GTP hydrolysis, due to transient association and dissociation events observed between adjacent G domains, which was translated into helix constriction (Colom *et al*., 2017b; Takeda *et al*., 2018). The distance between the helical turns varied over time, likely reflecting cycles of GTP binding, hydrolysis, and dissociation. Crucially, later analysis (Kadosh *et al*., 2019) revealed that the cyclic association-dissociation of the G domains led to the helix breakage into sub-helical pieces of seemingly arbitrary size. Such irregular disassembly reflects the random distribution of the hydrolysis events over the helix (Galli *et al*., 2017). While such a drastic fractionation of the helix shall greatly increase the PH domain freedom to tilt, it simultaneously mechanically uncouples the helical parts, questioning why the helix was assembled in the first place. The solution to this paradox was found in the latest high resolution cryo-EM analysis of Dyn1-driven membrane constriction.

The 2-start helix or how Dynamin1 really works

Early cryo-EM assessment of the narrow helices formed by the K44A Dyn1 mutant in the presence of GTP revealed that the 2-start helical structure in strike distinction from 1-start helical structure generally associated with dynamins ((Sundborger *et al*., 2014), Figure 1.7).

Similar 2-start helical arrangement was observed in a metastable super-constricted Dyn1 helices formed in the presence of GTP, prior to membrane fission (Kong *et al*., 2018). The authors associated the 2-start arrangement with the maximal packing density of the protein on the membrane surface, explaining the extreme constriction. Furthermore, the 2-start arrangement revealed distinct changes of the PH-domain orientation caused by GTP hydrolysis. The authors further revealed that the transition from 1-start helical arrangement, seen in apo Dyn1, to the 2-start arrangement requires disassembly of the 1-start helix, explaining the experimental observations described in the above section.

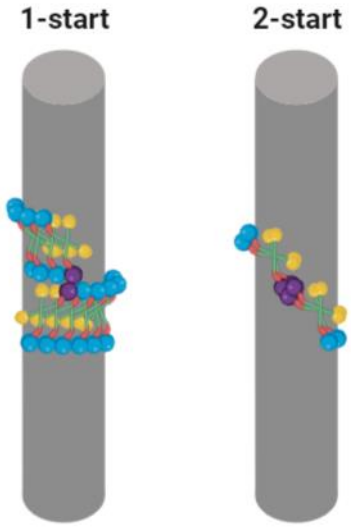

Figure 1.7 Comparison of the alternative self-assembly paths observed in Dyn1. The 1-start helical symmetry represents the classical self-assembly pathway through the stalk. To enable G-G dimerization, at least, a full helical rung must form. The 2-start helical symmetry combines both self-assembly paths observed in dynamin. The classical stalk assembly, leading to the formation of the tetramers, and the alternative dimerization through the G domains. The combination of both pathways would allow the formation of non-cylindrical mechano-active units. Dark purple G domains represent the GTP-bound state, which enables G-G dimerization.

One crucial difference between the 1-start and 2-start arrangements is the mechanism of G-G dimerization. While the 1-start helix needs to complete the full turn to enable the dimerization, in the 2-start helix G-G dimers emerge from the beginning of the self-assembly process (Figure 1.7). Furthermore, cryo-EM mapping identified a distinct self-assembly interface between the G domains in the 2-start helix (Kong *et al*., 2018). This G2 interface might assist in the self-assembly process, thus coupling the G-G dimerization and helical self-assembly (Chappie *et al*., 2010; Kong

et al., 2018). Importantly, in the cytoplasm dynamins operate under constant GTP turnover, with excessive amount of GTP generally available (Traut, 1994). Under such conditions, dynamins shall, in principle, self-assembly directly into the 2-start helical register.

The ab initio formation of the 2-start helix has one clear advantage: the helix immediately becomes GTP-active (Figure 1.7). In fact, biochemical analysis of helices co-assembled by wild-type and mutant dynamins showed that both GTPase and fission functional units can be smaller than a full turn of a 1-start helix (Liu *et al*., 2013). The GTPase activity of short subhelical dynamin oligomers can explain the fission events driven by small dynamin complexes containing less than 26 dynamin monomers required to form the full turn of the 1-start helix (Cocucci *et al*., 2014; Grassart *et al*., 2014b). The GTPase activity of subhelical dynamin might be also relevant to the regulatory role of dynamin at early stages of endocytosis, where non-helical assemblies act as a CCP maturation checkpoint (Loerke *et al*., 2009; Macia *et al*., 2006; Narayanan *et al*., 2005). All the above made us critically rethink the *in vitro* approach to reconstitution and mechanistic analyses of dynamins, and Dyn1 in particular.

Hypotheses and objectives of this work

For more than 25 years, from the seminal observation of dynamin self-assembly into ring-like and helical structures in solution (Carr and Hinshaw, 1997; Hinshaw and Schmid, 1995), the *in vitro* reconstitution approaches are fixed on the dynamin helices. But, as we described above, there are multiple indications in the literature that the functional unit is smaller than a single helical rung. Everything from functional to biochemical assays point us into this direction. And apart from the *in vitro* world, the GTPase activity of small dynamin oligomers would have clear physiological significance for the regulatory functions of Dyn1 and 2 (Loerke *et al*., 2009; Macia *et al*., 2006; Narayanan *et al*., 2005; Wang *et al*., 2020). Then, why have helices been so popular? The physiological significance of the helix resides in the evolutionary conserved nature of the self-assembly interfaces, shared by multiple members of the dynamin superfamily (Faelber *et al*., 2013). Still, we note that long, microscopic dynamin helices might have yet another function, namely regulation of the self-assembly of microtubule and actin filaments (Zhang *et al*., 2020). To perform fission, mind the regulation of CCP evolution, the helices are to miniaturize. But even subhelical oligomers retain all of the attributes and symmetries of the full helix, so that mechanisms of helical self-assembly revealed with long helices should remain relevant there. Another might be the extreme efficiency and robustness of the stalk-driven helical self-assembly of dynamins, and Dyn1 in particular, in the absence of GTP. Still, we note that the self-assembly is a nucleation process and, as Dyn1 in the bulk is in dimer-tetramer equilibrium, the nucleus of the nascent helix is likely small. Besides, in the constant presence of GTP the competitive assembly-disassembly mechanism involving the G2 interface is present so that the resulting size of the dynamin machinery is kinetically regulated.

The main goal of this work is to understand the mechanisms behind dynamic self-assembly of Dyn1 and emergence of its mechano-chemical activity. Based on the above arguments, we **hypothesize that**:

- GTP regulates self-assembly of Dyn1 via controlling dimerization of the GTPase domains of the protein.
- Subhelical Dyn1 oligomers are mechano-chemically active.
- Subhelical Dyn1 oligomers are self-sufficient membrane fission machines.
- The size and function of the Dyn1 machine depend on the membrane substrate.

To test these hypotheses, we plan to impair and disrupt helical self-assembly of Dyn1 using nanoengineered membrane templates, dynamin mutations and kinetic traps and further assess

molecular stoichiometry, architecture and mechano-chemical activity of the small dynamin oligomers using single molecule approaches.

The **objectives** of the present work are:

- To create and characterize a nanoengineered SLB template to study the mechano-chemistry of non-helical Dyn1 assemblies.
- To identify the minimal Dyn1 mechano-chemical unit on the nanoengineered membrane substrates.
- To study the mechano-chemical action of non-helical Dyn1 units on lipid membrane nanotubes and determine whether they are self-sufficient to break membranes apart.

Chapter 2:

Materials and methods

Equipment and materials

Giant Suspended Bilayers (GSBs) and Giant Unilamellar Vesicles (GUVs) formation

Microcentrifuge tubes	Safe-lock tubes, 1.5 mL, Eppendorf, Germany.
Vortex	$2x^3$, Velp Scientifica, Italy.
Teflon® film	Teflon® film 0.02'' thick, 24'' wide, VS002X24, Fluoro-plastics Inc., USA.
Silicon Oxide Microspheres	Ø=40 µm, C-SI-O-40, #140256 Corpuscular, USA.
Peristaltic Pump	2C 7.0mbar, Vacuumbrand, Germany.
Parafilm	4'' Parafilm® M Barrier Film, SPI supplies, USA.
35mm petri dishes	S01775, Thermo Fisher Scientific, USA.
Borosilicate glass capillaries	GB 150-10, Science Products, Germany.
Thermostatic Bath	CBN 18-30, Heto-Holten, Germany.
Cover glass	No.1, 25mm diameter glass covers, #41001125, Waldemar Knittel Glasbearbeitungs, Germany.
Coverslip chamber 25mm	QR-40LP, Warner Instruments, USA.

Argon compressed gas	Alphagaz™, Air Liquide, France.

Large Unilallemar Vesicles (LUVs) formation

Vortex	2x^3, Velp Scientifica, Italy.
Peristaltic Pump	2C 7.0mbar, Vacuumbrand, Germany.
Liposome Extruder	Lipex Extruder, Transferra, Canada.
Polycarbonate membranes	Whatman® Nucleopore Track-Etched Membranes, 25mm diameter, pore size 0.1 µm, #110605, Merck-Millipore, Germany.
Polycarbonate membranes	Whatman® Nucleopore Track-Etched Membranes, 25mm diameter, pore size 0.4 µm, #110607, Merck-Millipore, Germany.
Microcentrifuge tubes	Safe-Lock Tubes, 1.5mL, Eppendorf, Germany.
Parafilm	4'' Parafilm ® M Barrier Film, SPI supplies, USA.
Argon compressed gas	Alphagaz™, Air Liquide, France.
Liquid nitrogen	Air Liquide, France.
Thermostatic Bath	CBN 18-30, Heto-Holten, Germany.

Lipid Nanotubes (NTs)

Microcentrifuge tubes	Safe-lock tubes, 1.5 mL, Eppendorf, Germany.
Vortex	$2x^3$, Velp Scientifica, Italy.
Teflon® film	Teflon® film 0.02'' thick, 24'' wide, VS002X24, Fluoro-plastics Inc., USA.
Silicon Oxide Microspheres	Ø=40 µm, C-SI-O-40, #140256 Corpuscular, USA.
Peristaltic Pump	2C 7.0mbar, Vacuumbrand, Germany.
Parafilm	4'' Parafilm® M Barrier Film, SPI supplies, USA.
35mm petri dishes	S01775, Thermo Fisher Scientific, USA.
Borosilicate glass capillaries	GB 150-10, Science Products, Germany.
Cover glass	No.1, 25mm diameter glass covers, #41001125, Waldemar Knittel Glasbearbeitungs, Germany.
Coverslip chamber 25mm	Quick Change Chamber for 25mm, QR-40LP, #64-0367, Warner Instruments, USA.
Argon compressed gas	Alphagaz™, Air Liquide, France.
Sticky tape	SecureSeal™ Adhesive Sheet SA-S-1L, Grace Bio-Labs, USA.
Silicone Isolators	Silicone isolators Un-cut Sheet, #70338-20, Electron Microscopy Sciences, USA.
Plasma cleaner	Plasma cleaner PDC-002-CE, Harrick Plasma, USA.
Oil-Based Vacuum Pump	Dekker´s vacuum pump Titan series, Dekker Vacuum Technologies Inc., USA.

Polydimethylsiloxane (PDMS) elastomer	Dow Corp., Sylgard™ 184 Silicone Elastomer Kit.
Gastight Hamilton syringe	Gastight 1700 series, Hamilton comp., USA.
Syringe pump	LEGATO®130 Syringe pump, #78-8130, KD Scientific, USA.
Tubing	#24 AWG Thin Wall Tubing Natural, Cole Palmer, Cole-Palmer Instrument Company, USA.
Microfluidic fitting	Microfluidic fitting 23G Steel tubing PDMS adapter, Darwin Microfluidics, France.

Lipids

1,2-dioleoyl-sn-glycero-3-phosphocholine, 18:1 (Δ9-cis) PC, DOPC

#850375, Avanti Polar Lipids Inc., USA.

1,2-dioleoyl-sn-glycero-3-phospho-L-serine (sodium salt), 18:1 PS, DOPS

#840035, Avanti Polar Lipids Inc., USA.

Cholesterol (ovine wool, >98%), Chol

#700000, Avanti Polar Lipids Inc., USA.

L-α-phosphatidylinositol-4,5-bisphosphate (Brain, Porcine) (ammonium salt), $PI(4,5)P_2$

#840046, Avanti Polar Lipids Inc., USA.

1-oleoyl-2-[12-biotinyl(aminododecanoyl)]-sn-glycero-3-phosphocoline, 18:1-12:0 Biotin PC

#860563, Avanti Polar Lipids Inc., USA.

Texas Red™ 1,2-Dihexadecanoyl-sn-Glycero-3-Phosphoethanolamine, Triethylammonium Salt (Texas Red™ DHPE)

#T1395MP, Life Technologies™, USA.

Protein purification

Sf9 insect cells	Cell Line from *Spodoptera frugiperda* pupal ovarian tissue, #89070101, Sigma, Sigma-Aldrich, USA.
Protease Inhibitor Cocktail	cOmplete Tablets EASYpack, #04693116001, Roche, Germany.
Ti70 Rotor	Beckman Coulter, Beckman Coulter, Inc, USA.
Centrifuge	Ultra Optima L90K Beckman Coulter, Beckman Coulter, Inc, USA.
Centrifuge	Heraeus™ Biofuge™ Stratos, #75005283, ThermoFisher Scientific Inc, USA.
Sonicator	Soniprep 150, MSE, UK.
GST Microspheres	Pierce™ Glutathione Magnetic Agarose Microspheres, #78601, TermoFisher Scientific Inc., USA.
Heating magnetic stirrer	ARE, Velp Scientifica, Italy.
Gravity Chromatography Column	Econo-Pac® Chromatography Column, Bio-Rad, Bio-Rad Laboratories, Inc, USA.
BCA Protein Assay Kit	Pierce™ BCA Protein Assay Kit, #23227, ThermoFisher Scientific Inc., USA.

Buffers and buffer components

Potassium Chloride, KCl

#P9333, SigmaUltra, Sigma-Aldrich, USA.

HEPES Buffer

1M solution pH 7.3, #BP299, Fisher Bio reagents, ThermoFisher Scientific, USA.

Ethylenediaminetetracetic acid solution, EDTA

0.5M, pH 8.0 #03690, Fluka, Sigma-Aldrich, USA.

Magnesium Chloride solution, $MgCl_2$

1M, #63069, Fluka, Sigma-Aldrich, USA.

Ethylene glycol-bis(2-aminoethylether)-*N,N,N',N'*-tetraacetic acid, EGTA

#E3889, Sigma, Sigma-Aldrich, USA.

DTT

#GE17-1318-01, Sigma, Sigma-Aldrich, USA.

D-(+)-Trehalose dihydrate

#T9449, Sigma, Sigma-Aldrich, USA.

Sodium Fluoride, NaF

#201154-5G, Sigma, Sigma-Aldrich, USA.

Aluminium Chloride, $AlCl_3$

#563919-5G, Sigma, Sigma-Aldrich, USA.

Phosphate-buffered saline, PBS

Phosphate-buffered saline 10X, #BP399-1, Fisher BioReagents™, USA.

Organic solvents

Chloroform for HPLC	#366927, Sigma-Aldrich, USA.
Methanol (≥99,8%)	NORMAPUR, #20847, VWR, USA.
Ethanol (≥99,5%)	EMSURE, #100983, Merk Millipore, USA.

Fluorescent labels

Qdot® 705	Qdot™ 705 Streptavidin Conjugate, #Q10163MP, ThermoFisher Scientific, USA.

Nucleotides

Guanosine 5'-triphosphate sodium salt, Na GTP

#G5884, Sigma, Sigma-Aldrich, USA.

Guanosine 5'-triphosphate lithium salt, Li GTP

#G5884, Sigma, Sigma-Aldrich, USA.

Guanosine 5'-diphosphate sodium salt, Na GDP

#G7127, Sigma, Sigma-Aldrich, USA.

β,γ-Methyleneguanosine 5'-triphosphate sodium salt, GMPPCP

#M3509, Sigma, Sigma-Aldrich, USA.

Molecular biology

In-Fusion HD EcoDry Cloning Plus	In-Fusion® HD EcoDry™ Cloning Plus, #638915, Takara, Takara Bio Inc., Japan.
Site-directed mutagenesis kit	KOD-Plus-Mutagenesis Kit, #SMK-101, TOYOBO, TOYOBO Co., Ltd., Japan.
Chemically competent cells	Stellar™ Competent Cells, #636766, Takara, Takara Bio Inc., Japan.
Miniprep Kit	GeneJET Plasmid Miniprep Kit, #K0502, ThermoFisher Scientific, USA.
Thermocycler	Mastercycler personal, Eppendorf AG, #5332 01577, Germany.

LB	Lennox L Broth Base, #12780052, Invitrogen™, USA.
LB Agar	#1083.00, Pronadisa Micro & Molecular Biology, Spain.
35mm petri dishes	S01775, Thermo Fisher Scientific, USA.
Centrifuge	Allegra™ X-12R Centrifuge, Beckman Coulter, USA.
Centrifuge	Biocen 22 R, Ortoalresa, Spain.
DNA Electrophoresis	E-Gel Power Snap Electrophoresis Device, #G8100, ThermoFisher Scientific, USA.
Agarose gel	E-Gel EX agarose gels, 1%, #G401001, ThermoFisher Scientific, USA.
DNA Ladder and Sample Loading Buffer	E-Gel 1 Kb Plus Express DNA Ladder with E-Gel Sample Loading Buffer (1X), #10488091, ThermoFisher Scientific, USA.

Cell culture

Cos-7 cells	ATCC® CRL-1651™, ATCC®, USA.
Transfection reagent	GeneJuice® Transfection Reagent, #70967, Sigma-Aldrich, USA.
Cell Culture Imaging Dish	Glass bottom Dish 35mm, #81218-200, Ibidi®GmbH, Germany.
Medium	DMEM (1X), high glucose, GlutaMAX™ Supplement, #10566016, Gibco® by life technologies, USA.
Flask	TC Flask T25, Stand. Vent. Cap, #83.3910.002, Sarstedt, Germany.

Trypan Blue Solution	Trypan Blue Stain (0,4%), #15250-061, Gibco® by life technologies, USA.
Automated Cell Counter	TC20™ Automated Cell Counter, BioRad, USA.
Counting Slides	Dual Chamber for cell counter, #145-0011, BioRad, USA.
Trypsin	Trypsin-EDTA 0,05% (1X), #25300-062, Gibco® by life technologies, USA.

Other materials

Green Fluorescent Protein, GFP	GREEN FLUORESCENT PROTEIN (GFP) 300UG, #14-392, Merck Life Science S.L.U, Spain.
Spin Desalting Columns	Zeba™ Spin Desalting Columns, 7K MWCO, 0,5mL, #89882, ThermoFisher Scientific, USA.
SDS-PAGE Electrophoresis Gel	Novex™ 4-20% Tris-Glycine Mini Gels, WedgeWell™ format, 12-well, #XP04202BOX, ThermoFisher Scientific, USA.

Peptoid Nanotubes (PNTs) were kindly provided by the group of Dr. Aleksandr Noy from the Lawrence Livermore National Laboratory (LLNL) in Livermore, CA, USA.

Epifluorescence microscopy

Eclipse Ti-e inverted microscope, Nikon, Japan

Lense	CFI S Plan Fluor ELWD 40X (NA=0.60), Nikon, Japan.

Lense	CFI Apo TIRF 100X Oil (NA=1.49), Nikon, Japan.
Zyla Camera	Zyla 4.2 sCMOS, Andor, Oxford Instruments, UK.
Fluorescence Lamp	pE-4000, Cooled, UK.
PC workstation	Dell Inc., USA.
Optical table	Newport, USA.
Fluorescence filter	560/585, FF560/25 TRITC, Semrock, USA.
Fluorescence filter	485/505, FF01-485/20 FITC, Semrock, USA.
Fluorescence filter	432/515/595/730, FF01-432/515/595/730-25, Semrock, USA.

Confocal microscopy

TCS SP5 II Confocal microscope, Leica Microsystems GmbH, Germany

Photomultiplier Detectors, PMT	Air-cooled R9624 Hamamatsu Photonics, Japan.
Lense	HCX PL APO 63x/1.20 W CORR lbd.blue (NA=1.2), Leica Microsystems GmbH, Germany.
Lense	HCX PL FLUOTAR 100x/1.30 Oil (NA=1.4), Leica Microsystems GmbH, Germany.
PC workstation	Dell Inc., USA.
Optical table	Newport, USA.

TCS SP8 Confocal microscope, Leica Microsystems GmbH, Germany

Lense	63x Oil (NA=1.4), Leica Microsystems GmbH, Germany.
Lense	HC PL APO 100x/1.40 Oil (NA=1.4), Leica Microsystems GmbH, Germany.
PC workstation	Dell Inc., USA.
Optical table	Newport, USA.
STED CW Unit	Leica TCS STED CW (592 depletion laser for super-resolution), Leica Microsystems GmbH, Germany.
High-sensitive Hybrid Detectors	Hybrid Detector Leica HyD, Leica Microsystems GmbH, Germany.

Cryo-Electron Microscopy

Field Emission Scanning Electron Microscope (FESEM), JEM-2200FS/CR, JEOL Inc., Tokyo, Japan

CCD Camera	16 megapixels, (4096 x 4096 pixels), 895 model, US4000, GATAN, USA.
Software	JEM-toolbox, TEMography.com, Japan.
Automatic vitrification robot	Vitrobot, FEI, The Netherlands.
High vacuum coating system for carbon evaporation and glow discharge	MED 020, BALTEC, Switzerland.
Holey Carbon Films	R2/2, Quantifoil®, Quantifoil Instruments GmbH, Germany.

Atomic Force Microscopy

AFM	NanoWizard II AFM, JPK Instruments, Germany.
Table	Halcyonics Micro 40 antivibration table, Halcyonics, Inc., USA.
Acoustic enclosure	JPK, Germany.
Cantilevers	V-shaped MLCT Si_3N_4 cantilevers, nominal spring constants 0.01-0.1 N/m, Bruker, USA.
Microscope	Leica DMI 4000B microscope, Leica Microsystems GmbH, Germany.

Other equipment

Bath sonicator	FB15049, Fisher Scientific, Thermo Fisher Scientific, USA.
pH paper strips	Macherey-Nagel, Germany.
Balance	CP32025, Sartorius, Germany.
Balance	CP225D, Sartorius, Germany.
Balance	ME36S-0CE, Sartorius, Germany.
Ultrapure water purification system	Ultrapure Direct-Q® 3 UV, Merck-Millipore, Germany.
Variable Volume Single Channel Pipettes	0.1-2, 2-20, 20-200, 100-1000, Discovery Comfort, HTL, Germany.
Plate reader	Synergy HT, BioTek Instruments Inc., USA.

Data acquisition software

Micro-Manager	1.4, version 1, Micro-Manager, NIH, USA.
LAS AF	2.6.3 Leica Microsystems GmbH, Germany.

JPK Nanowizard Control	JPK Instruments AG, Germany.

Data analysis software

Image J	64, 1.50n, NIH, USA.
Origin 8	SR4, OriginLab Inc., USA.
Imaris 7.4	Oxford Instruments, UK.
Icy 2.0	France.
JPK Data Processing	version spm-5.0.131, JPK Instruments AG, Germany.

Methods

Model membranes

Multilamellar vesicles formation

Multilamellar vesicles (MLVs) were used as starting point for all model membranes produced in this thesis. Lipid composition and total lipid concentration of MLVs used in this work are described in table 2.1.

MLVs were prepared as follows:

1. Appropriate amounts of lipid stocks in chloroform, or chloroform:methanol:water, were mixed in a 1.5mL Safe-Lock Eppendorf® tube.
2. The desired lipid mixture was dried under vacuum for, at least, 15 minutes till the formation of a lipid film over the microcentrifuge tube wall.
3. When a lipid in chloroform:methanol:water was added to the composition, the lipid film was resuspended in a mixture of chloroform:methanol (9:1) and dried again under vacuum.
4. MLVs were, finally, produced by hydration of the lipid film with HEPES 1mM and vortexing.

Table 2.1. Lipid compositions and their concentrations for all MLVs used in this thesis.

SLBs Imaging	DOPC:DOPS:Chol:PI(4,5)P_2:TR-DHPE (68.95:20:10:1:0.05 mol%)	0.5 g/L
NTs Imaging	DOPC:DOPS:Chol:PI(4,5)P_2:TR-DHPE (69.45:20:10:0.5:0.05 mol%)	0.5 g/L
SLB fluidity determination	DOPC:DOPS:Chol:BiotinPC:TR-DHPE (69.75:20:10:0.2:0.05 mol%)	0.5 g/L
Dyn1 biochemical activity	DOPC:DOPE:DOPS:Chol:PI(4,5)P_2 (24:45:20:10:1 mol%)	0.5 g/L

Giant suspended bilayers (GSBs) formation

Functional analyses of Dyn1, such as membrane tubulation and fission assays (Higgins and McMahon, 2005) require soft, easily deformable membrane templates having sufficient membrane reservoir to support formation of microns-long Dyn1 scaffolds. Originally, Large Unilamellar Vesicles (100-400nm LUVs) have been generally used for such purposes. However, dynamics of the LUVs transformations is impossible to visualize and quantify in real time. (Pucadyil and Schmid, 2008) developed a novel lipid template, called SUPER (from *sup*ported bilayers with *e*xcess membrane *r*eservoir), to assay tubulation and membrane fission. Recently, a new lipid template, based on SUPER templates and some of the recent developments in GUVs production, has been developed, which incorporates some novel features compared to the previous one (Velasco-Olmo *et al*., 2019a).

The steps required for the Giant Suspended Bilayers (GSBs) formation (Velasco-Olmo *et al*., 2019b) were the following:

1. The first step corresponds to the MLVs formation.
2. 10µL of the MLVs suspension were deposited in a Petri dish covered with a Teflon® film, forming 4 equal drops. A prewashed 40µm silica beads solution was added to the drops. The beads precipitated on the drops when a 10µL micropipette tip filled with 1µL of the suspension contacted them.
3. The Petri dish containing the bead-MLV mixture was placed under vacuum for 15 minutes till complete evaporation of the MLVs suspension, forming a multilamellar lipid film over the beads.

4. Using a fire-closed glass capillary, the beads covered with the lipid film were deposited into a cut 10µL micropipette tip (2/3 of its original size) prefilled with 6µL of Trehalose 1M.
5. The cut tip was placed into a humidity chamber and incubated at 60° for 15 minutes for the lamellas prehydration.
6. A microscopy observation chamber was prepared during the prehydration step. A coverslip, previously cleaned by sonication with pure ethanol for 30 minutes, was rinsed several times with Milli-Q water, followed by 30 sec plasma cleaning. The cover glass was blocked using a 0.2g/L BSA solution for 15 minutes and rinsed with water after the incubation. The microscopy chamber was then filled with the working buffer (KCl: HEPES: EDTA (150:20:1 mM)) and mounted on the stage of the epifluorescence inverted microscope.
7. The prehydrated lipid covered beads were transferred to the microscopy chamber by touching the surface of the buffer with the cut tip. The beads were incubated in the working buffer for 10-20 extra minutes for the complete formation of the GSBs.

Giant Unilamellar Vesicles (GUVs) formation

The Giant Unilamellar Vesicles were formed modifying a bit the GSBs protocol (Velasco-Olmo *et al*., 2019b).

1. Steps 1-5 from the GSBs formation section were followed.
2. A 0.5mL microcentrifuge tube was filled with 30µL of working buffer (KCl: HEPES: EDTA (150:20:1 mM)) and the lipid covered beads were deposited into the tube.
3. After 15 minutes of incubation, using a cut tip, the GUVs were released from the beads by gentle pipetting up and down several times. The GUVs present in the supernatant were transferred to a new 0.5mL microcentrifuge tube.
4. A microscopy observation chamber was prepared as in step 6 in the GSBs formation section. The GUVs were added to the chamber for its observation.

Large Unilamellar Vesicles (LUVs) formation

Large Unilamellar Vesicles (LUVs) were formed following the next steps:

1. The first step corresponds to the MLVs formation, substituting HEPES 1mM for the desired hydrating buffer.
2. MLVs were subjected to 10 freeze and thaw cycles. Each cycle was composed of two steps, 1 minute of immersion in liquid nitrogen and transference to a 35° water bath until the complete thaw of the sample. This process allows the formation of unilamellar vesicles of different sizes.

3. The vesicles were extruded by passing 10 times the sample through polycarbonate filters of the desired pore size (100 or 400 nm).

Supported Lipid Bilayers (SLBs) formation from lipid covered beads

SLBs formation from silica beads was previously described in (Pucadyil and Schmid, 2010). Steps required for their preparation were the following:

1. Steps 1-3 from the GSBs protocol were followed.
2. Using a fire-closed glass capillary the lipid covered beads were deposited in the observation chamber, filled with working buffer. The coverslip was previously cleaned as described in step 6 of the 2.1.2. section, BSA treatment of the cover glass surface was avoided. Once the beads contacted the coverslip surface, the SLBs were formed by "lipid spilling" from silica beads. After 10 minutes of incubation, beads were removed from SLBs top.

Peptoid Nanotubes (PNTs)

Nanofabricated templates with precisely defined local curvature were instrumental in characterizing curvature-driven binding and self-assembly of peripheral membrane proteins. Micro- and nano-patterned surfaces as well as tubular substrates, nanowires and nanorods have been tried as supports for lipid bilayer (Hsieh *et al*., 2012; Huang *et al*., 2007; Misra *et al*., 2009; Sanii *et al*., 2008). However, nanopatterned surfaces generally have local curvatures lower than those required for robust Dyn1 membrane adsorption (1/20nm^{-1}). Highly curved nanorods, such as GalCer lipid rods (Stowell *et al*., 1999), have short submicron length, complicating real time observation of Dyn1 self-assembly. To overcome these problems we designed, in collaboration with Dr. Aleksandr Noy group, a supported lipid bilayer system which combined flat and highly curved parts. We used Peptoid Nanotubes (PNTs) (Jin *et al*., 2018) formed from nanosheets of sequence-defined peptoids by a rolling-up and closure mechanism. PNTs properties, such as wall thickness or diameter, can be easily tuned by varying the number of residues on peptoids resulting in a robust formation of highly curved cylinders (1/20nm^{-1}) suitable for Dyn1 experiments.

The main method used to form the supported lipid bilayers (SLBs) is vesicle fusion (Jass *et al*., 2000; McConnell *et al*., 1986), consisting in the deposition of small unilamellar vesicles (SUVs) on the solid support and subsequent deformation, and formation of a single membrane layer. The lipid spreading method (Nissen *et al*., 1999) is used as an alternative to vesicle fusion in some cases (Sanii *et al*., 2008). This method is based on the hydration of a dried lipid film, resulting in the formation of a multilamellar lipid stack, and spreading out a single lipid bilayer which covers the solid substrate. However, these methods have not been adapted to lipid

mixtures containing highly charged lipid species, such as $PI(4,5)P_2$ required for the Dyn1 adsorption. Here, we adapted the membrane "spill" technique introduced earlier to measure the amount of lipid reservoir deposited on a silica bead (Pucadyil and Schmid, 2010). The lipids were deposited on 40µm silica beads by MLV adsorption followed by drying. Upon rehydration, the beads became covered by lipid bilayer stacks. When brought in contact with a clean glass or a glass-PNT surface (PNTs were deposited onto the glass or mica surface prior to the SLB formation), the lipids spread from the bead forming the bilayer continuously covering the glass and PNTs. The quality of the bilayer was tested by AFM and FRAP (described later in this chapter).

Lipid Nanotubes (NTs)

Lipid nanotubes were formed using lipid covered beads. The steps to obtain NTs were the following:

1. Steps 1-3 from GSBs formation section were followed.
2. SLBs were formed as described earlier.
3. After beads removal from SLBs top, new lipid covered beads were added to the sample and rolled over SLBs. Lipid nanotubes were formed between silica beads.

Protein purification

Dyn1-meGFP plasmid, needed for the production of the protein, was kindly provided by the group of Dr. Sandra L. Schmid from UT Southwestern Medical Centre in Dallas, Texas, USA. Sf9 insect cells were transfected with the plasmid, the produced protein was purified by affinity chromatography through the interaction between Dyn1-mEGFP and recombinant SH3 domains (Neumann *et al*., 2013; Stowell *et al*., 1999). After dialysis, the protein concentration was determined using a commercial BCA protein assay kit. This assay combines the reduction of Cu^{2+} to Cu^{1+} by protein in an alkaline medium with detection of cuprous cation bicinchoninic acid (BCA). Bovine Serum Albumin (BSA) was used as a protein reference to get the standard curve needed to determine the protein concentration. The standard curve and sample values were measured with a plate reader at 562nm.

Molecular Biology

In order to obtain different Dyn1-meGFP mutants, the primers present in table 2.2 were specifically designed. The new protein variants were obtained through the site-directed mutagenesis method. For this purpose, the KOD-Plus-Mutagenesis Kit was used following the

manufacturer´s indications. The correct substitution of the nucleotides was checked by Sanger sequencing.

In-Fusion® HD EcoDry™ Cloning Plus kit was used to obtain the gene substitution, meGFP for mNeonGreen, following the manufacturer´s indications. The gene swap was checked by Sanger sequencing.

Table 2.2. Primers designed for the substitutions made in the proteins used in this work.

Dyn1-meGFP	R399A	FW: 5´-GCAACGGGGCTGTTTACCCCAGACATGG- 3´ RV: 5´-AATGCCATGGATATTCTTGATAGCATAGC-3´
Dyn1-meGFP	I690K	FW: 5´-AAGAACAATACCAAGGAGTTCATCTTCTCG-3´ RV: 5´-CATGAGGTGCATGATGGTCTTGGGC-3´
Dyn1-meGFP	I533A	FW: 5´-GCCATGAAAGGGGGCTCCAAGGAGTACTGG-3´ RV: 5´-GCCAATATTATTGATAGTCAGCCAGCCC-3´
Dyn1-meGFP	K44A	FW: 5´-GCGAGCTCGGTGCTCGAGAATTTCGTAGGC-3´ RV: 5´-GCCGGCGCTCTGGCCGCCCACCACAGCG-3´
Dyn2-meGFP	S619C	FW: 5´-TGTTTCCTCCGAGCTGGCGTCTACCCCG-3´ RV: 5´-GGCCTTCCAGCTGTCCACGTCTTCCTGGG-3´
Dyn1-meGFP	mEGFP → mNeonGreen	FW (vector): 5´-GCGGCCGCACTCGAGTCT-3´ RV (vector): 5´-GAGGTCGAAGGGGGGCCT-3´ FW (insert): 5´-CCCCCCTTCGACCTCATGGTGAGCAAGGGCGAGG-3´ RV (insert): 5´-CTCGAGTGCGGCCGCTTACTTGTACAGCTCGTCCATGCC-3´

Cell culture

COS-7 cells (ATCC® CRL-1651TM) were cultured in DMEM supplemented with 10% fetal bovine serum and 1% penicillin-streptomycin. All cells were maintained in a 37°C incubator supplied with 5% CO_2. For fluorescence microscopy experiments cells were plated in 35 mm glass bottom dishes and transfected with vectors for expression of Dyn1-EGFP and Dyn1-K44A-EGFP (2 µg DNA each) using GeneJuice® Transfection Reagent according to the manufacturer procedure.

Epifluorescence Microscopy

SLBs and NTs imaging

For the visualization of the samples, we used an Eclipse Ti-e inverted microscope equipped with a 100x Oil objective and a Zyla 4.2 sCMOS camera from Andor, controlled by µManager software (Edelstein *et al.*, 2010). A pE-4000 Cooled LED light source was used to illuminate the samples. Light power was controlled to minimize sample photobleaching. We used two different filters, 560/585 (FF560/25 TRITC) filter, to monitor the lipid channel (TR-DHPE), and 485/505 (FF01-485/20 FITC) filter, to monitor the protein channel (Dynamin1 meGFP labeled). Fluorescence pictures were collected at 100ms exposure time.

SLBs fluidity determination mediated by Quantum dots

Supported lipid bilayers were produced as described earlier in this chapter. For this particular experiment, lipid membranes were doped with small amounts of Biotin PC (0.2% mol). Once the SLBs were formed, Qdots™ 705 were added, at a final concentration of 0.1-0.2nM, to the sample. Qdots™ 705 are conjugated with, approximately, 5 to 10 streptavidins per nanocrystal. After 10 minutes of incubation, the excess of Quantum dots present in the bulk of the preparation were washed away. The Biotin PC-Qdots™ 705 interaction allowed us to evaluate the membrane fluidity. The samples were imaged as described in the previous paragraph, a 432/515/595/730 (FF01-432/515/595/730-25) filter was used to monitor the Quantum dot channel. 600 frames were collected at 100ms exposure time and the stack images were analysed using ImageJ (Schindelin *et al.*, 2012) and Icy 2.0 software.

Fluorescence calibration

In order to quantify the total number of Dyn1 molecules implicated in membrane remodelling processes, we performed a fluorescence calibration. This calibration can be, methodologically, separated into two different experiments:

a) Dyn1 helical structure: Based on previous structural Cryo-EM studies done by Jenny Hinshaw´s group (Zhang and Hinshaw, 2001), we designed an experiment to obtain GFP single-molecule fluorescence from dynamin helical structure. Cover glass was cleaned as explained in GSBs formation section, avoiding BSA treatment, and lipid nanotubes (NTs) were formed as explained earlier in this chapter. Dyn1-meGFP was added to the preparation at a final concentration of 0.5µM. After 10 minutes of incubation, the residual protein present in the bulk was carefully washed away to reduce background signal. Protein scaffolds wrapping up lipid nanotubes were imaged at 100msec exposure time and low light power (20%). Images were analysed using ImageJ (Schindelin *et al*., 2012). Background signal was subtracted before single Dyn1-meGFP fluorescence was calculated (all the calculations are explained in the results section).

b) Single-molecule quantification: Due to photo-physical related problems, as dark state, we performed another experiment to get GFP fluorescence quantum and to validate our calibration. Commercially available GFP and Dyn1-meGFP were used to study the fluorescence intensity of a single GFP molecule (Grassart *et al*., 2014a). Borosilicate no. 1 coverslips were prepared as described in GSBs formation section, avoiding BSA treatment step. GFP samples (either commercially available or Dyn1) were diluted in PBS 1X to the nanomolar range (0.5-1nM final concentration). Samples were sonicated for 5s to destroy big aggregates. GFP molecules were imaged at high light power (40%), collected at 1 sec exposure time for 5 minutes until the fluorescence intensity of the molecules reached the background level. Integrated fluorescence intensity and step size from the stepwise bleaching decrease of the molecules were measured using ImageJ (Schindelin *et al*., 2012). Background was subtracted locally to better estimate single-molecule fluorescence. Unitary GFP fluorescence was used as a reference value to quantify the number of dynamins present in our experiments.

Dynamin1 behaviour on different substrates

We focused our study on the behaviour of small dynamin units. To that end, we used different substrates as membrane models. We imaged all the preparations before and after addition of different nucleotides (GTP, GDP, GMPPCP and GDP AlF_4^-) at 1mM final concentration. The membrane models used were the following:

a) Lipid nanotubes: Cover glass and lipid nanotubes were prepared as described earlier. Dyn1-meGFP was added to the sample at 50nM final concentration. Protein incorporation into the nanotubes was followed. Once the first oligomers appeared on the tubes, the excess of

protein was removed to avoid big scaffolds formation. Small oligomers were imaged at low light power (20%) and collected at 100msec exposure time for 1 minute. For this experiment, we performed a fluorescence calibration of the lipid channel. We normalized the fluorescence intensity from the NTs to the mean fluorescence intensity from the supported lipid bilayer to get the radii of the tubes (the calculations are explained in the results section).

b) Supported lipid bilayers: The main purpose of using this model membrane is to study Dyn1 lateral mobility. From previous single-particle tracking experiments performed on a fluorescently labelled (GRP1, different from Dyn1) PH domain we know that, when bound to its target lipid (phosphoinositides) embedded on a supported lipid bilayer, it diffuses at the same rate as a single lipid molecule (Knight and Falke, 2009), which corresponds to 1-10 μ^2/s (Kiessling *et al*., 2006; Schütz *et al*., 1997; Seu *et al*., 2007; Sonnleitner *et al*., 1999; Tamm and McConnell, 1985; Zhang and Granick, 2005). As the number of protein-lipid contacts increase, the diffusion coefficient of the particle decreases. This has been reported using different approaches, such as PH domain multimers, ranging from one to three domains, connected by flexible linkers (Knight *et al*., 2010), or PH fusion proteins capable to dimerize, which showed that when the heterodimer forms, the particle diffuses nearly two-fold more slowly (Ziemba *et al*., 2012). A recent study showed similar results using coarse-grained molecular dynamics simulations (Yamamoto *et al*., 2017). Finally, a study performed with different peripheral protein constructs comprised by one to three domains, including the PH domain, concluded that the number of individual bound lipids and domains that penetrate into the lipid bilayer contribute to the friction against the underlying membrane, defining the diffusion coefficient of the particle (Ziemba and Falke, 2013). Therefore, the mechano-chemistry of small Dyn1 units could be studied attending to their diffusive properties under the constant presence of GTP and their analogues.

   The coverslip and SLBs were prepared as described earlier in this chapter. Dyn1 was added at 50nM final concentration and incubated for 10 minutes. The sample was rinsed with working buffer several times. The preparation was imaged at low light power and collected at 100msec or 1sec for 1 or 3 minutes, depending on the experiment. Stack images were analysed using ImageJ (Schindelin *et al*., 2012) and Icy 2.0.

c) PNTs: The coverslip and SLBs were prepared as described earlier. Dyn1 was added at 0.5µM final concentration and incubated for 10 minutes. The sample was rinsed with working buffer several times. The preparation was imaged at low light power and collected at 100msec for 1 minute. Stack images were analysed using ImageJ (Schindelin *et al*., 2012).

Confocal Microscopy

Fluorescence Recovery After Photobleaching (FRAP)

In order to study the fluidity of the supported bilayers, we performed FRAP experiments. Glass support and bilayers were prepared as previously described. We used a TCS SP5 II Confocal microscope equipped with a 63X water immersion objective. The image format was 512x512 pixels, 400 Hz scan speed and 111.48µm pinhole. We stablished a bleach point into the lipid bilayer, and we used an argon laser at 543nm, 85% power, for 10 minutes to completely bleach the central region of the membrane. Laser power was reduced to 17% and a PMT detector (stablished between 555-695nm, with an 850 V gain) was used to follow the fluorescence recovery each minute for the next 45 minutes after photobleaching. ImageJ (Schindelin *et al*., 2012) was used to analyse the stack images.

Number and Brightness (N&B)

Another way we used to quantify the total number of dynamin molecules implicated in the fission process was number and brightness technique. 35 mm cell imaging dish with a glass bottom was used as a support for the SLB formation. Cell dish was cleaned as coverslips used in the rest of the experiments. SLBs were formed as described before and Dyn1-mEGFP was added at 50nM final concentration. The protein was incubated for 10 minutes and it was washed before imaging. We used a TCS SP8 Confocal microscope equipped with a 63X oil immersion objective. The image format was 512x512 pixels, 200 Hz scan speed, 2.43µs pixel dwell time, 0.775/s frame rate and 84µm pinhole. We used an argon laser at 488nm, 8% power, to excite the fluorophores. A HyD detector in photon-counting mode (stablished between 500-580nm) was used to collect fluorescence emission. 200 frames were recorded before and after GTP addition at 1mM final concentration. ImageJ (Schindelin *et al*., 2012) and Imaris 7.4 were used to analyse the stack images.

For the experiments carried out with Cos-7 cells, they were cultured and transfected as described in cell culture section.

Cryo-EM Microscopy

To study membrane remodelling properties of Dyn1-meGFP we performed a tubulation assay. To that end, 400nm LUVs, at 300µM final concentration, were produced as described in LUVs formation section. LUVs were incubated overnight at room temperature with Dyn1-mEGFP at 0.5µM final concentration in a final volume of 50µL. Another sample of LUVs was incubated with Dyn1 WT under the same conditions as a control. Samples were vitrified in liquid nitrogen and

imaged with a field emission scanning electron microscope at 200kV and 40000x detector magnification.

Atomic Force Microscopy

Supported lipid bilayers quality was characterized using different techniques. Atomic Force Microscopy (AFM) was used to measure membranes topography. Samples were prepared on glass, instead of mica. Cover glass and SLBs were prepared as described in GSBs and SLBs formation sections, respectively. Due to sample softness, spring constants of the cantilevers, used to scan the samples, ranged between 0.01-0.1 N/m. Samples were scanned in contact or tapping mode, depending on substrate stiffness, using a JPK Nanowizard AFM 3 microscope. JPK Data Processing software was used to analyse the scans.

GTPase assay

Biochemical activity of Dyn1-meGFP was assayed and compared with Dyn1 WT to check how the presence of the fluorophore affects its GTPase activity. We quantified basal and liposome stimulated GTPase activities of both proteins using Malachite green to measure free phosphate, as described in (Leonard *et al*., 2005). For liposome stimulated GTPase activity, Dyn1-mEGFP (0.5µM final concentration) was incubated in presence of 100nm LUVs (150µM final concentration) for 30 minutes at 37°C. After liposome stimulation, GTP (1mM final concentration) was added to basal and stimulated preparations for 1 hour at 37°C. GTP hydrolysis was stopped adding EDTA at 100mM final concentration. 150µL of Malachite green were added to the reaction and the absorbance was measured at 650nm in a plate reader. Free phosphate was calculated using as a reference a standard curve ranging from 0-100µM Pi.

Chapter 3:

Creation and characterization of membrane templates of different curvature and topology

Overview of the templates and their purposes

Our main goal was to assess membrane-remodelling activities of small, subhelical Dyn1 oligomers. In the cell, such oligomers bind only weakly to low-curved membranes of CCPs and very efficiently to emergent highly curved necks of CCV (see Figure 1.1). To mimic this physiological situation, we designed membrane templates having low- and highly curved parts. We created two types of such templates (Figure 3.1). The first consisted of a supported lipid bilayer (SLB) deposited over a glass (or mica) surface with prebound peptoid nanotubes (PNTs).

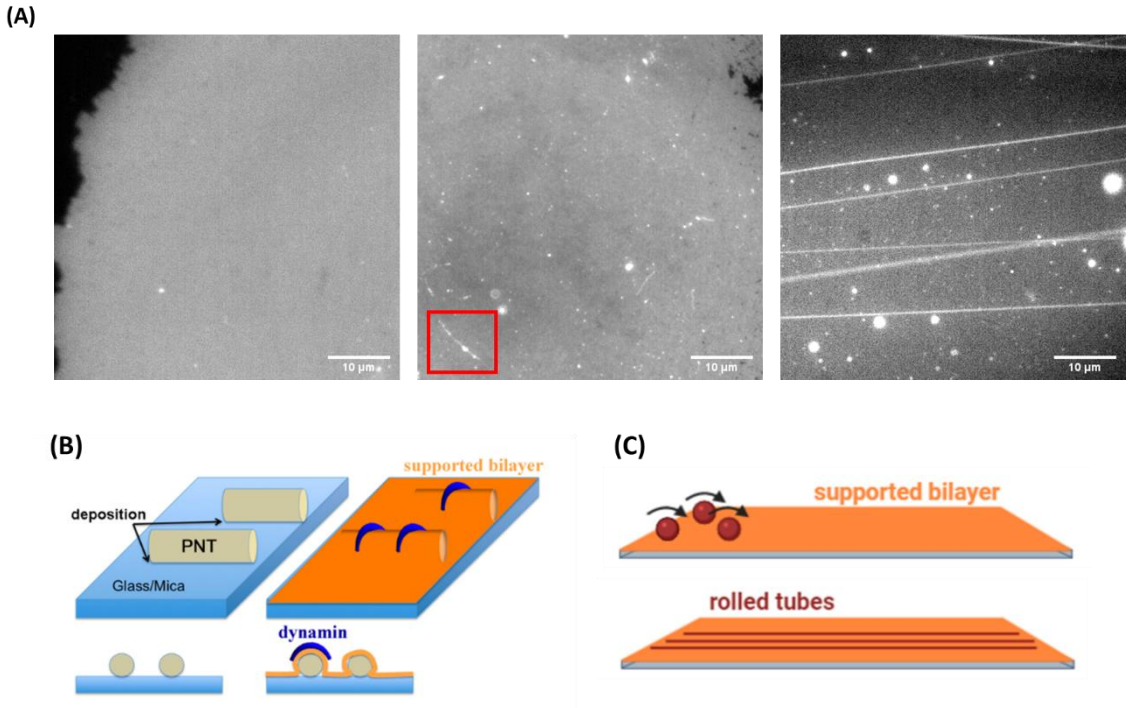

Figure 3.1 Membrane templates of different curvature and topology. (A) Widefield fluorescence microscopy images of the different lipid templates used in this work. From left to right, a supported lipid bilayer (SLB) formed from DOPC:DOPS:Chol:PI(4,5)P_2:TR-DHPE, a SLB-PNT template, and a bunch of lipid NTs over a SLB. The ROI in the second image highlights a PNT deposited on the coverslip and covered by the SLB. (B) Schematic representation of the SLB-PNT template creation. (C) Schematic representation of the rolled tubes formation.

The SLB, continuous over the complex support, combined the flat parts attached to the glass and highly curved (mean curvature 20nm^{-1}) parts attached to the PNTs. This template was designed and engineered by our collaborators, Dr. Aleksandr Noy´s group in LLNL (Livermore, USA). We developed a new method of the SLB deposition on this template enabling robust

incorporation of highly charged lipid species (see the Methods above). As PNTs were firmly bound to the flat surface, the SLB parts over the PNT had approximately half-cylinder shape (Figure 3.1 B). Nowhere on the SLB-PNT template could Dyn1 form a helix, so that this template allowed interrogating membrane activities, such as curvature sensing, of non-helical Dyn1 oligomers. To assess the membrane curvature-creation by such oligomers, we designed the second type of the templates, the one combining SLBs and lipid membrane nanotubes (Figure 3.1 C). The nanotubes (NTs) were formed over the SLB by "rolling" silica beads covered by preformed lipid stacks over the SLB patches using a custom-designed microfluidic chip ((Dar *et al*., 2017; Martinez Galvez *et al*., 2020), see also the Method section). The NTs stuck to SLBs via "hot-spot" defects in the bilayer and remained firmly bound to the SLB upon termination of the flux in the microfluidic chip. Dyn1 binding to the NT and the flat SLB could be simultaneously quantified by the single-molecule fluorescence microscopy (Figure 3.1 A). Besides characterizing the curvature dependence of Dyn1 binding, the SLB-NT system also enabled quantifying the stoichiometry of Dyn1 oligomers producing the NT fission in the presence of GTP. The methodological details of the templates' creation are described in the corresponding sections of Chapter 2. Below, we described how we checked the essential parameters of the templates, such as fluidity, curvature, and topography, to confirm that the new method of SLB deposition used here robustly yields SLB-NT and SLB-PNT templates suitable for Dyn1 experiments.

Characterization of the templates: topography, curvature, and fluidity

First, we assessed the topography of the SLB-NT and the SLB-PNT templates by Atomic Force Microscopy (AFM). A typical AFM image showing an SLB patch formed on a glass substrate is shown on Figure 3.2 A. We could not resolve the NT over the SLB due to the extreme softness of the NTs and the overall weak attachment of the NT to the SLB. Yet, we occasionally resolved the NTs crashed over the glass substrate near the SLB edge (Figure 3.2 A). The bilayer structure was confirmed by the measurements of the height of the SLB edge. The height profiles obtained by scanning across holes in the SLB (Figure 3.2 B) confirmed that the SLB thickness was around 4 nm, characteristic for a single lipid bilayer. The SLB-PNT system was analysed by High-Speed AFM (HS AFM), the experiments being carried out while visiting Dr. Aleksandr Noy´s group in Livermore, USA. HS AFM imaging showed that individual PNTs as well as small PNT aggregates laid flat on the mica support (Figure 3.2 C, inset). Analysis of the cross-sectional height profiles revealed the peak heights of 20-25nm, corresponding to the PNT diameter (Figure 3.2 C). Further comparison of the bare and lipid-covered PNTs confirmed systematic ~4nm increase of the peak height due to the lipid bilayer coverage.

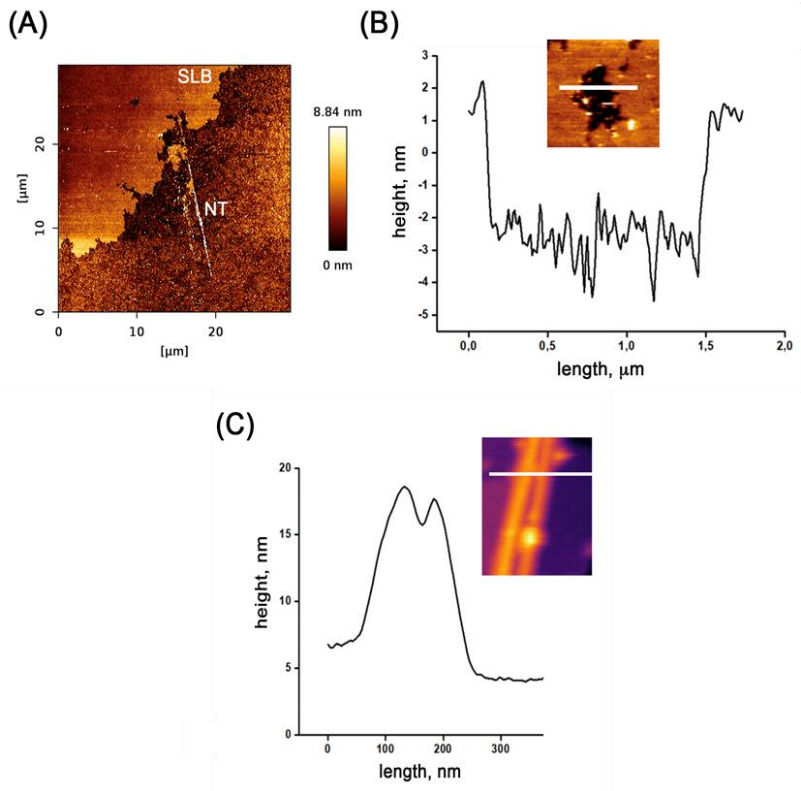

Figure 3.2 Atomic Force Microscopy (AFM) scans performed on the membrane templates. (A) A representative raw AFM image of a SLB-NT template, the lipid composition is DOPC:DOPS:Chol:PI(4,5)P_2:TR-DHPE. (B) The SLB thickness was verified from the scans across the hole defects, the graph shows the height profile taken from the scan along the white line shown in the inset AFM image. (C) An HS AFM image (inset) and the height profile (along the white line in the inset) of a PNT pair in the SLB-PNT template; 0 height corresponds to the mica surface.

Once we analysed the topography of the templates, we performed fluorescence recovery after photobleaching (FRAP) experiments to assess the fluidity of the SLB formed. We observed robust recovery of the membrane fluorescence upon bleaching a circular membrane region using a standard confocal microscopy protocol (Figure 3.3). The fluorescence plateaued at 0.54±0.07 (SD, n=4) of its initial value, corresponding to the complete recovery of the fluorescence coming from a single (upper) monolayer of the SLB. The lipid diffusion coefficient, estimated from the recovery half-time ($t_{1/2}$) as $D=0.22r^2/t_{1/2}$ (where r is the radius of the bleaching beam, (Soumpasis, 1983)), was equal 0.56±0.31 $\mu m^2/s$ (SD n=3), in the range reported for the SLBs formed on glass (Sterling *et al*., 2015).

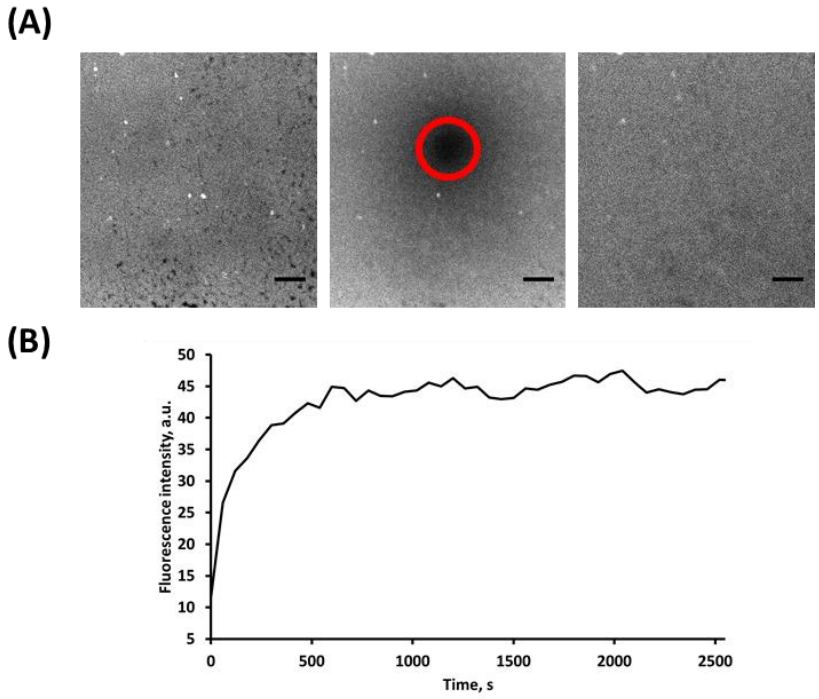

Figure 3.3 FRAP on the membrane templates. (A). The confocal fluorescence microscopy images showing an SLB region before bleaching, right after bleaching and upon partial recovery. Red circle marks the bleached region. Scale bar, 10µm. (B) The fluorescence intensity curve (integrated over the circular ROI showed by the red circle in (A)) showing kinetics of the recovery.

To specifically assess the mobility of lipids in the upper monolayer of the SLB we applied the particle tracking technique. We doped the SLBs with small amounts (0.2 mol%) of Biotin PC and added streptavidin conjugated quantum dots (Qdots) (5-10 molecules per Qdot) (Figure 3.4 A). Stepwise trajectories of the Qdots (Figure 3.4 B) were obtained using particle tracking algorithm of the ImageJ and Icy software packages (see Methods). At each trajectory step, the square displacement (r^2) was calculated as:

$$r^2 = (x_1 - x_0)^2 + (y_1 - y_0)^2$$

where (x_0, y_0) and (x_1, y_1) are the Qdot coordinate at the beginning and end of each step.

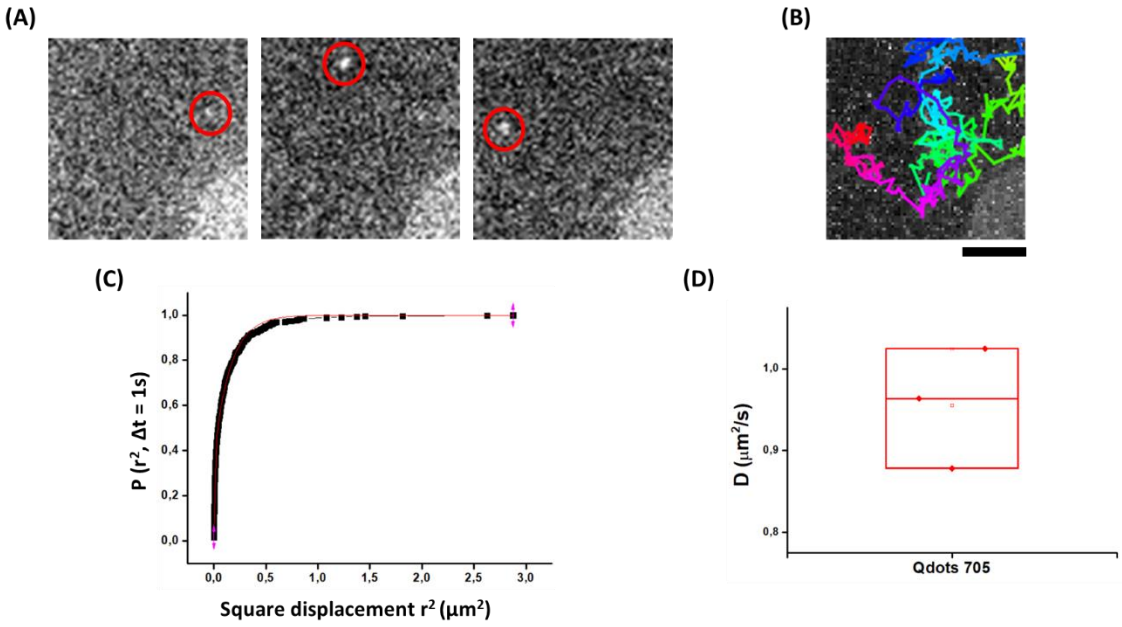

Figure 3.4 Lipid mobility determination. (A) Frame sequence (10fps) showing Qdot705 mobility at times 0, 30, 60s. Red circles mark the position of the Qdot705 at each snapshot. (B) STD Z projection from the previous sequence, with the Qdot705 trajectory, reconstructed from 600 localizations, overlapped, scale bar 1µm. The colour represents time, from 0s (green) to 60s (red). (C) Cumulative probability distribution function of square displacements P (r^2, Δt) for Δt = 10 msec, red solid line represents two-component model fit. (D) Diffusion constants obtained from the previous analysis.

The cumulative probability distribution of the square displacements P (r^2, Δt) was fitted to either a single-component or a two-component diffusion model using the following equation (Schütz *et al*., 1997):

$$P(r^2, \Delta t) = 1 - \varepsilon_1 e^{-\frac{r^2}{4D_1 \Delta t}} - \varepsilon_2 e^{-\frac{r^2}{4D_2 \Delta t}},$$

where D_1 and D_2 represent the diffusion constants, and ε_1 and ε_2 represent the weighting factors, which refer to the fractions of time a particle undergoes diffusion with the corresponding diffusion constant, with $\varepsilon_1 + \varepsilon_2 = 1$ (Hsieh *et al*., 2014) (Figure 3.4 C). We used weighted diffusion constant $D_w = (D_1 * \varepsilon_1) + (D_2 * \varepsilon_2)$ as the output (Figure 3.4 D). As expected, the Qdot experiments reported on average higher D values than did the FRAP experiments, confirming unrestricted lipid mobility in the upper monolayer of the SLB.

We finished characterizing the SLB-NT template by quantifying the NT curvature. As AFM failed to resolve the NTs, we used the membrane fluorescence intensity integrated over the NT of a given length as the measure of its radius (Kunding *et al*., 2008). For that, we first determined the

relation between the fluorescence intensity and the membrane area using the SLBs containing the same concentration of a lipid fluorescence probe as the NTs (Dar *et al*., 2015, 2017). To obtain the calibration constant, we used regions of interest (ROIs) of different sizes (Figure 3.5 A).

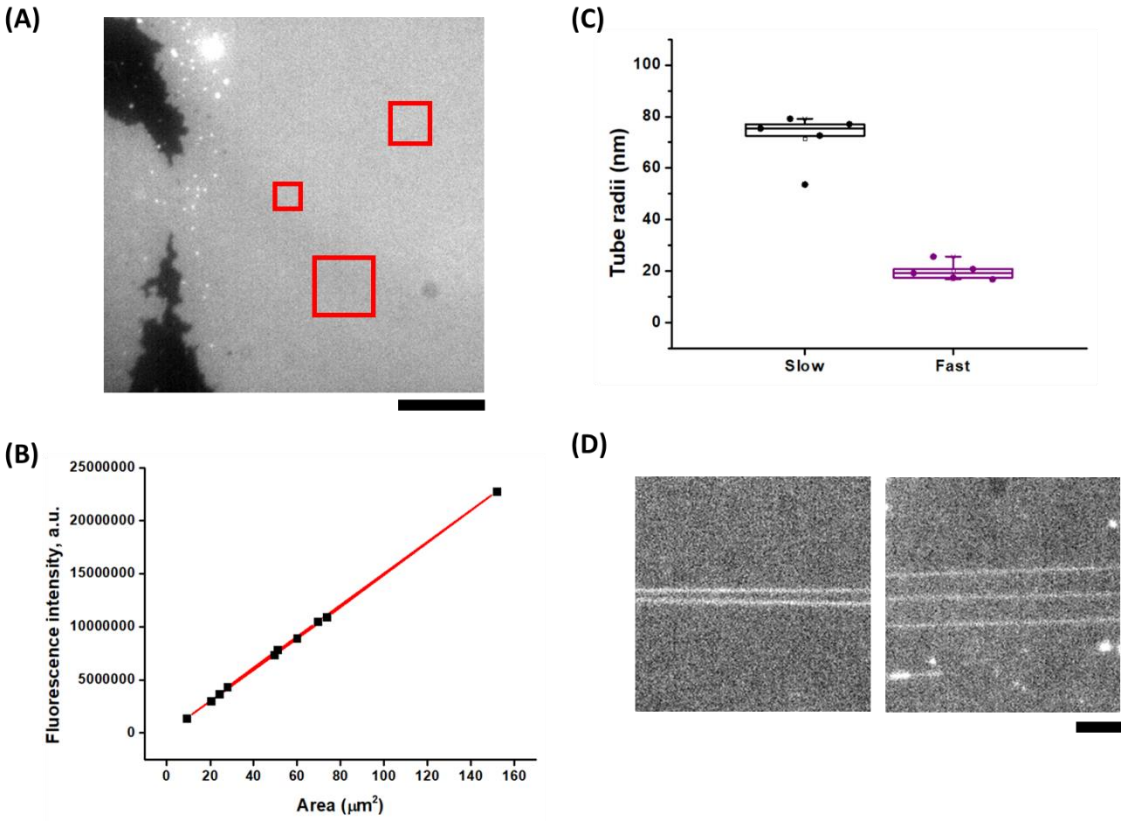

Figure 3.5. Lipid nanotubes radius determination. (A) Fluorescence image of a SLB. Red squares represent the different ROIs used to perform the fluorescence per area calibration. Scale bar 10 μm. (B) Total fluorescence intensity per area unit from the ROIs in (A). (C) Box plots showing the distribution of NTs radius obtained from different rolling speeds. (D) Fluorescence images of a bunch of NTs formed over a SLB, using the silica beads rolling method. From left to right, thick NTs, obtained rolling slowly the silica beads, and thin NTs, obtained rolling fast. Scale bar 5 μm.

We calculated the total fluorescence intensity for each ROI, I_{ROI}, and plotted it as a function of the ROI area, A (Figure 3.5 B). The calibration constant δ was found from linear regression of the I_{roi}(A) dependence (Figure 3.5 B, red line). Then, assuming that the calibration constant does not depend on membrane curvature (Dar *et al*., 2015, 2017; Espadas *et al*., 2019), we obtained the nanotube radius R_{NT} as:

$$R_{NT} = I_{NT} / 2 * \pi * \delta * L_{NT}$$

where I_{NT} is the total membrane fluorescence of the NT of the length L_{NT}. We found that the NT radius depended on the speed of the flux used in the NT production. The weak flux producing slow movements of the lipid-containing beads over the SLB resulted in thick NTs while faster beads movement resulted in thinner tubes, with curvatures equivalent to that of the SLB-PNT system and of the CCV necks (Figure 3.5 C, D). This thin NTs were further used in Dyn1 experiments described below.

Discussion

We introduce here two novel membrane templates, SLB-PNT and SLN-NT, suitable for *in vitro* reconstitution and mechanistic analyses of the membrane remodelling activities of cellular proteins. Each template serves distinct purposes. The SLB-PNT has fixed, rigid topology and can be used to analyse curvature sensing by proteins, other effects of membrane curvature on protein binding and membrane activities as well as protein sorting in curvature gradients. The local topography of the SLB-PNT template is different from typical solid nanopatterned surfaces (such as wavy glass (Hsieh *et al*., 2012)). It presents well defined cylindrical geometry in the curved parts. The well-defined topology is critical for reconstruction of protein self-assembly, e.g., formation of cylindrical protein cages typical for intracellular filaments and protein helices, such as Dyn1 helix. Notably, while free-standing PNTs can support full-scale cylindrical self-assembly, the SLB-PNT system enables uncoupling longitudinal and lateral interactions and thus untangle multiple competing self-assembly pathways, as we show below for Dyn1.

The SLB topology could be modified by incorporation of nanoengineered templates different from PNTs, e.g., elastomers (Sanii *et al*., 2008) or silicon nanowires (SiNW) (Misra *et al*., 2009). However, the relatively low curvature and high size variability of such structures made them inappropriate for our purposes. In a different approach, highly curved cylindrical topology of PNTs can be created using lipid-based nanorod made of galactocerebrosides (Stowell *et al*., 1999). When supplemented with a small amount of PI(4,5)P_2, the GalCer rods were used to study the reorganization of the Dyn1 helix at the single-protein level (Colom *et al*., 2017b). However, the surface properties of the rigid rods are far from those of a fluid lipid bilayer, potentially interfering with the membrane insertion and lateral mobility of small Dyn1 oligomers. Besides, the geometry of the PNTs can be modified and fine-tuned (Jin *et al*., 2018), greatly expanding their versatility and applicability to membrane transformations of different length and curvature scales.

To deposit the SLB on the glass or mica surface with prebound PNTs we used a novel procedure based upon previously observed spreading (spilling) of lipids from a lipid-covered silica bead to a glass surface upon establishing a contact between the glass and bead (Pucadyil and Schmid, 2010). The main advantage of the spill method over other SLB formation methodologies, such as SUVs deposition (Jass *et al*., 2000; McConnell *et al*., 1986), is the fast and robust formation of the SLBs containing highly charged lipid species. Besides, the spill method yields many small (100s of μm^2, dependently on the amount of lipids available on the silica beads) SLBs, which might facilitate certain type of experiments, such as parallel interrogation of multiple protein

species. One critical step for the formation of SLBs is the pre-cleaning of the glass support, coverslips in our case. Plasma cleaning, of the ethanol sonicated glass, for just 15-30 seconds greatly facilitates formation the SLBs. Though AFM scanning of the SLBs revealed the presence of imperfections, such as holes, our FRAP experiments showed that lipids displayed seemingly unrestricted lateral mobility in the SLB-PNT templates.

To analyse the lateral mobility of small molecular clusters mimicking Dyn1 oligomers we used polyvalent Qdots interacting with multiple biotin-bearing lipids in the SLB. To assess their lateral mobility we performed single particle tracking (SPT) experiments (Chang *et al*., 2008). The main advantages of using Qdots on these experiments are their high photostability and brightness, making them good candidates for long timescale imaging. However, these semiconductor nanocrystals present one clear disadvantage front other fluorescent probes, their photoluminescence intermittency known as blinking (Efros and Nesbitt, 2016), which can make difficult, sometimes, particle tracking recording. Even taking all these issues into account, we considered Qdots good reporters of individual lipids mobility. In fact, the diffusion constants obtained from the trajectories derived from Qdots movement, coincide with lipid diffusion constants reported by others (ranging from 1-10 $\mu m^2/s$) (Kiessling *et al*., 2006; Seu *et al*., 2007; Sonnleitner *et al*., 1999; Tamm and McConnell, 1985; Zhang and Granick, 2005). Moreover, if we consider that the Qdots used in that study were conjugated with 5-10 streptavidin molecules, we could not discard the simultaneous interaction of a single Qdot with two or more lipid species, slowing down the mobility of the particle in the bilayer (Knight *et al*., 2010; Ziemba and Falke, 2013).

Finally, lipid-covered silica beads served us for a purpose completely different from the SLB deposition. By rolling the beads over the SLB-covered surface we created lipid nanotubes stably attached to the SLB. This method is a modification of the supported membrane tube assay system (SMrTs) (Dar *et al*., 2015, 2017). The major novelty we introduced is in the preparation of the flat support for the NTs. Pure lipid NTs crash upon interacting with a bare glass. To avoid the NT rupture, SMrTs uses the surface passivation which requires substantial time and expertise to complete. Instead of chemical passivation, we use preformed SLB patches. The fission experiments (see Chapter 5 below) showed that the NT attach to the SLB in a few hot spots, while most of the NT remains intact and available for the protein, thus closely resembling SMrTs. Importantly, we found that the NT curvature can be tuned by changing the speed of the NT formation (Figure 3.5 C), with thin NTs almost perfectly mimicking the natural curvatures of the CCV necks (Kosaka and Ikeda, 1983). Finally, the clear advantage of the SLB-NT system is the ability to simultaneously monitor protein interactions with flat and curve membranes. We could

even create a PNT-SLB template and then roll beads over it, thus testing a protein of interest with membranes of different, yet precisely controlled curvature and topology.

Chapter 4:

Determination of the stoichiometry of Dyn1 oligomers bound to flat SLB

To monitor Dyn1 interaction with SLB-PNT and SLB-NT templates we used Dyn1 conjugated with monomeric enhanced GFP (Dyn1-meGFP construct). To quantify the number of Dyn1-meGFP in the oligomers bound to these membrane templates, we used the fluorescence intensity distribution measured for a single GFP molecule. To obtain and verify the distribution we used three different approaches. First, we directly measured the fluorescence intensity of pure GFP molecules (0.5-1 nM in the bulk) bound to a pre-cleaned coverslip (Fig. 4.1A, inset, see materials and methods chapter for more details).

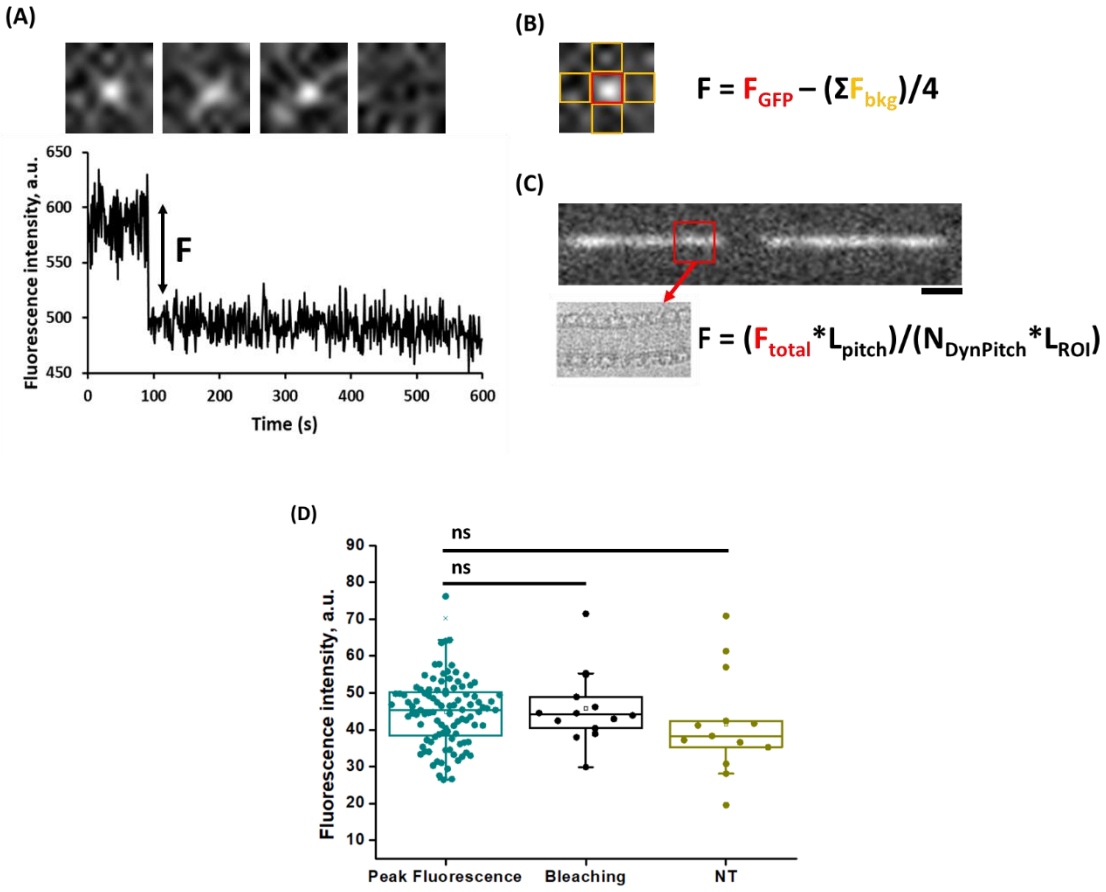

Figure 4.1 Determination of the mean fluorescence intensity of the single GFP. (A) Frame sequence showing bleaching of a single GFP molecule and its corresponding plot profile showing stepwise behaviour of the fluorescence decay. The fluorescence intensity of the molecule is calculated as the difference between the two levels. (B) Single GFP molecule, yellow squares represent selected regions to calculate the subtracted background and the red square marks the GFP molecule. (C) Dyn1-meGFP scaffold assembled on a lipid NT and a cryo-EM picture showing membrane tubulation by the labelled protein. (D) Boxplots showing the distribution of single GFP molecule fluorescence intensities measured from the

three different methods exemplified in (A), (B), and (C). Statistical significance was calculated according to One-way ANOVA (n=100, n=14, n=13, respectively).

We measured a total fluorescence from square ROI including the GFP (Fig. 4.1B, red square) and further subtracted the average fluorescence obtained from four adjacent ROIs of the same size (Fig. 4.1B, yellow squares). Second, we detected the stepwise GFP bleaching events. At the low bulk concentration used, most of the detected bright spots showed distinct bleaching steps (Fig. 4.1A). The step amplitude was used as the second measure of the unitary GFP fluorescence. Third, we used the fluorescence of Dyn1-meGFP helix. We added Dyn1-meGFP to NTs at high concentration (0.5 µM) so that the protein formed microns long helical scaffolds on the NT (Fig. 4.1C). For the scaffold of the length L, we calculated the total number of Dyn1-meGFP (N_{dyn}) using the helical pitch and the number of molecules per helical turn determined by cryo-EM (Zhang and Hinshaw, 2001):

$$N_{dyn} = L / \text{pitch} * \#\text{Dyn1} / \text{turn}$$

Once we knew the number of dynamins per scaffold, we calculated the total fluorescence intensity of the scaffold, subtracted the background, and divided the resultant fluorescence intensity by the total number of proteins. Finally, we compared the fluorescence intensity per molecule obtained by the three different approaches. Figure 4.1D shows that the three approaches converged relatively well, thus yielding a reliable measure for the single GFP fluorescence at a given excitation intensity (and camera parameters).

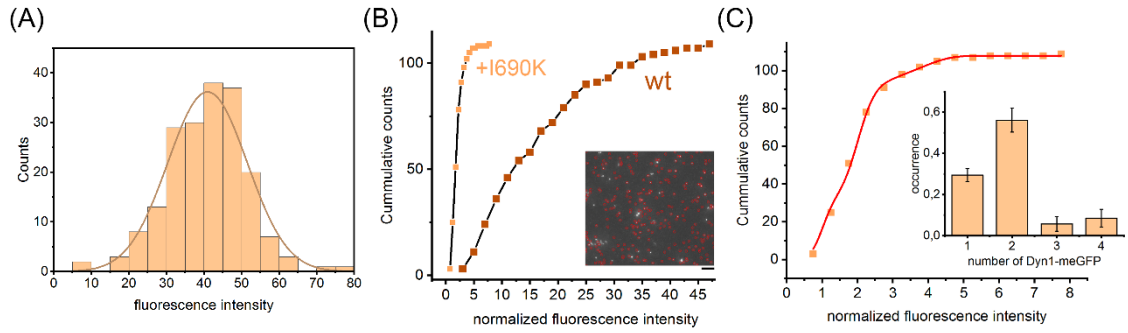

Figure 4.2 The procedure for the stoichiometric analysis of Dyn1-meGFP clusters. (A) The distribution of the single GFP fluorescence intensity. (B) Cumulative probability distribution of the fluorescence intensity of Dyn1-meGFP oligomers (wt) and the oligomers obtained from 1:1 (mol/mol) mixture of Dyn1-meGFP and I690K mutant of Dyn1 (+I690K). The fluorescence intensity was normalized to the mean GFP

fluorescence (from (A)). The inset shows the fluorescence microscopy image of the Dyn1-meGFP oligomers detected by the particle detection algorithm of Icy software package (red circles). Scale bar, 5 µm. (C) Cumulative distribution of the Dyn1-meGFP+I690K oligomers (squares) fitted with the sum of normal distributions calculated for individual oligomer species, their size ranging from 1 to 6 (solid line). The inset shows the relative contribution of each individual species into the distribution.

After obtaining this verification, we characterized the fluorescence intensity distribution measured for the single GFP molecule (Fig. 4.2A). The distribution was normal following Anderson-Darling test (A^2=0.51, Fig. 4.2A). The distribution can be used to deconvolve the intensity distributions obtained from Dyn1-meGFP clusters assuming that all of the GFP molecules fluoresce independently, with the intensity distribution shown in Fig. 4.2A (Schmidt, 1996; Schmidt *et al*., 1996; Subburaj *et al*., 2015). Namely, the cumulative distribution obtained from the clusters could be fitted with a linear combination of the distributions $\sum_n(A_n normalCDF(n, \sigma_n))$, where $\sigma_n = (\frac{\sqrt{n}\sigma_{GFP}}{f_{GFP}})$, f_{GFP} and σ_{GFP} are the mean and variance of the distribution of the single GFP fluorescence intensity (Fig. 4.2A). Each distribution characterizes the fluorescence intensity of a Dyn1-meGFP oligomer containing exactly **n** Dyn1-meGFP molecules, with A_n characterizing the contribution of the oligomer into the total distribution (and thus the oligomer occurrence in the population).

To test the deconvolution procedure, we tried it on the Dyn1-meGFP oligomers bound to flat SLB. We added Dyn1-meGFP (50nM in the bulk) to the SLB and incubated for 5 min. After washing out the excess of the protein, we could detect individual Dyn1-meGFP clusters bound to the SLB (Fig. 4.2B, inset). The distribution of their fluorescence intensities, normalized to the mean fluorescence of GFP, indicated that the clusters are mostly subhelical (<30 molecules forming a single rung of 1-start Dyn1 helix, (Zhang and Hinshaw, 2001)) species (Fig. 4.2B, wt). Addition of I690K mutant, 1:1 (mol/mol) to Dyn1-meGFP, caused dramatic reduction of the cluster intensity (Fig. 4.2B, +I690K). We next fitted the cumulative distribution of the intensity of this small clusters using the above linear combination of distributions. We found that formation of the oligomers larger than dimers were strongly inhibited, in agreement with I690K phenotype detected *in vitro* and *in vivo* (Kenniston and Lemmon, 2010; Sever *et al*., 2006; Song *et al*., 2004).

Finally, we assessed for the effect of bleaching on our measurements. We found that the bleaching is minimal in low-intensity particles studied in Dyn1 experiments (Fig. 4.3). However,

we took the uncertainties associated with the bleaching into account while interpreting the experiments described below.

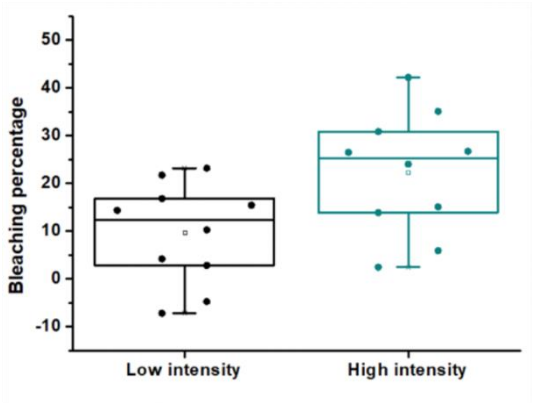

Figure 4.3 Boxplot showing the bleaching percentage on consecutive sample recordings.

About a half of Dyn1-meGFP oligomers bound to planar SLB are smaller than decamers (Fig. 4.2B), the number corresponding to 1/3 of the rung of the 1 start Dyn1 helix (Zhang and Hinshaw, 2001). Equally small oligomers of Dyn2 were earlier associated with HIV viral infection (Jones *et al*., 2017), indicating their physiological relevance. Following this finding, we were curious whether Dyn1 could form similar low-number oligomer species in the cell.

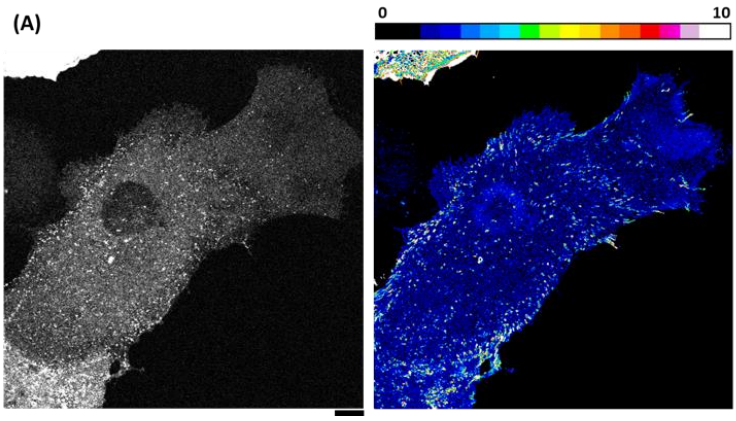

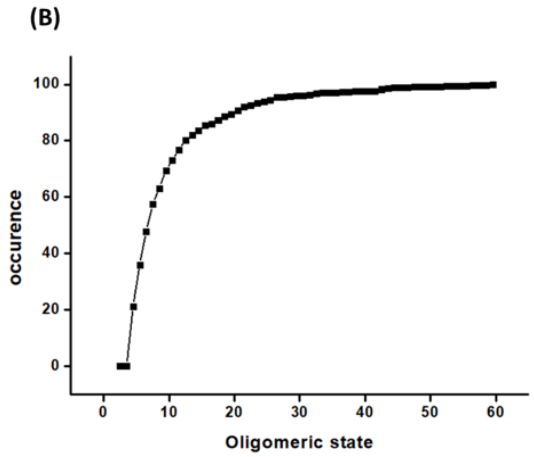

Figure 4.4 Dyn1-EGFP oligomeric state in cells. (A) Confocal image of a Cos-7 cell transfected with Dyn1-EGFP and its brightness image transformation. Scale bar, 10 µm. The colour code on top of the brightness image corresponds to the different values of brightness. (B) Cumulative probability distribution of the Dyn1-EGFP oligomeric state.

We chose Cos-7 cells for their large size and firm adhesion to the bottom of the observation chamber creating a large chunks of flat plasma membrane resembling SLB. We transfected Cos-7 cells with a plasmid containing Dyn1-eGFP and imaged the transfected cells using a SP8 confocal microscope at low laser power and in the photon counting mode (see materials and methods chapter for more details). We transformed the acquired fluorescence images into a brightness image (Fig. 4.4A). To estimate the relative monomer value, we applied a mask on the brightness image to remove all the brighter spots. Once we knew the corresponding value for the monomer, we quantified the oligomeric state of the spots similarly as in *in vitro* experiments. We divided the brightness value of the spots by the value of the monomer. Then, we plotted the oligomeric state of the bright foci as a cumulative probability distribution (Fig. 4.4B). Striking similarity of the cluster size distribution obtained *in vitro* (Fig. 4.2B) and *in vivo* (Fig 4.4B) confirm that small non-helical Dyn1 oligomers bind to flat or low curved membranes and have a preferred stoichiometry, likely corresponding to their molecular architecture (see Chapter 5 and 6 below).

Finally, we tested whether the GFP attachment alter the helical self-assembly of Dyn1 assumed in the calibration experiments (Fig. 4.1C). For that we first compared the assembly stimulated GTPase activity (normalized to basal GTPase activity) of the wild-type and the GFP labelled proteins. We revealed that the GFP attachment impaired, yet not critically, the GTPase activity of Dyn1 relying on helical self-assembly (Fig. 4.5A). Next, we performed membrane tubulation

assay using large unilamellar vesicles. We found that GFP did not critically affected the Dyn1 ability to transform spherical LUVs into tubular structures covered by the protein helix (Fig. 4.5B). We conclude that the Dyn1-meGFP construct can be used to visualize and study the mechano-chemistry of the non-helical assemblies of Dyn1.

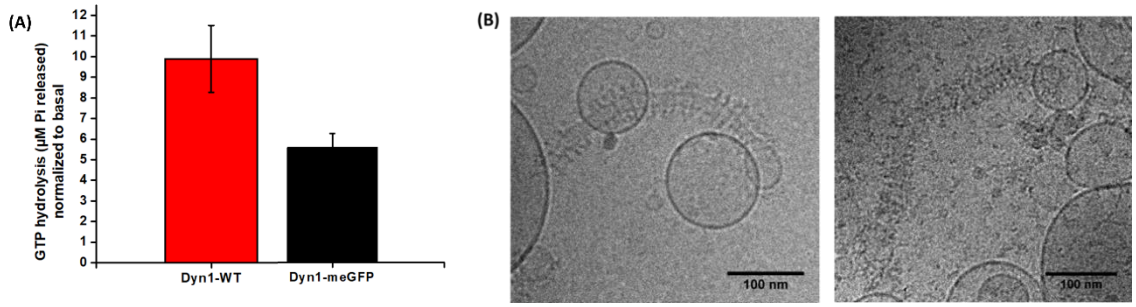

Figure 4.5 Dyn1-meGFP characterization. (A) Liposome-stimulated GTPase activities (normalized to basal GTPase activity) of Dyn1-WT and Dyn1-meGFP (n=5 and n=3, respectively). Liposomes, formed from DOPC:DOPS:DOPE:Chol:PI(4,5)P_2, were incubated with the proteins for 15 minutes. The phosphate release was measured after 1 hour incubation of the proteins with GTP. (B) Cryo-EM images showing membrane tubulation by Dyn1-WT, on the left, and Dyn1-meGFP, on the right.

Discussion

Since the demonstration that GFP could be used as a tool to study protein distribution and dynamics in living cells (Chalfie *et al*., 1994), the usage of the fluorescent proteins (FPs) for stoichiometric analyses of intracellular and *in vitro* proteomes has increased exponentially. Nowadays, due to recent advances in genome editing (Chen *et al*., 2013; Chiu *et al*., 2013), studying FP-conjugated proteins at physiological expression levels becomes a routine. However, the attachment of an FP to a protein of interest also has undesirable consequences. For example, GFP, one of the most widely used fluorophores, is a large molecule (~27 kDa) (Prasher *et al*., 1992) which can interfere with the target protein structure and functions. GFP and their variants have been widely used in different investigations monitoring protein localization and/or function. GFP was the first FP cloned for life imaging purposes (Prasher *et al*., 1992) and it remains one of the best characterized FPs. Nevertheless, different groups reported protein malfunction related to the GFP-tagging (Chudakov *et al*., 2010; Meyer *et al*., 2007; Zhang *et al*., 2014). Quite recently, it was shown that attaching GFP to either the N- or C-terminus of the dynamin-related protein 1 (Drp1) alters its functions (Montecinos-Franjola *et al*., 2020). However, since the first introduction of the FP labelling, various strategies aimed at avoiding steric, structural, and functional interferences from the FP label have been developed. For example, choosing between N- and C-terminus of the protein for the FP placement, insertion of a flexible linker between the FP and the protein of interest or even inclusion of the FP inside the protein could help creating a fully functional protein construct (Baehler *et al*., 2002; Moradpour *et al*., 2004; Rocheleau *et al*., 2003). In this respect, Dynamin-GFP conjugates have been proven to retain their functionality in various cellular contexts. They were successfully applied to reveal the presence of dynamin at actin tails (Lee and De Camilli, 2002), the recruitment of Dyn1 to clathrin-coated pits (Merrifield *et al*., 2002), or Dyn2 role in HIV-1 fusion pore stabilization at low oligomeric state (Jones *et al*., 2017). Here, for the first time, we systematically tested Dyn1-meGFP behaviour also behaves relatively well in the *in vitro* context. Though we found that GFP attachment did impair the stimulated GTPase activity of the protein (Figure 4.5 A), it nevertheless retained major characteristics and functions of the wild-type protein, such as GTP-induced GG dimerization, GTP-dependent membrane insertion and recycling and, most important, membrane fission (see Chapters 5-6 below). We conclude that Dyn1-meGFP can be used in functional reconstitution assays, yet the effects of the bulk GFP tag are better verified by a label-independent technique, such as AFM used here.

One of the most challenging applications of FPs is the stoichiometric analysis of oligomeric protein machineries, such as Dyn1 (Antonny *et al*., 2016). Two independent groups utilized

Dyn2-EGFP in quantitative fluorescence microscopy to reveal that a single helical ring of dynamin is sufficient to mediate membrane fission (Cocucci *et al*., 2014; Grassart *et al*., 2014a). Using FPs, and GFP in particular, for stoichiometric assessments shall be done with much caution. The first set of problems is related to the FPs interference with the native oligomerization process. FPs themselves often tend to oligomerize (Dunsing *et al*., 2018). Fortunately, for GFP this can be easily solved by introduction of a single point mutation (A206K) abrogating the GFP dimerization (Zacharias *et al*., 2002). Besides undesirable inter-molecular interactions, FPs might also have an integral mesoscopic effect related to their accumulation (crowding) in/over a protein cluster (Stachowiak *et al*., 2012). Protein crowding creates entropic forces affecting formation and function of protein clusters (Espadas *et al*., 2019; Stachowiak *et al*., 2012). Though we did not directly assay for this effect, we assumed it minor for small Dyn1 oligomers (the main subject of this study) bearing few GFP molecules.

The second set of problems is related to the FP fluorescence properties. All FPs have a common structure, composed of a protein case and a chromophore group located at the center of the protein shell. The chromophore group needs to be post-translationally modified to be fully mature and acquire its intrinsic fluorescent property (Chudakov *et al*., 2010). The maturation rate greatly varies from FP to FP, being the rate-limiting step of most of them. In the case of mEGFP, it just takes 25 minutes to become fully mature (Cormack *et al*., 1996). The incomplete maturation of the chromophore group produces a FP unable to fluoresce, a condition known as dark state. This non-fluorescent state of a FP can be also produced by light-induced damage of the molecule (Vámosi *et al*., 2016). The presence of non-fluorescent GFPs in the protein assembly undermines correct evaluation of its molecular stoichiometry. Similar issue emerges due to fluorescence polarization. Though FPs are rarely completely rotationally constrained (McQuilken et al., 2015; Rocheleau *et al*., 2003) and, as in our case, weekly polarized LED light sources can be used, different spatial orientation of FPs in the protein cluster can lead to uneven excitation conditions and thus undermine the quantification of the FP-conjugated molecules. To test for these issues, we combined single molecule and ensemble calibrations, the latter based upon known ultrastructural parameters of helical Dyn1. We reasoned that thousands GFP molecules in a micron-long Dyn1-meGFP helix should reveal systematic error related to dark-state fluorophores of fluorescence polarization. Crucially, we found that the difference between the single molecule and ensemble calibrations was insignificant (Figure 4.2 D). Slightly lower values obtained by ensemble (helix-based) calibration might indeed reflect the presence of a small fraction of non-fluorescent GFPs and/or differences in the excitation efficiency in different parts of the helix. Yet, the diminished values might also reflect defects in the helical packaging,

as random as GFP-caused. The structural studies carried out on Dyn1 use a construct lacking the proline-rich domain (PRD) of the protein (Dyn1-ΔPRD) (Zhang and Hinshaw, 2001). This domain, responsible for the interaction between the protein and their binding partners, characterizes by the lack of structure (Antonny *et al*., 2016). The absence of the PRD allows obtaining a tightly packaged helix, widely used in cryo-EM studies (Kong *et al*., 2018; Zhang and Hinshaw, 2001). Then, long scaffolds, obtained with the full-length protein, would not present such dense packing. Therefore, we are likely overestimating the number of dynamins in the scaffolds and underestimating the fluorescence intensity per dynamin molecule obtained in the ensemble calibration.

Finally, we resorted to yet another, calibration-free technique called number and brightness (N&B) (Digman *et al*., 2008), which can be used to determine the oligomeric state of a labelled protein. One of the most attractive things of N&B is that it is based on a moment analysis to measure the number and brightness of labelled entities in each pixel of a stack of fluorescence images (Nolan *et al*., 2018). An entity is defined as the number of molecules, and its brightness as the number of photon detector counts detected while in the illumination volume. The ratio of the variance (σ^2) to the average intensity (<I>) in each pixel is used to calculate the average brightness of an entity. Variance increase, with equal average intensity, would be informative of an oligomeric state change. This technique can be used to discriminate the oligomeric state of different entities and/or to follow the oligomeric state change of an entity over time. This free-calibration technique has been previously used to determine the oligomeric state of Dyn2 in fusion pores during HIV-1 infection (Jones *et al*., 2017), and to determine the oligomeric state of Dyn2 within the plasma membrane of live cells (Ross *et al*., 2011). Crucially, using this technique in a cellular expression system we obtained similar distribution of Dyn1-meGFP clusters as in SLB-PNT system. Though additional experiments are needed for mechanistic comparison of the Dyn1 membrane adsorption to SLB and plasma membrane, the tendency of Dyn1 to form small clusters consisting of 2-4 tetramers is sticking and, as we show below, underlies the GTPase activity of the small subhelical Dyn1 oligomers.

Chapter 5:

The size and stoichiometry of the minimal Dyn1 fission machinery

There are many indications in the literature that the long regular Dyn1 helices, the foundation of the structural analyses of the GTPase activity of Dyn1 (Hinshaw and Schmid, 1995; Kong *et al*., 2018; Zhang and Hinshaw, 2001) are not required for fission and even inhibitory to the process (Antonny *et al*., 2016; Bashkirov *et al*., 2008a; Morlot *et al*., 2012; Pucadyil and Schmid, 2008). Moreover, other studies showed that the helical polymer fragments into smaller pieces (Kadosh *et al*., 2019). Before exploring the action of non-helical Dyn1 machineries, we studied the effect of GTP on large Dyn1 helices pre-assembled in the *apo* (nucleotide-free) state. To produce the helices, we prepared a SLB-NT template and incubated it for 10 minutes with a high concentration of the Dyn1-meGFP (0.5 µM). After washing away the excess of the protein, we imaged the sample and observed large Dyn1-meGFP helical scaffolds on the NT (Fig. 5.1A). Addition of GTP (1 mM) to the preassembled scaffolds caused the quick formation and expansion of multiple gaps in the scaffolds (Fig. 5.1A, kymograph). The gap formation was followed by the NT fission (Fig. 5.1A, red arrowhead).

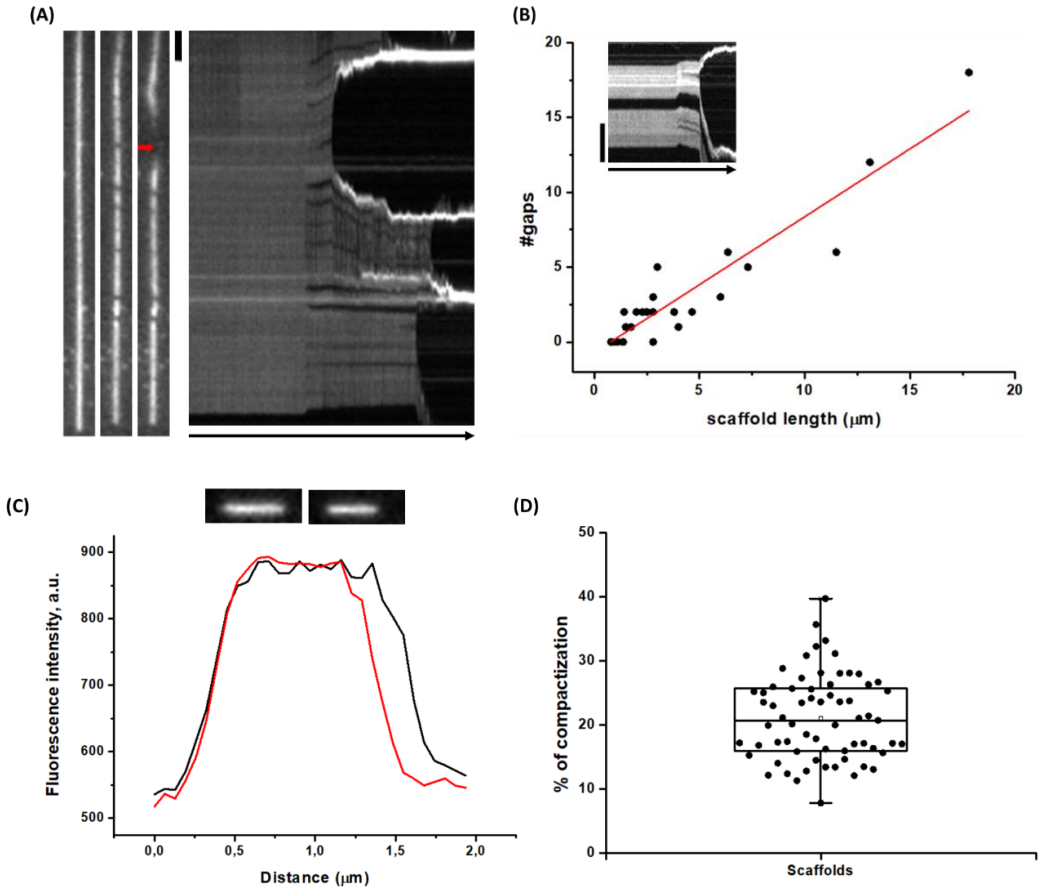

Figure 5.1. Effect of GTP addition to large Dyn1-meGFP scaffolds pre-assembled on lipid NT. (A) A time sequence of the fluorescence microscopy images (left) with the corresponding kymograph (right) showing

formation of gaps in a large Dyn1-meGFP scaffold followed by the NT fission. The GFP fluorescence is shown. Red arrowhead marks the fission event. Black arrow indicates time (10 s). Scale bar, 1 µm. (B) Dependence of the gap occurrence on the scaffold length. Insert shows kymograph illustrating appearance of the gap directly preceding membrane fission. Black arrow indicates time (10 s). Scale bar, 5 µm. (C) Fluorescence images of a Dyn1 scaffold before (left, black) and after (right, red) GTP addition, and their corresponding fluorescence intensity profiles illustrating scaffold compactization before fission. (D) Boxplot showing the % of scaffold compactization upon GTP addition.

The number of gaps increased linearly with the length of scaffolds (Fig. 5.1B), indicating that the gap formation is a regular process coupled to GTP-induce conformational rearrangements of the Dyn1 helix. This process was evident in the short individual scaffolds. Such scaffolds visibly shrank upon GTP addition (Fig. 5.1C). We measured their length before and after GTP addition and calculated the percentage of compactization (Fig. 5.1D). On average, the scaffolds shortened by 20%, closely matching the GTP-induced reduction of the axial distance between helical subunits from 13 to 10nm reported by cryo-EM (Kong *et al*., 2018; Zhang and Hinshaw, 2001). Hence, we interpreted the fragmentation of the large Dyn1-meGFP scaffolds as a reorganization of the helical polymer into shorter protein assemblies capable of mediate membrane fission. Importantly, in 25 out of 25 tubes the NT fission occurred at or near a gap, as can be seen from snapping of the two ends of the NT in opposite directions (Fig. 5.1B, inset). This evokes the earlier observation of the fission happening at or near the ends of long Dyn1 scaffolds (Morlot *et al*., 2012). Thus, by fragmentation of the long scaffolds the GTP hydrolysis promotes formation of the fission "hot spots", the scaffold edges.

It follows from the above that more severe fragmentation should benefit fission. Indeed, earlier electro-physiology-based assessment of short Dyn1 scaffold revealed that in the presence of GTP they tend to diminish their length to few helical turns (Shnyrova *et al*., 2013). Recent HS AFM study also revealed complete loss of helical order at nanoscale and the scaffold breakage into small, seemingly subhelical pieces (Kadosh *et al*., 2019). However, it remains unclear whether these small subhelical oligomers are fission-competent. To answer this question, we decided to change the experimental strategy. *In vitro* reconstructions of Dyn1-driven fission have been generally conducted under conditions optimal for the fission reaction, namely, at relatively high bulk concentration of the protein and with the high amount of charged lipid species in the target membrane (e.g., as those used in Fig. 5.1). Such settings accelerate helical self-assembly of Dyn1 even in the presence of GTP (Shnyrova *et al*., 2013). To obtain short Dyn1-meGFP structures, we reduced the amount of PIP_2 present in the lipid NTs, from 1 to 0.5 mol%,

and monitored protein, added at 50 nM final concentration, arrival to the tubes using fluorescence microscopy. Once we observed the Dyn1-meGFP spots on the NTs, we rapidly removed the protein from the bulk to suppress further self-assembly. As a result, we obtained small Dyn1-meGFP clusters, likely precursors of helical self-assembly, on the NT (Fig. 5.2A, left, Dyn1). Their scarce appearance contrasted to almost complete NT coverage by the protein obtained at high Dyn1-meGFP concentration in the bulk (Fig. 5.2A, right, Dyn1). The NT constriction by the large scaffolds was seen as the decrease of the lipid probe fluorescence proportional to the NT radius (Fig. 5.2A, right, lipid). Small oligomers did not produce visible constriction, indicating that their length was below optical resolution (Fig. 5.2A, left, lipid). To determine the size of these oligomers, we quantified the fluorescence intensity of individual oligomers using the algorithm described in Chapter 4 (Fig. 4.2C). The cumulative distribution of the intensities, normalized to the mean intensity of a single GFP (Fig. 4.2A), demonstrates that more that 50% of the clusters contained less than 30 Dyn1-meGFP molecules (Fig. 5.2B), the number associated with a single rung of a 1-start Dyn1 helix (Cocucci *et al.*, 2014; Zhang and Hinshaw, 2001). Hence, our add-wash approach indeed allowed trapping and investigating small sub-helical Dyn1 oligomers.

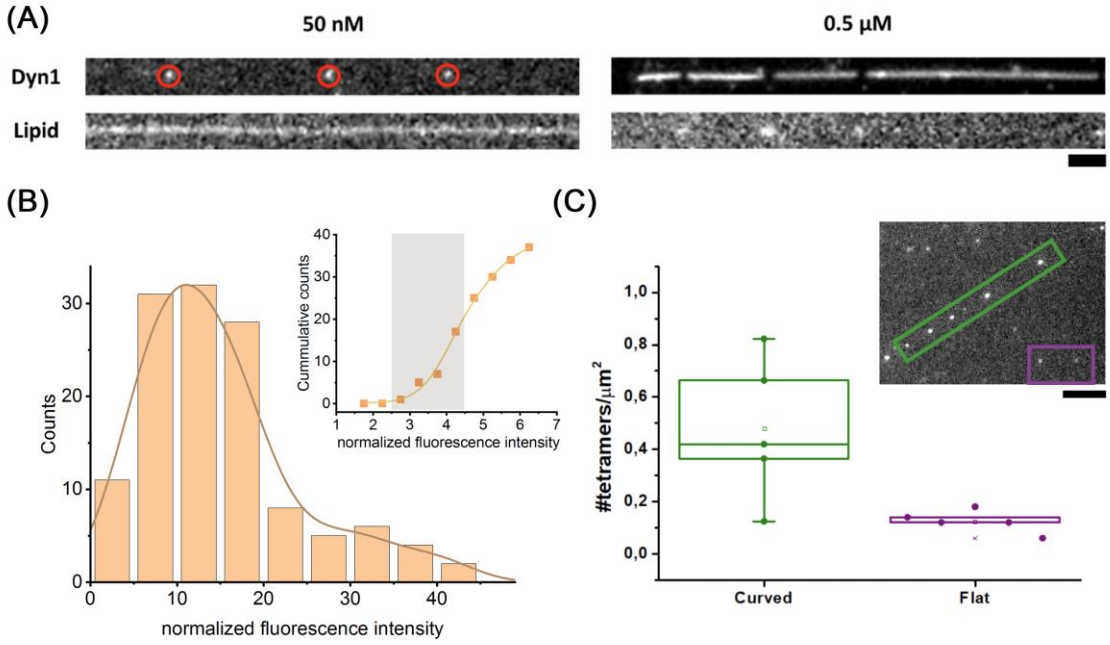

Figure 5.2. Trapping of small Dyn1-meGFP oligomers on the SLB-NT template. (A) Fluorescence microscopy images showing adsorption of Dyn1-meGFP to lipid NT at the indicated bulk concentrations of the protein. Red circles mark the small sub-helical Dyn1 oligomers formed on the lipid NTs. Scale bar, 2 µm. (B) Distribution of the fluorescence intensity of Dyn1-meGFP oligomers normalized to the mean

intensity of GFP (Fig. 4.2A). The inset shows the cumulative distribution of the intensities measured from the small oligomers (squares), the solid line showed $\sum_n(A_n normalCDF(n, \sigma_n))$ fit (n=3-6, see Fig. 4.2C). The grey rectangle marks trimer (A_3=0.05±0.04) and tetramer (A_4=0.49±0.08) fractions. (C) Surface density of the Dyn1-meGFP tetramers (defined as the oligomers with the normalized intensity less than 6) bound to the NT (small clusters in the green ROI in the inset) and to the flat SLB (smaller cluster in the magenta ROI). The NT area was calculated using the ROI length and the average NT radius determined as described in Fig. 3.5C. The inset shown a representative part of SLB-NT template with a single NT crossing over (the chain of Dyn1-meGFP oligomers bound to the NT in seen in the green ROI). Scale bar, 5 μm.

The smallest detected oligomers were tetramers (Fig. 5.2B, inset), the dominant oligomeric state of the protein in the bulk (Sever *et al*., 2006). We next determined whether the tetramers bind preferably to the NT membrane. Comparison of the tetramer surface density (per μm^2) on the NT and flat SLB revealed that the tetramers bound on average 4 times more efficiently to the NT (Fig. 5.2C). Hence the Dyn1-meGFP tetramers sense membrane curvature and tend to bind to the membranes of higher curvature.

Next, we assessed the lateral mobility of Dyn1-meGFP oligomers on the NT surface. The small oligomers bound to the NTs were visibly mobile, while the large ones remained almost static (Fig. 5.3A). We calculated the diffusion coefficients for the small (normalized fluorescence intensity smaller than 16) oligomers following the protocol explained in Fig. 3.4, modified for the 1D diffusion. The lateral mobility of such subhelical oligomers increased upon addition of 1mM GTP to the bulk (Fig. 5.3B), indicating that their membrane affinity depends on the nucleotide binding and/or hydrolysis.

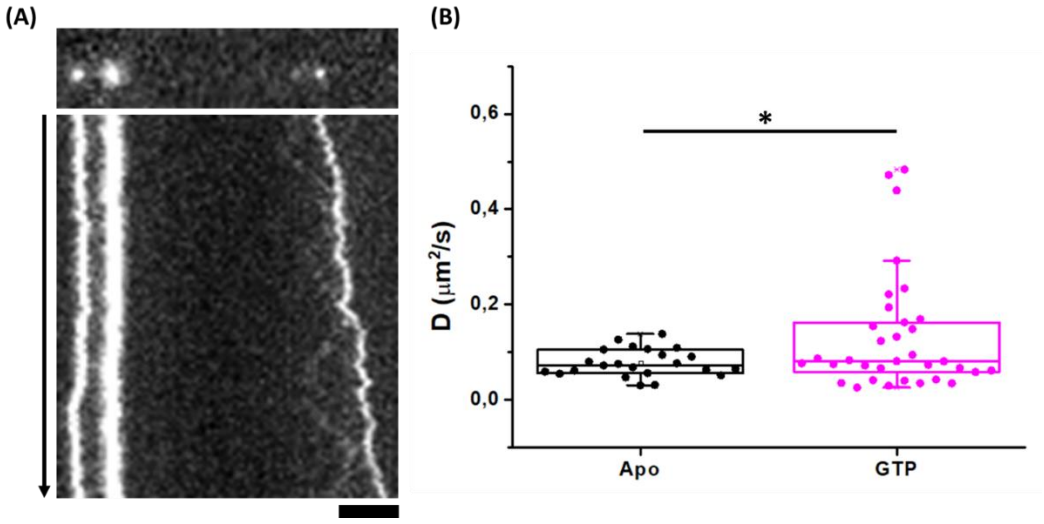

Figure 5.3. Mobility of small Dyn1-meGFP oligomers on the NT surface. (A) The upper panel corresponds to the fluorescence image of oligomers stably bound to a lipid NT and the lower panel corresponds to the kymograph, which illustrates the lateral mobility of the oligomers. Black arrow indicates time (10 s). Scale bar, 2 µm. (B) Boxplot showing the lateral diffusion coefficient of Dyn1-meGFP oligomers bound to lipid nanotubes. Statistical significance was calculated according to Two sample t test (n=23, n=34, respectively).

This "activation" of the small oligomers by GTP was followed by the NT fission. The moment of fission was seen as a rapid movement of the oligomers in two opposite directions (Fig. 5.4A). Fission is unlikely to happen in dynamin-free parts of the tube as ~1/20nm^{-1} curvature of non-constricted NTs (see Fig. 5.2A, 3.5C (fast)) is too low for spontaneous fission. Hence, we associated the fission with the local membrane constriction by Dyn1-meGFP oligomers. To identify the fission making oligomers, we analysed the kymograph plots. We looked for the neighbour clusters moving in opposite directions. In 27 cases we could clearly identified such cluster pairs (Fig. 5.4B, arrows). Though we could not discriminate which one of the two clusters produced fission, the size distribution for the bigger of the two (Fig. 5.4C) reveals that in 22 cases the fission was mediated by oligomers smaller than a full rung of 1-start Dyn1 helix.

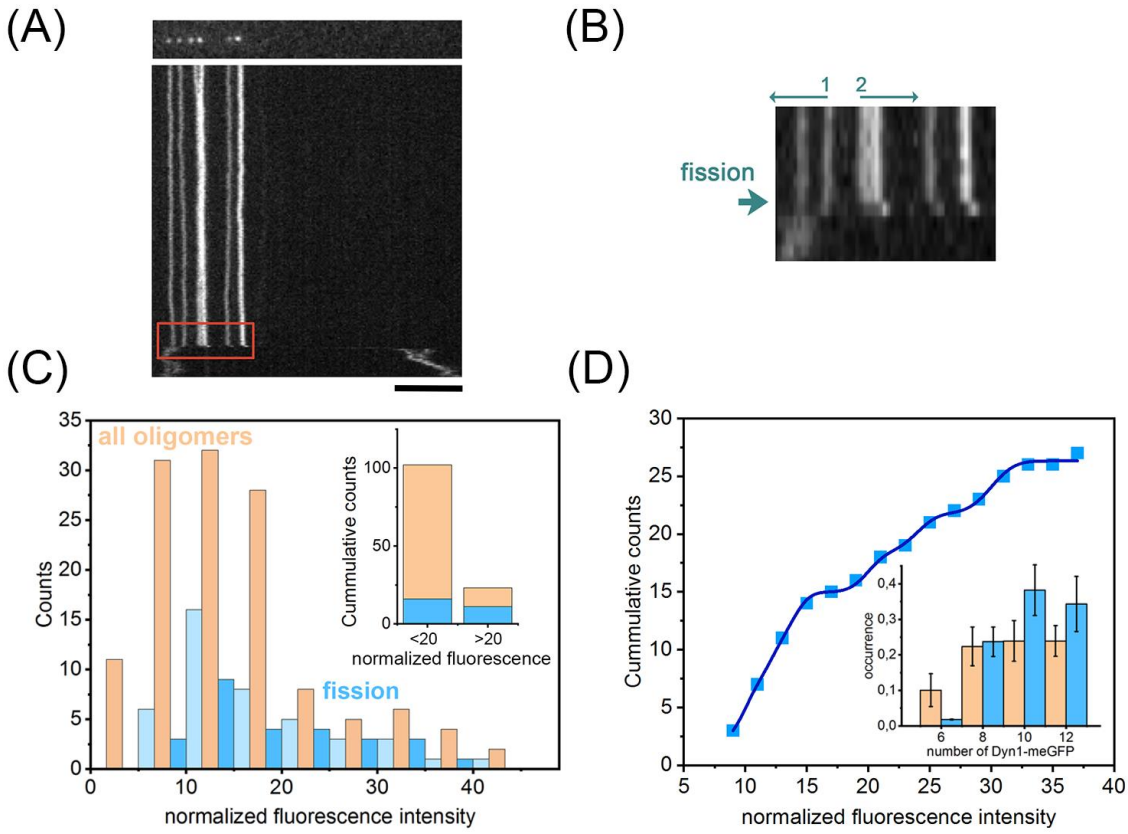

Figure 5.4. Small Dyn1-meGFP oligomers mediate membrane fission. (A) The fluorescence microscopy image (GFP fluorescence) of the oligomers stably bound to a lipid NT (upper panel) and the kymograph (100ms/line) illustrating the NT fission seen as the NT snapping in different directions (red rectangular) (B) A blow-up of the ROI marked by the red rectangular in (A), oligomers 1 and 2 move in opposite directions upon fission. (C) Histogram illustrating the size distribution of the pairs of Dyn1-meGFP oligomers associated with the membrane fission (light blue) and of the larger-in-the-pair oligomers (blue), compared with the size distribution of all NT-bound oligomers (apricot). The inset shows the total amount of small (n<20) and large (n>20) oligomers in the groups indicated by colour coding. (D) The cumulative distribution of the normalized fluorescence intensity for the subhelical (n<30) fission-producing (blue group in (C)) oligomers (squares). The distribution was fitted by a linear combination of the intensity distributions for the oligomers containing even number of molecules (blue line). The inset shows the relative occurrence of the small species in all NT-bound (apricot) and fission-associated (blue) oligomers obtained from the fit (see Fig. 4.2).

Hence, the GTP-driven "activation" of the subhelical oligomers not only augments their lateral mobility but also converts them into stand-alone fission machineries. The large (>20 molecules) oligomers produced fission much more effectively than their smaller counterparts, as can be seen from the ratio of the fission events to the total number of oligomers (Fig. 5.4C, inset). This

difference in the efficiency might account for the diminished participation of the subhelical Dyn1 oligomers in the membrane scission in the cell, with the mean size of the fission-producing oligomers there being estimated as ~30 Dyn1 molecules (Cocucci *et al*., 2014).

The broadness of the fluorescence intensity distribution (Fig. 5.4C, blue) suggests no preferred stoichiometry of the Dyn1 fission machinery. The stoichiometric resolution of our measurements, estimated as $n_{max}=(f_{GFP}/\sigma_{GFP})^2 \sim 16$ (Schmidt *et al*., 1996), shall allow us discriminating oligomeric species smaller than 16. Hence, we attempted fitting the distribution using $\sum_n(A_n normalCDF(n,\sigma_n))$ (see Fig. 4.2C above) with the combination of even-numbered oligomers as the dimer is an elementary building block of the Dyn1 polymer (see Chapter 1, Figs 1.2 and 1.3). The fit (r^2=0.99, Fig. 5.4D, blue curve) revealed that the smallest fission machineries contained 8, 10 and 12 dynamin molecules (Fig. 5.4D, inset, blue bars). As the number of the fission events associated with the small oligomers was small, we applied the same fitting function to the fluorescence intensity distribution measured for all NT-bound oligomers (Fig. 5.4C, apricot). We found that the main peak of the distribution is comprised by octa-, deca- and dodecamers, equally present (Fig. 5.4D, apricot bars). Apparently, the smallest fission machineries were recruited from this oligomer pool. Thus, we conclude that the minimal fission machinery consists of 2-3 Dyn1 tetramers.

Activation of the membrane fission activity as well as lateral mobility of small Dyn1-meGFP oligomers by GTP implies the nucleotide hydrolysis and thus GG dimerization. The dimerization cannot occur within a subhelical oligomer, the one representing a part of the 1-start Dyn1 helix, as all of its G domains are facing outwards (Fig. 1.3). A full helical turn is required to setup the G domains from the adjacent helical rungs for the dimerization (see Chapter 1, Fig 1.3). Apparently, the GG dimerization would require lateral interactions between subhelical oligomers. We next explored whether such interactions are feasible and how they could occur.

We employed the SLB-PNT template as the PNT supported lipid bilayers have highly curved half-cylinder shape, an attractive substrate for small curvature-sensing molecular entities. Indeed, upon addition of Dyn1-me GFP to the bulk (0.5 µM), followed by 10 minutes incubation and removal of the unbound protein, we found PNT surface covered by the protein (Fig. 5.5A). The bound oligomers could not self-assemble into a helix winding around the PNT as the PNTs were tightly bound to the planar substrate (see Chapter 3). Hence, the PNTs were likely covered by subhelical arc-like Dyn1-meGFP oligomers (Fig. 5.5A, cartoon). When we compared the fluorescence intensity per area on PNTs vs the flat parts of the SLB, we observed that, as on the

SLB-NT template (Fig. 5.2C), the subhelical oligomers sensed the membrane curvature and accumulated on highly curved parts of the SLB-PNT template (Fig. 5.5B) (Liu *et al*., 2011b).

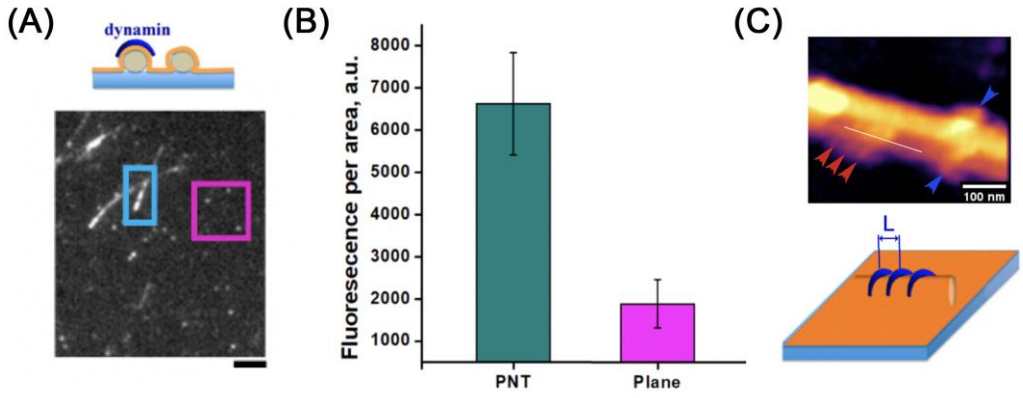

Figure 5.5 Subhelical Dyn1 oligomers lateral interaction. (A) Schematic representation of the template showing Dyn1 clusters on a lipid bilayer covering a PNT and a fluorescence microscopy picture showing Dyn1 oligomers over a PNT (blue), and over the flat regions of the template (magenta). Scale bar, 2 µm. (B) The column bars show fluorescence (meGFP) intensity density calculated from the ROIs drawn over the PNT-SLB template (cyan) and the flat (magenta) lipid bilayer. (C) HS-AFM image showing small Dyn1 oligomers over the SLB-PNT template. Blue and red arrows mark the position of individual and aligned Dyn1 oligomers, respectively. The cartoon illustrates arc-like Dyn1 oligomers separated by a length (L).

To resolve the fine structure of the Dyn1-meGFP oligomers on the PNTs we applied HS AFM imaging in collaboration with Dr. Aleksandr Noy´s group (LLNL, Livermore, USA). The experiments, carried out in their laboratory, confirmed that Dyn1-meGFP formed small arc-like oligomers on the PNT surface (Fig. 5.5C). The oligomers were oriented at an angle to the PNT surface as in the helical arrangement (Fig. 5.5C, arrows). We ascribed this orientation to the geometry of the attachment line between the oligomers and the membrane, similar in subhelical oligomers and in the full Dyn1 helix. The oligomers often form small groups indicating weak lateral interaction (Fig. 5.5C, red arrows). Crucially, the axial distance between the adjacent oligomers, measured between the peaks of the height profile (Fig. 5.5C, cartoon), decreased from 21.8 ± 7.7 nm to 13.6 ± 3.7 nm upon GTP addition, indicating GTP-driven attraction between the oligomers. Same attractive forces are likely responsible for the GTP-driven compactization of short Dyn1-meGFP scaffolds seen by fluorescence microscopy (Fig. 5.1C, D). The 13nm distance between the PNT-bound oligomers matches the pitch of Dyn1 helix (Colom *et al*., 2017b; Zhang and Hinshaw, 2001), so that the G domains of the closely apposed oligomers

are setup for GTP-dependent dimerization. Hence, we concluded that the GG dimerization can occur via lateral interaction between membrane-bound subhelical oligomers, without full-scale helical polymerization.

On the PNT surface the dimerization is facilitated by the oligomer crowding. But how does it occur in the sparse subhelical oligomers as those shown in Fig. 5.4A producing the NT fission? We identified two possible pathways of the oligomer interaction leading to GG dimerization. The first is via collision between small and highly mobile Dyn1-meGFP oligomers in the presence of GTP. In some cases (~10%) such collision could be traced to the NT scission (Fig. 5.6A). The second is via lateral interaction between the oligomers in the *apo* state, driven by weak GG dimerization (Kong *et al*., 2018) and membrane-mediated attractive interactions (Jarin *et al*., 2021; Van Der Wel *et al*., 2016; Yolcu *et al*., 2014). This weak lateral attraction is corroborated by clusterization of the arc-like oligomers on the PNT surface prior to GTP addition (Fig. 5.5C). It follows that a small Dyn1-meGFP cluster detected by fluorescence microscopy might represent either a single oligomer, a part of 1-start Dyn1 helix, or a cluster of smaller oligomers. The latter but not the former arrangement can be "activated" by GTP. The comparison of the two arrangements of 12 Dyn1-meGFP molecules are shown in Fig. 5.6B, C. The single oligomer, dodecamer, is a short arc representing about 1/3 of the 1-start helical rung (Fig. 5.6B). It cannot form GG dimers by itself and hence cannot effectively hydrolyze GTP. Alternatively, 3 tetramers interacting via GG links form a much longer arc which engulf the NT and is GTP active (Fig. 5.6C). We conclude that minimal Dyn1 fission machinery is constructed from short arc-like oligomers linked together via GG dimers. Multiple GG dimers form the motor core of the machine while the curved oligomers operate as membrane-constricting arms spreading out from the core.

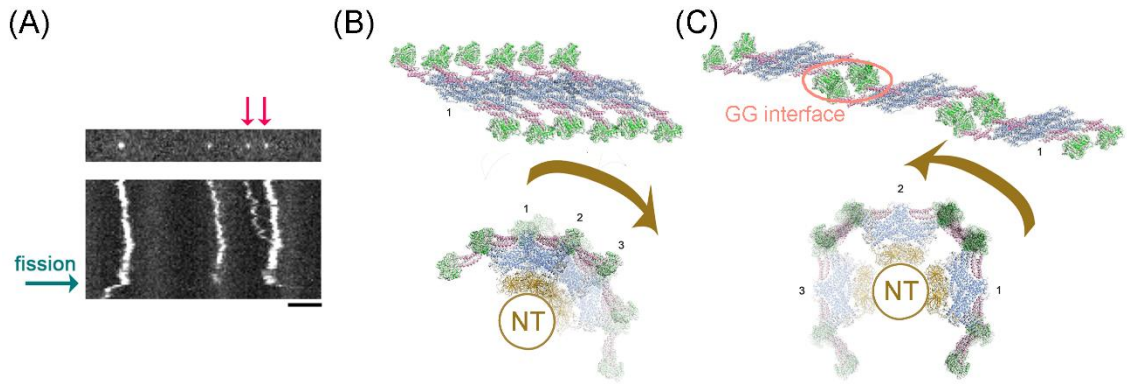

Figure 5.6 Two modes of interaction between subhelical oligomers of Dyn1. (A) The fluorescence microscopy image (upper panel) shows small Dyn1-meGFP oligomers bound to a horizontally oriented NT

(GFP fluorescence is shown). The kymograph (lower panel) shows the merger of two oligomers (marked by red arrows) followed by the NT scission. 1mM GTP is present in the bulk, the scale bar is 2μm. (B, C) The cartoons illustrate a possible spatial arrangement of the dynamin oligomers upon merger. A straightened oligomer assembled of three tetramers via stalk (B) and GG (C) is shown in the upper panel. The frontal view of the Dyn1 oligomer, adopted from cryo-EM reconstruction ((Kong *et al*., 2018), is used), bound to a NT (brown circle) is shown in the lower panel. The stalk-mediated interaction between the tetramers would result in the short dodecamer shown in (B). The GG mediated interaction would result in the long dodecamer seen in (C).

The molecular stoichiometry of the machinery is not fixed. Rather, the GG driven self-assembly is a dynamic process enabling self-optimization and adaptation of the machinery size to the lipid template. We will explore this adaptation in more details in the following chapter.

Discussion

The space between the parent membrane and the nascent vesicle, defined by the length of the membrane neck (Kosaka and Ikeda, 1983), is just about 20 nm long. Therefore, the fission reaction must be governed by a very small machinery. Indeed, a theoretical analysis, based on *in vitro* experiments, defined two-rung dynamin scaffold, about 20nm long, as the minimal unit required to mediate membrane fission (Shnyrova *et al*., 2013). On the other hand, quantitative fluorescence microscopy experiments performed in cells determined that a single helical rung is sufficient for coated vesicle release (Cocucci *et al*., 2014; Grassart *et al*., 2014a). Even shorter, sub-helical Dyn1 units operate at early stages of endocytosis as regulators of the clathrin-coated pit maturation (Loerke *et al*., 2009; Macia *et al*., 2006; Narayanan *et al*., 2005). Supporting all of the above observations, we reveal here that the Dyn1 machinery, that is, the Dyn1 oligomer capable of GTP-dependent membrane action, has no predetermined size. The key process for the machinery emergence is GG dimerization, as established earlier (Antonny *et al*., 2016; Chappie *et al*., 2010). However, the previous studies linked GG dimerization to full scale helical polymerization, formation of at least single helical turn enabling trans-rung interaction between the G domains. Here we found that GG dimerization is possible between the small subhelical oligomers, precursors of the helical polymerization. The dimerization pieces such oligomers together into a mechano-active unit capable of producing membrane scission.

The leading role of GG dimerization in the self-assembly of Dyn1 fission machinery has been long appreciated. More than two decades ago it was found that Dyn1 in solution, in absence of any lipid membrane, could form rings and spirals when incubated with GDP and beryllium or aluminium fluoride (BeF_3^- or AlF_4^-) (Carr and Hinshaw, 1997), which arrest the GTP hydrolysis cycle in the transition state (TS, (Bigay *et al*., 1985). The authors concluded that TS Dyn1 is the protein configuration seen as electron-dense collar on the necks of the clathrin-coated pits (Takei *et al*., 1995). The mechanistic interpretation of the TS self-assembly was done by Chappie *et al*. about a decade later: they found Dyn1 G domains dimerized strongly in the TS (Chappie *et al*., 2010). They predicted, and further confirmed through a model based on cryo-EM and crystallographic data (Chappie *et al*., 2011), that the G-G domain dimerization just occurs between dynamin tetramers and not between G domains within the tetramer, leading to the formation of a GTP/TS state-dependent octamer.

However, they also showed that the GG dimerization is strong only in the TS. During the rest of the GTPase cycle the GG bond is weak or non-existent, furthermore, GTP promotes disassembly of large Dyn1 helices (Antonny *et al*., 2016; Carr and Hinshaw, 1997). Hence, the Dyn1 helix has been commonly considered as a rigid frame required to hold the G domains in place for

continuous GTP hydrolysis. How can the GG dimerization result in formation of a stable contact between the subhelical oligomers free to move out?

We believe that the necessary assistance comes from the membrane template. As small Dyn1 oligomers, even tetramers, have intrinsic curvature (Fig. 5.2C), they tend to accumulate on positively curved membrane parts. Furthermore, the arc-like oligomers have a preferable orientation on the cylindrical surface greatly facilitating their stacking and thus formation of the GG contacts (Fig. 5.5C). Hence, even if the strength of GG interaction varies during the GTPase cycle the oligomers are unlikely to split apart immediately. Furthermore, in large Dyn1 helices the hydrolysis cycles are not synchronized and at each given moment of time the hydrolysis happens only in a few GG dimers randomly scattered over the helix (Galli *et al*., 2017). Hence, if an intermolecular bonding interface is comprised of many GG dimers, it might remain stable while some of the dimers hydrolyze GTP. The interface could be further stabilized by weak GG dimerization seen in the apo state (Kong *et al*., 2018). Lastly, we note that the GG interface does not need to be long living as its formation is rapidly followed by membrane scission (e.g., see Fig. 5.6A). The disassembly of GG-mediated machinery and detachment of the Dyn1 from the membrane (studied in detail in the next chapter) upon fission would be necessary for the prompt recycling of the protein in the cell.

We next ask whether small subhelical Dyn1 oligomers could generate enough force to drive scission. The energy barrier for the fission of a pre-constricted vesicle neck or NT was estimated as 20-40k_BT (Kozlovsky and Kozlov, 2003; Shnyrova *et al*., 2013), comparable with the energy generated by hydrolysis of 2-3 GTP molecules. Such energies can in principle be generated in the subhelical oligomers having 2 and more active GG links. However, the extent of the pre-constriction and the geometry of the small oligomers would critically influence the efficiency of the subhelical fission machinery (Shnyrova *et al*., 2013). In our system the fission was assisted by relatively high (1-3*10^{-4}N/m) tension pre-constricting the NTs (see Fig. 3.5C). Even there the small oligomers were much less effective than their larger counterparts (see Fig. 5.4C, inset). We note that, as mentioned above, the hydrolysis cycles are unsynchronized in Dyn1 helix (Galli *et al*., 2017), hence the fission is likely driven by a few hydrolysis events even in the large Dyn1 machineries. Their size then is important not for generation of the hydrolysis-driven powerstroke but for the pre-constriction relying upon “passive”, GTP-independent curvature activity of Dyn1. In this respect, we found that Dyn1 tetramers already possess intrinsic curvature activity, seen in their preferential binding to highly curved NTs (Fig. 5.2C). This intrinsic curvature activity can account for the local pre-constriction required for the membrane scission by small Dyn1 oligomers.

If the fission machinery is easily made from small arc-like Dyn1 oligomers via GG dimerization what is the role of the helical self-assembly of Dyn1? Formation of Dyn1 helices is a robust process mediated by evolutionary conserved interactions and, as such, it cannot be simply dismissed. And it is not in our model. The machinery formed via GG dimerization can be considered a part of Dyn1 helix, but not the 1-start helix. Recent structural analyses demonstrated that 1-start helix is incompatible with GTP hydrolysis (Kong *et al*., 2018). In the GTP-bound super-constricted state directly preceding membrane scission, Dyn1 forms 2-start helix with two helical strands tightly bound via GG links (Kong *et al*., 2018; Sundborger *et al*., 2014). Two subhelical oligomers linked via GG interface on a curved membrane can be considered as a part of 2-start helix (see Fig. 5.5C). Hence, the energy transduction mechanisms underlying the mechano-chemical activity of Dyn1 and established using the 1- and 2-start helical models shall be straightforwardly applied to our short Dyn1 machineries. In the next chapter we will test the major prediction of these mechanisms on the subhelical Dyn1 machinery.

Chapter 6:

Characterization of the GTP effects on the subhelical Dyn1 oligomers

In the previous chapter we established that small, subhelical Dyn1 oligomers could use the energy of GTP hydrolysis generated by the GG interface for membrane scission. In this chapter we will test whether the energy transduction mechanisms, established for helical Dyn1, operate in the subhelical machinery. It is generally accepted that in Dyn1 polymer the GTP cycle is coupled to a set of conformational rearrangements on the polymer architecture, which affects the interaction between the individual polymer subunits and the underlying lipid membrane (Mattila *et al*., 2015; Mehrotra *et al*., 2014; Ramachandran and Schmid, 2008). Therefore, we explored how these small Dyn1 units interact with membranes and how this interaction changes along the GTP hydrolysis cycle. We showed earlier that Dyn1-meGFP binds to SLB and oligomerizes on the template, with I690K mutant inhibiting formation of large oligomers (Fig. 4.2B). Here we explored the diffusional mobility of small (<16 molecules) oligomers. We postulated that these oligomers interact with SLB via their PH domains. Their mobility then should depend on the membrane perturbations produced by the PH domains, as reported for various peripheral membrane proteins (Knight *et al*., 2010; Yamamoto *et al*., 2017; Ziemba and Falke, 2013; Ziemba *et al*., 2012).

It has been demonstrated that the PH domain wedges into the hydrophobic core of the lipid bilayer and the insertion depth varies along the GTP cycle (Mattila *et al*., 2015; Mehrotra *et al*., 2014; Ramachandran and Schmid, 2008; Shnyrova *et al*., 2013). The wedging, and associated membrane deformations, are expected to hinder the diffusional mobility of the oligomers (Ziemba and Falke, 2013). We, therefore, hypothesized that if small Dyn1 oligomers are mechano-chemically active, the nucleotide binding and GTP hydrolysis should affect their diffusional behaviour on the SLBs. To test this hypothesis, we used the spot tracking plugin from Icy 2.0 to get the trajectories from these mobile oligomers and calculate their effective diffusion constants using the two-component diffusion model (as described in Chapter 3, see Fig. 3.4). The GTP addition resulted in dramatic increase of the lateral mobility of the oligomers as compared to the mobility in the *apo* state (Fig. 6.1A). Conversely, addition of GDP AlF_4^- blocking the hydrolysis cycle in the transition state (TS) slowed the oligomers down (Fig. 6.1A).

The two-component model generally returned two diffusion coefficients (Fig. 6.1C, D), indicating the combination of fast and slow diffusion processes. The latter process likely reports oligomer stalling by defects in the SLB templates, such as curved edges of the holes (Fig. 3.2), natural attractors for the membrane-wedging PH domains. Accordingly, the smaller diffusion coefficient decreased sharply in the TS, indicating much increased diffusion stalling. The slowed diffusion and the stalling effect correspond well to the increased membrane insertion of the PH domains in the TS reported earlier as one of the characteristic feature of the GTPase activity of Dyn1

(Antonny *et al*., 2016; Mattila *et al*., 2015). GTP, in turn, shifted the distribution of both diffusion coefficients to the right, indicating that conformational dynamics of the oligomers fueled by the hydrolysis teared the oligomers from the membrane, its flat parts or defects (Fig. 6.1B, blue arrow).

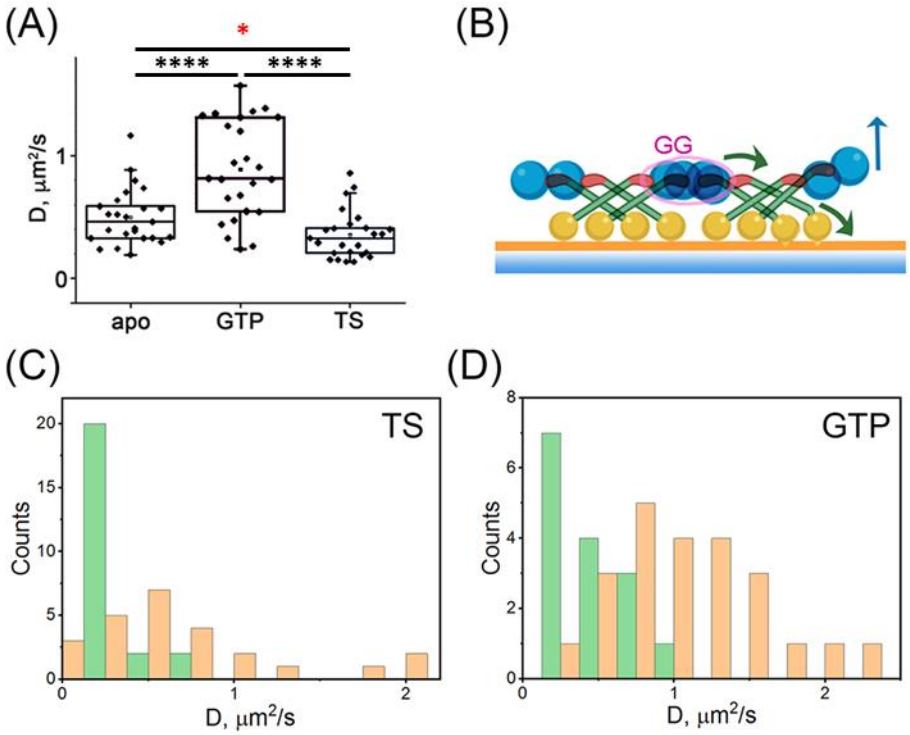

Figure 6.1 Effect of nucleotides on the diffusional mobility of Dyn1 oligomers on the SLB. (A) Box plot of the weighted diffusion coefficient D = (D_1 * ε_1) + (D_2 * ε_2) (see Fig. 3.4 for details) measured for the subhelical (8-18 molecules) Dyn1-meGFP oligomers in the apo state (apo), upon addition of GTP (GTP) and GDP AlF_4^- (TS). Statistical significance was calculated according to One-way ANOVA (n=25) (red asterisk means no significantly different applying ANOVA, but significantly different applying t-test). (B) The cartoon showing 2 Dyn1 tetramers on the SLB surface interacting via GG dimerization. The green arrows show that the GTP hydrolysis by the GG interface is translated to the changes of the membrane insertion by the PH domain. The blue arrow indicates the detachment force produced by the hydrolysis. (C, D). Histograms showing distribution of D_1 (the smaller coefficient in the pair measured for an oligomer, green) and D_2 (the larger coefficient, apricot) measured in TS (C) and in the presence of 1mM GTP (D).

To further explore this effect of GTP, we tested whether the GTP addition induced detachment of the oligomers from the SLB surface (Ramachandran and Schmid, 2008). For that, we compared the density of the Dyn1-meGFP oligomers on the SLB surface before and 5 min after

GTP (1 mM) addition (Fig. 6.2A). We then calculated the ratio between the two densities characterizing the average probability of the oligomer survival on the SLB surface upon the GTP addition. We normalized it to the probability measured in the apo state to account for GTP-independent changes, such as bleaching. As a control we used 1:1 mixture of the Dyn1-meGFP and I690K mutant of Dyn1, established blocker of the GTPase activity of the protein (Song *et al.*, 2004). The survival analysis revealed that about 30% of the Dyn1-meGFP oligomers detached from SLB (Fig. 6.2B). No significant decrease of the survival probability was seen in the presence of I690K, in agreement with the detachment driven by GTP hydrolysis. Crucially, analysis of size distribution of the Dyn1-meGFP oligomers revealed that the detachment was mostly in the subhelical oligomer pool (8-12 Dyn1-meGFP molecules, Fig. 6.2C), similar to oligomers trapped on NT (see Fig. 5.4C). Hence, GTP-driven activation of these oligomers, seen in the increased diffusional mobility, was indeed linked to decreased membrane affinity leading to probabilistic detachment of the oligomers from the SLB surface.

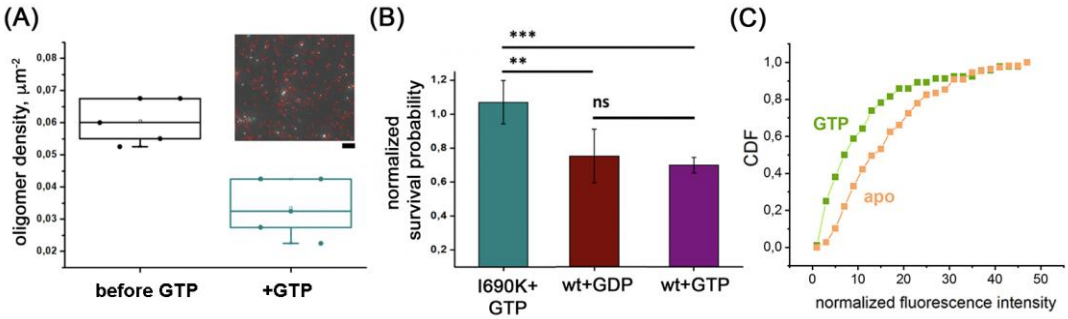

Figure 6.2 GTP-driven detachment of Dyn1-meGFP oligomers from SLB. (A) The boxplot showing the oligomer surface density (number of oligomers per surface area) calculated for randomly selected ROIs before and 5min after GTP addition. The inset shows a fluorescence microscopy image (GFP) individual Dyn1-meGFP clusters (red circles) bound to a SLB template. Scale bar, 5 µm. (B) Column bars showing survival probability (calculated as the ratio of the densities measured in (A)), normalized to the survival probability measured in *apo* state. Statistical significance was calculated according to One-way ANOVA (n=5). (C) Cumulative distribution of the fluorescence intensity of the Dyn1-meGFP oligomers (normalized to the mean fluorescence of a single GFP, Fig. 4.2A) before (apricot) and after (green) the GTP addition.

The decrease membrane affinity is likely related to the conformational rearrangements of the subhelical oligomers driven by GTP hydrolysis. On a soft membrane template, such as NT, the rearrangements produce the constriction force leading to the NT scission (Fig. 5.4). On a rigid SLB the force instead would turn back to the oligomer causing its detachment from the

membrane. As in the TS the membrane engagement is maximal, the conformation(s) pushing the oligomers away from the SLB (Fig. 6.1B, blue arrow) occur post-TS, close to the GDP-bound state (Mattila *et al*., 2015). Indeed, addition of GDP (10mM, to compensate for small affinity of Dyn1 G domain to GDP) caused the oligomer detachment from the SLB comparable to that driven by GTP (Fig. 6.2B). Hence, as in the helical Dyn1, GDP addition recreates the final part of the working cycle of the Dyn1 machinery, its disassembly and recycling to the bulk. Summarizing all of the above, we concluded that small sub-helical Dyn1-meGFP oligomers could deliver the energy of GTP hydrolysis to the membrane using the conventional set of conformational rearrangements described for helical Dyn1.

Discussion

Dyn1 interacts with membranes via the PH domain (Fig. 1.2, (Raimondi *et al*., 2011; Schmid and Frolov, 2011). The domain has specific pockets recognizing highly charged lipid species, particularly, PI(4,5)P_2 phosphatidylinositol (Antonny *et al*., 2016; Ferguson *et al*., 1994; Lemmon and Ferguson, 2000) as well as parts, such as variable loop 1 (VL1), wedging into hydrophobic core of the lipid bilayer (Ramachandran and Schmid, 2008). The membrane insertion of the PH domain of Dyn1 is coupled to its GTPase activity: the insertion of VL1 depends on the nucleotide-bound state of the G domain (Mattila *et al*., 2015). Furthermore, the PH domain present two alternate orientations, characterised by the insertion or the retraction of the VL1 into the membrane bilayer (Mehrotra *et al*., 2014). These observations have been supported by the cryo-EM maps of ΔPRD Dyn1 polymers at different NTP-bound states (Kong *et al*., 2018), which showed a deeper insertion of the PH domain at advanced stages of the hydrolysis cycle. Therefore, it has become established that Dyn1 helix uses the energy of GTP hydrolysis to wedge the PH deeper into the membrane core, thus promoting the membrane destabilization and scission (Antonny *et al*., 2016).

Here we show that similar energy transduction mechanism operates in subhelical Dyn1 oligomers. We used the membrane mobility of the oligomers as an indicator of the membrane insertion of the PH domains in the oligomers. A study carried out with multimers of the GRP1 PH domain revealed that the lateral diffusion of those constructs on lipid bilayers was inversely proportional to the number of bound lipids (Knight *et al*., 2010; Yamamoto *et al*., 2017; Ziemba *et al*., 2012). The presence of different negatively charged lipid species promotes a stronger interaction with the membrane, slowing down the diffusivity of the particles (Knight and Falke, 2009). Protein insertion into the hydrocarbon core of the membrane further decreases its mobility on a membrane surface, the effect being proportional to the number on membrane-inserting domains (Ziemba and Falke, 2013). Therefore, the diffusivity of Dyn1 oligomers on SLB should depend on the number of PH domains actively engaged with the lipid template. We found that in the presence of GDP AlF_4^- the diffusional mobility of the oligomers was reduced as compared with the mobility measured in the absence of nucleotides (Fig. 6.1A, C). Conversely, addition of GTP increased the mobility and triggered detachment of oligomers from the SLB (Fig. 6.1A, 6.2A, B). Similar detachment was induced by addition of GDP known to interfere with helical self-assembly of Dyn1 on membrane templates (Bashkirov *et al*., 2008a; Stowell *et al*., 1999). Overall, the effects of nucleotides and TS mimic addition on subhelical Dyn1-meGFP oligomers bound to SLB qualitatively resembled those reported for the helical Dyn1. Furthermore, similar sized oligomers bound to the NT produced membrane scission upon GTP

addition (Fig. 5.4). We concluded that sub-helical Dyn1-meGFP oligomers could deliver the energy of GTP hydrolysis to the membrane using the conventional set of conformational rearrangements described for helical Dyn1.

The increased mobility of the subhelical Dyn1-meGFP oligomers bound to SLB in the presence of GTP closely resembles the GTP-driven "activation" of the oligomers bound to the NT template (Fig. 5.3). In both cases the effective diffusion constant increased substantially upon GTP addition, though the NT-bound oligomers move slower than their SLB-bound counterparts (Fig. 6.1A, 5.3B). We ascribe the difference in mobility to the NT deformations produced by the oligomers. Another common feature of the GTP-driven activation of these oligomers seen on both SLB and NT was that the oligomers remained bound to the membrane and did not break apart while hydrolysing GTP. Hence GTP-dependent GG dimerization indeed creates a stable intermolecular interface and, simultaneously, mechano-active core of the Dyn1 molecular machinery. The minimal subhelical machinery can operate on flat and curved membrane templates and use GTP hydrolysis to control its membrane affinity and mobility. In the cellular context, the GTPase activity of small Dyn1 oligomers can account for their active exchange with the cytoplasmic pool as well as for their active, curvature-directed migration towards the neck of the endocytic vesicle.

Chapter 7:

Conclusions

1. Combination of supported lipid bilayer (SLB) with lipid membrane nanotubes (NT) and peptoid nanotubes (PNT) creates robust and tunable SLB-NT and SLB-PNT templates suitable for single molecule analyses of membrane activity by individual proteins and protein complexes.

2. Attachment of meGFP to the C terminal of Dynamin1 does not significantly interfere with its biochemical and membrane remodeling activities *in vitro*, enabling stoichiometric analysis of functional Dyn1-meGFP oligomers.

3. The mechano-chemical activity of Dynamin1 is not limited to helical structures, small subhelical oligomers of Dynamin1 can perform mechanical work upon GTP addition.

4. Non-helical Dyn1 assemblies likely use the same set of conformational rearrangements described for helical Dyn1 to deliver the energy from GTP hydrolysis to the membrane.

5. Dyn1-meGFP oligomers smaller than a single rung of 1-start Dynamin1 helix can produce membrane fission.

6. In the presence of GTP, subhelical Dynamin1 oligomers bound to a membrane template, curved or flat, can further oligomerize via G domains, using this alternative oligomerization pathway to form mechano-chemically active units.

Chapter 8:

Bibliography

Antonny, B., Burd, C., De Camilli, P., Chen, E., Daumke, O., Faelber, K., Ford, M., Frolov, V.A., Frost, A., Hinshaw, J.E., et al. (2016). Membrane fission by dynamin: what we know and what we need to know. EMBO J. *35*, 2270–2284.

Baehler, P.J., Biondi, R.M., van Bemmelen, M., Véron, M., and Reymond, C.D. (2002). Random insertion of green fluorescent protein into the regulatory subunit of cyclic adenosine monophosphate-dependent protein kinase. Methods Mol. Biol. *183*, 57–68.

Bashkirov, P. V., Akimov, S.A., Evseev, A.I., Schmid, S.L., Zimmerberg, J., and Frolov, V.A. (2008a). GTPase Cycle of Dynamin Is Coupled to Membrane Squeeze and Release, Leading to Spontaneous Fission. Cell *135*, 1276–1286.

Bashkirov, P.V., Kuzmin, P.I., Chekashkina, K., Arrasate, P., Vera Lillo, J., Shnyrova, A.V., and Frolov, V.A. (2020). Reconstitution and real-time quantification of membrane remodeling by single proteins and protein complexes. Nat. Protoc. *15*, 2443–2469.

Bigay, J., Deterre, P., Pfister, C., and Chabre, M. (1985). Fluoroaluminates activate transducin-GDP by mimicking the γ-phosphate of GTP in its binding site. FEBS Lett. *191*, 181–185.

Bigay, J., Deterre, P., Pfister, C., and Chabre, M. (1987). Fluoride complexes of aluminium or beryllium act on G-proteins as reversibly bound analogues of the gamma phosphate of GTP. EMBO J. *6*, 2907–2913.

Binns, D.D., Barylko, B., Grichine, N., Atkinson, M.A.L., Helms, M.K., Jameson, D.M., Eccleston, J.F., and Albanesi, J.P. (1999). Correlation between self-association modes and GTPase activation of dynamin. J. Protein Chem. *18*, 277–290.

Van Der Bliek, A.M., and Meyerowrtz, E.M. (1991). Dynamin-like protein encoded by the Drosophila shibire gene associated with vesicular traffic. Nature *351*, 411–414.

Brodsky, F.M., Chen, C.Y., Knuehl, C., Towler, M.C., and Wakeharn, D.E. (2001). Biological basket weaving: Formation and function of clathrin-coated vesicles. In Annual Review of Cell and Developmental Biology, pp. 517–568.

Campelo, F., and Malhotra, V. (2012). Membrane fission: The biogenesis of transport carriers. Annu. Rev. Biochem. *81*, 407–427.

Carr, J.F., and Hinshaw, J.E. (1997). Dynamin assembles into spirals under physiological salt conditions upon the addition of GDP and γ-phosphate analogues. J. Biol. Chem. *272*, 28030–28035.

Chalfie, M., Tu, Y., Euskirchen, G., Ward, W.W., and Prasher, D.C. (1994). Green fluorescent protein as a marker for gene expression. Science (80-.). *263*, 802–805.

Chang, Y.P., Pinaud, F., Antelman, J., and Weiss, S. (2008). Tracking bio-molecules in live cells using quantum dots. J. Biophotonics 287–298.

Chappie, J.S., Acharya, S., Leonard, M., Schmid, S.L., and Dyda, F. (2010). G domain dimerization controls dynamin's assembly-stimulated GTPase activity. Nature *465*, 435–440.

Chappie, J.S., Mears, J.A., Fang, S., Leonard, M., Schmid, S.L., Milligan, R.A., Hinshaw, J.E., and Dyda, F. (2011). A pseudoatomic model of the dynamin polymer identifies a hydrolysis-dependent powerstroke. Cell *147*, 209–222.

Chen, C., Fenk, L.A., and De Bono, M. (2013). Efficient genome editing in Caenorhabditis elegans by CRISPR-targeted homologous recombination. Nucleic Acids Res. *41*, e193.

Chen, M.S., Obar, R.A., Schroeder, C.C., Austin, T.W., Poodry, C.A., Wadsworth, S.C., and Vallee, R.B. (1991). Multiple forms of dynamin are encoded by shibire, a Drosophila gene involved in endocytosis. Nature *351*, 583–586.

Chen, Y.J., Zhang, P., Egelman, E.H., and Hinshaw, J.E. (2004). The stalk region of dynamin drives the constriction of dynamin tubes. Nat. Struct. Mol. Biol. *11*, 574–575.

Chernomordik, L. V., and Kozlov, M.M. (2003). Protein-Lipid Interplay in Fusion and Fission of Biological Membranes. Annu. Rev. Biochem. *72*, 175–207.

Cheung, A.Y., and De Vries, S.C. (2008). Membrane trafficking: Intracellular highways and country roads. Plant Physiol. 1451–1453.

Chiu, H., Schwartz, H.T., Antoshechkin, I., and Sternberg, P.W. (2013). Transgene-free genome editing in Caenorhabditis elegans using CRISPR-Cas. Genetics 1167–1171.

Chudakov, D.M., Matz, M. V., Lukyanov, S., and Lukyanov, K.A. (2010). Fluorescent proteins and their applications in imaging living cells and tissues. Physiol. Rev. 1103–1163.

Cocucci, E., Gaudin, R., and Kirchhausen, T. (2014). Dynamin recruitment and membrane scission at the neck of a clathrin-coated pit. Mol. Biol. Cell *25*, 3595–3609.

Colom, A., Redondo-Morata, L., Chiaruttini, N., Roux, A., and Scheuring, S. (2017a). Dynamic remodeling of the dynamin helix during membrane constriction. Proc. Natl. Acad. Sci. *114*, 5449–5454.

Colom, A., Redondo-Morata, L., Chiaruttini, N., Roux, A., and Scheuring, S. (2017b). Dynamic remodeling of the dynamin helix during membrane constriction. Proc. Natl. Acad. Sci. U. S. A. *114*, 5449–5454.

Conner, S.D., and Schmid, S.L. (2003). Regulated portals of entry into the cell. Nature 37–44.

Cook, T., Mesa, K., and Urrutia, R. (1996). Three dynamin-encoding genes are differentially expressed in developing rat brain. J. Neurochem. *67*, 927–931.

Cormack, B.P., Valdivia, R.H., and Falkow, S. (1996). FACS-optimized mutants of the green fluorescent protein (GFP). In Gene, pp. 33–38.

Danino, D., Moon, K.H., and Hinshaw, J.E. (2004). Rapid constriction of lipid bilayers by the mechanochemical enzyme dynamin. J. Struct. Biol. *147*, 259–267.

Dar, S., and Pucadyil, T.J. (2017). The pleckstrin-homology domain of dynamin is dispensable for membrane constriction and fission. Mol. Biol. Cell *28*, 152–160.

Dar, S., Kamerkar, S.C., and Pucadyil, T.J. (2015). A high-throughput platform for real-time analysis of membrane fission reactions reveals dynamin function. Nat. Cell Biol. *17*, 1588–1596.

Dar, S., Kamerkar, S.C., and Pucadyil, T.J. (2017). Use of the supported membrane tube assay system for real-time analysis of membrane fission reactions. Nat. Protoc. *12*, 390–400.

Digman, M.A., Dalal, R., Horwitz, A.F., and Gratton, E. (2008). Mapping the number of molecules and brightness in the laser scanning microscope. Biophys. J. *94*, 2320–2332.

Dunsing, V., Luckner, M., Zühlke, B., Petazzi, R.A., Herrmann, A., and Chiantia, S. (2018). Optimal fluorescent protein tags for quantifying protein oligomerization in living cells. Sci. Rep. *8*, 10634.

Edelstein, A., Amodaj, N., Hoover, K., Vale, R., and Stuurman, N. (2010). Computer control of microscopes using manager. Curr. Protoc. Mol. Biol. 14.20.1-14.20.17.

Efros, A.L., and Nesbitt, D.J. (2016). Origin and control of blinking in quantum dots. Nat. Nanotechnol. 661–671.

Espadas, J., Pendin, D., Bocanegra, R., Escalada, A., Misticoni, G., Trevisan, T., Velasco del Olmo, A., Montagna, A., Bova, S., Ibarra, B., et al. (2019). Dynamic constriction and fission of endoplasmic reticulum membranes by reticulon. Nat. Commun. *10*, 5327.

Faelber, K., Posor, Y., Gao, S., Held, M., Roske, Y., Schulze, D., Haucke, V., Noé, F., and Daumke, O. (2011). Crystal structure of nucleotide-free dynamin. Nature *477*, 556–560.

Faelber, K., Gao, S., Held, M., Posor, Y., Haucke, V., Noé, F., and Daumke, O. (2013). Oligomerization of dynamin superfamily proteins in health and disease. In Progress in Molecular Biology and Translational Science, pp. 411–443.

Ferguson, S.M., and De Camilli, P. (2012). Dynamin, a membrane-remodelling GTPase. Nat. Rev. Mol. Cell Biol. 75–88.

Ferguson, K.M., Lemmon, M.A., Schlessinger, J., and Sigler, P.B. (1994). Crystal structure at 2.2 Å resolution of the pleckstrin homology domain from human dynamin. Cell *79*, 199–209.

Ferguson, S.M., Brasnjo, G., Hayashi, M., Wölfel, M., Collesi, C., Giovedi, S., Raimondi, A., Gong, L.W., Ariel, P., Paradise, S., et al. (2007). A selective activity-dependent requirement for dynamin 1 in synaptic vesicle endocytosis. Science (80-.). *316*, 570–574.

Ford, M.G.J., Jenni, S., and Nunnari, J. (2011). The crystal structure of dynamin. Nature *477*, 561–566.

Frolov, V.A., Escalada, A., Akimov, S.A., and Shnyrova, A. V. (2015). Geometry of membrane fission. Chem. Phys. Lipids *185*, 129–140.

Fuhrmans, M., and Müller, M. (2015). Coarse-grained simulation of dynamin-mediated fission. Soft Matter *11*, 1464.

Galli, V., Sebastian, R., Moutel, S., Ecard, J., Perez, F., and Roux, A. (2017). Uncoupling of dynamin polymerization and GTPase activity revealed by the conformation-specific nanobody dynab. Elife *6*, e25197.

Goñi, F.M. (2014). The basic structure and dynamics of cell membranes: An update of the Singer-Nicolson model. Biochim. Biophys. Acta - Biomembr. 1467–1476.

Grassart, A., Cheng, A.T., Hong, S.H., Zhang, F., Zenzer, N., Feng, Y., Briner, D.M., Davis, G.D., Malkov, D., and Drubin, D.G. (2014a). Actin and dynamin2 dynamics and interplay during clathrin-mediated endocytosis. J. Cell Biol. *205*, 721–735.

Grassart, A., Cheng, A.T., Hong, S.H., Zhang, F., Zenzer, N., Feng, Y., Briner, D.M., Davis, G.D., Malkov, D., and Drubin, D.G. (2014b). Actin and dynamin2 dynamics and interplay during clathrin-mediated endocytosis. J. Cell Biol. *205*, 721–735.

Gudimchuk, N.B., Ulyanov, E. V., O'Toole, E., Page, C.L., Vinogradov, D.S., Morgan, G., Li, G., Moore, J.K., Szczesna, E., Roll-Mecak, A., et al. (2020). Mechanisms of microtubule dynamics and force generation examined with computational modeling and electron cryotomography. Nat.

Commun. *11*, 3765.

Higgins, M.K., and McMahon, H.T. (2005). In vitro reconstitution of discrete stages of dynamin-dependent endocytosis. Methods Enzymol. 597–611.

Hinshaw, J.E., and Schmid, S.L. (1995). Dynamin self-assembles into rings suggesting a mechanism for coated vesicle budding. Nature *374*, 190–192.

Hsieh, C.L., Spindler, S., Ehrig, J., and Sandoghdar, V. (2014). Tracking single particles on supported lipid membranes: Multimobility diffusion and nanoscopic confinement. J. Phys. Chem. B *118*, 1545–1554.

Hsieh, W.T., Hsu, C.J., Capraro, B.R., Wu, T., Chen, C.M., Yang, S., and Baumgart, T. (2012). Curvature sorting of peripheral proteins on solid-supported wavy membranes. Langmuir *28*, 12838–12843.

Huang, S.C.J., Artyukhin, A.B., Martinez, J.A., Sirbuly, D.J., Wang, Y., Ju, J.W., Stroeve, P., and Noy, A. (2007). Formation, stability, and mobility of one-dimensional lipid bilayers on polysilicon nanowires. Nano Lett. *7*, 3355–3359.

Jarin, Z., Pak, A.J., Bassereau, P., and Voth, G.A. (2021). Lipid-Composition-Mediated Forces Can Stabilize Tubular Assemblies of I-BAR Proteins. Biophys. J. *120*, 46–54.

Jass, J., Tjärnhage, T., and Puu, G. (2000). From liposomes to supported, planar bilayer structures on hydrophilic and hydrophobic surfaces: An atomic force microscopy study. Biophys. J. *79*, 3153–3163.

Jin, H., Ding, Y.H., Wang, M., Song, Y., Liao, Z., Newcomb, C.J., Wu, X., Tang, X.Q., Li, Z., Lin, Y., et al. (2018). Designable and dynamic single-walled stiff nanotubes assembled from sequence-defined peptoids. Nat. Commun. *9*, 270.

Jones, D.M., Alvarez, L.A., Nolan, R., Ferriz, M., Sainz Urruela, R., Massana-Muñoz, X., Novak-Kotzer, H., Dustin, M.L., and Padilla-Parra, S. (2017). Dynamin-2 Stabilizes the HIV-1 Fusion Pore with a Low Oligomeric State. Cell Rep. *18*, 443–453.

Kadosh, A., Colom, A., Yellin, B., Roux, A., and Shemesh, T. (2019). The tilted helix model of dynamin oligomers. Proc. Natl. Acad. Sci. U. S. A. *116*, 12845–12850.

Kenniston, J.A., and Lemmon, M.A. (2010). Dynamin GTPase regulation is altered by PH domain mutations found in centronuclear myopathy patients. EMBO J. *29*, 3054–3067.

Kiessling, V., Crane, J.M., and Tamm, L.K. (2006). Transbilayer effects of raft-like lipid domains in

asymmetric planar bilayers measured by single molecule tracking. Biophys. J. *91*, 3313–3326.

Kirchhausen, T. (1999). Adaptors for clathrin-mediated traffic. Annu. Rev. Cell Dev. Biol. 705–732.

Knight, J.D., and Falke, J.J. (2009). Single-molecule fluorescence studies of a PH domain: New insights into the membrane docking reaction. Biophys. J. *96*, 566–582.

Knight, J.D., Lerner, M.G., Marcano-Velázquez, J.G., Pastor, R.W., and Falke, J.J. (2010). Single molecule diffusion of membrane-bound proteins: Window into lipid contacts and bilayer dynamics. Biophys. J. *99*, 2879–2887.

Koenig, J.H., and Ikeda, K. (1989). Disappearance and reformation of synaptic vesicle membrane upon transmitter release observed under reversible blockage of membrane retrieval. J. Neurosci. *9*, 3844–3860.

Kong, L., Sochacki, K.A., Wang, H., Fang, S., Canagarajah, B., Kehr, A.D., Rice, W.J., Strub, M.P., Taraska, J.W., and Hinshaw, J.E. (2018). Cryo-EM of the dynamin polymer assembled on lipid membrane. Nature *560*, 258–262.

Kosaka, T., and Ikeda, K. (1983). Possible temperature-dependent blockage of synaptic vesicle recycling induced by a single gene mutation in drosophila. J. Neurobiol. *14*, 207–225.

Kozlovsky, Y., and Kozlov, M.M. (2003). Membrane fission: Model for intermediate structures. Biophys. J. *85*, 85–96.

Kunding, A.H., Mortensen, M.W., Christensen, S.M., and Stamou, D. (2008). A fluorescence-based technique to construct size distributions from single-object measurements: Application to the extrusion of lipid vesicles. Biophys. J. *95*, 1176–1188.

Lee, E., and De Camilli, P. (2002). Dynamin at actin tails. Proc. Natl. Acad. Sci. U. S. A. *99*, 161–166.

Lemmon, M.A., and Ferguson, K.M. (2000). Signal-dependent membrane targeting by pleckstrin homology (PH) domains. Biochem. J. 1–18.

LEMMON, M.A., and FERGUSON, K.M. (2000). Signal-dependent membrane targeting by pleckstrin homology (PH) domains. Biochem. J. *350*, 1–18.

Leonard, M., Doo Song, B., Ramachandran, R., and Schmid, S.L. (2005). Robust Colorimetric Assays for Dynamin's Basal and Stimulated GTPase Activities. In Methods in Enzymology, pp. 490–503.

Liu, Y.W., Lukiyanchuk, V., and Schmid, S.L. (2011a). Common membrane trafficking defects of disease-associated dynamin 2 mutations. Traffic *12*, 1620–1633.

Liu, Y.W., Neumann, S., Ramachandran, R., Ferguson, S.M., Pucadyil, T.J., and Schmid, S.L. (2011b). Differential curvature sensing and generating activities of dynamin isoforms provide opportunities for tissue-specific regulation. Proc. Natl. Acad. Sci. U. S. A. *108*, E234–E242.

Liu, Y.W., Mattila, J.P., and Schmid, S.L. (2013). Dynamin-Catalyzed Membrane Fission Requires Coordinated GTP Hydrolysis. PLoS One *8*, e55691.

Loerke, D., Mettlen, M., Yarar, D., Jaqaman, K., Jaqaman, H., Danuser, G., and Schmid, S.L. (2009). Cargo and dynamin regulate clathrin-coated pit maturation. PLoS Biol. *7*, e57.

Macia, E., Ehrlich, M., Massol, R., Boucrot, E., Brunner, C., and Kirchhausen, T. (2006). Dynasore, a Cell-Permeable Inhibitor of Dynamin. Dev. Cell *10*, 839–850.

Marks, B., Stowell, M.H.B., Vallis, Y., Mills, I.G., Gibson, A., Hopkins, C.R., and McMahon, H.T. (2001). GTPase activity of dynamin and resulting conformation change are essential for endocytosis. Nature *410*, 231–235.

Martinez Galvez, J.M., Garcia-Hernando, M., Benito-Lopez, F., Basabe-Desmonts, L., and Shnyrova, A. V. (2020). Microfluidic chip with pillar arrays for controlled production and observation of lipid membrane nanotubes. Lab Chip *20*, 2748–2755.

Mattila, J.P., Shnyrova, A. V., Sundborger, A.C., Hortelano, E.R., Fuhrmans, M., Neumann, S., Müller, M., Hinshaw, J.E., Schmid, S.L., and Frolov, V.A. (2015). A hemi-fission intermediate links two mechanistically distinct stages of membrane fission. Nature *524*, 109–113.

McConnell, H.M., Watts, T.H., Weis, R.M., and Brian, A.A. (1986). Supported planar membranes in studies of cell-cell recognition in the immune system. BBA - Rev. Biomembr. *864*, 95–106.

McQuilken, M., Mehta, S.B., Verma, A., Harris, G., Oldenbourg, R., and Gladfelter, A.S. (2015). Polarized fluorescence microscopy to study cytoskeleton assembly and organization in live cells. Curr. Protoc. Cell Biol. *67*, 4.29.1–4.29.13.

Mears, J.A., Ray, P., and Hinshaw, J.E. (2007). A Corkscrew Model for Dynamin Constriction. Structure *15*, 1190–1202.

Mehrotra, N., Nichols, J., and Ramachandran, R. (2014). Alternate pleckstrin homology domain orientations regulate dynamin-catalyzed membrane fission. Mol. Biol. Cell *25*, 879–890.

Merrifield, C.J., Feldman, M.E., Wan, L., and Almers, W. (2002). Imaging actin and dynamin

recruitment during invagination of single clathrin-coated pits. Nat. Cell Biol. *4*, 691–698.

Mettlen, M., Pucadyil, T., Ramachandran, R., and Schmid, S.L. (2009). Dissecting dynamin's role in clathrin-mediated endocytosis. In Biochemical Society Transactions, pp. 1022–1026.

Mettlen, M., Chen, P.H., Srinivasan, S., Danuser, G., and Schmid, S.L. (2018). Regulation of Clathrin-Mediated Endocytosis. Annu. Rev. Biochem. 871–896.

Meyer, T., Begitt, A., and Vinkemeier, U. (2007). Green fluorescent protein-tagging reduces the nucleocytoplasmic shuttling specifically of unphosphorylated STAT1. FEBS J. *274*, 815–826.

Misra, N., Martinez, J.A., Huang, S.C.J., Wang, Y., Stroeve, P., Grigoropoulos, C.P., and Noy, A. (2009). Bioelectronic silicon nanowire devices using functional membrane proteins. Proc. Natl. Acad. Sci. U. S. A. *106*, 13780–13784.

Montecinos-Franjola, F., Bauer, B.L., Mears, J.A., and Ramachandran, R. (2020). GFP fluorescence tagging alters dynamin-related protein 1 oligomerization dynamics and creates disassembly-refractory puncta to mediate mitochondrial fission. Sci. Rep. *10*, 14777.

Moradpour, D., Evans, M.J., Gosert, R., Yuan, Z., Blum, H.E., Goff, S.P., Lindenbach, B.D., and Rice, C.M. (2004). Insertion of Green Fluorescent Protein into Nonstructural Protein 5A Allows Direct Visualization of Functional Hepatitis C Virus Replication Complexes. J. Virol. *78*, 7400–7409.

Morlot, S., Galli, V., Klein, M., Chiaruttini, N., Manzi, J., Humbert, F., Dinis, L., Lenz, M., Cappello, G., and Roux, A. (2012). Membrane shape at the edge of the dynamin helix sets location and duration of the fission reaction. Cell *151*, 619–629.

Narayanan, R., Leonard, M., Byeong, D.S., Schmid, S.L., and Ramaswami, M. (2005). An internal GAP domain negatively regulates presynaptic dynamin in vivo: A two-step model for dynamin function. J. Cell Biol. *169*, 117–126.

Neumann, S., Pucadyil, T.J., and Schmid, S.L. (2013). Analyzing membrane remodeling and fission using supported bilayers with excess membrane reservoir. Nat. Protoc. *8*, 213–222.

Nissen, J., Gritsch, S., Wiegand, G., and Rädler, J.O. (1999). Wetting of phospholipid membranes on hydrophilic surfaces - Concepts towards self-healing membranes. Eur. Phys. J. B *10*, 335–344.

Nolan, R., Iliopoulou, M., Alvarez, L., and Padilla-Parra, S. (2018). Detecting protein aggregation and interaction in live cells: A guide to number and brightness. Methods 172–177.

Obar, R.A., Collins, C.A., Hammarback, J.A., Shpetner, H.S., and Vallee, R.B. (1990). Molecular

cloning of the microtubule-associated mechanochemical enzyme dynamin reveals homology with a new family of GTP-binding proteins. Nature *347*, 256–261.

Pannuzzo, M., McDargh, Z.A., and Deserno, M. (2018). The role of scaffold reshaping and disassembly in dynamin driven membrane fission. Elife *7*, e39441.

Praefcke, G.J.K., and McMahon, H.T. (2004). The dynamin superfamily: Universal membrane tubulation and fission molecules? Nat. Rev. Mol. Cell Biol. 133–147.

Prasher, D.C., Eckenrode, V.K., Ward, W.W., Prendergast, F.G., and Cormier, M.J. (1992). Primary structure of the Aequorea victoria green-fluorescent protein. Gene *111*, 229–233.

Pucadyil, T.J., and Schmid, S.L. (2008). Real-Time Visualization of Dynamin-Catalyzed Membrane Fission and Vesicle Release. Cell *135*, 1263–1275.

Pucadyil, T.J., and Schmid, S.L. (2010). Supported bilayers with excess membrane reservoir: A template for reconstituting membrane budding and fission. Biophys. J. *99*, 517–525.

Raimondi, A., Ferguson, S.M., Lou, X., Armbruster, M., Paradise, S., Giovedi, S., Messa, M., Kono, N., Takasaki, J., Cappello, V., et al. (2011). Overlapping Role of Dynamin Isoforms in Synaptic Vesicle Endocytosis. Neuron *70*, 1100–1114.

Ramachandran, R., and Schmid, S.L. (2008). Real-time detection reveals that effectors couple dynamin's GTP-dependent conformational changes to the membrane. EMBO J. *27*, 27–37.

Ramachandran, R., Surka, M., Chappie, J.S., Fowler, D.M., Foss, T.R., Song, B.D., and Schmid, S.L. (2007). The dynamin middle domain is critical for tetramerization and higher-order self-assembly. EMBO J. *26*, 559–566.

Ramachandran, R., Pucadyil, T.J., Liu, Y.W., Acharya, S., Leonard, M., Lukiyanchuk, V., and Schmid, S.L. (2009a). Membrane insertion of the pleckstrin homology domain variable loop 1 is critical for dynamin-catalyzed vesicle scission. Mol. Biol. Cell *20*, 4630–4639.

Ramachandran, R., Pucadyil, T.J., Liu, Y.-W., Acharya, S., Leonard, M., Lukiyanchuk, V., and Schmid, S.L. (2009b). Membrane Insertion of the Pleckstrin Homology Domain Variable Loop 1 Is Critical for Dynamin-catalyzed Vesicle Scission. Mol. Biol. Cell *20*, 4630–4639.

Rocheleau, J. V., Edidin, M., and Piston, D.W. (2003). Intrasequence GFP in class I MHC molecules, a rigid probe for fluorescence anisotropy measurements of the membrane environment. Biophys. J. *84*, 4078–4086.

Rosendale, M., Van, T.N.N., Grillo-Bosch, D., Sposini, S., Claverie, L., Gauthereau, I., Claverol, S.,

Choquet, D., Sainlos, M., and Perrais, D. (2019). Functional recruitment of dynamin requires multimeric interactions for efficient endocytosis. Nat. Commun. *10*, 4462.

Ross, J.A., Digman, M.A., Wang, L., Gratton, E., Albanesi, J.P., and Jameson, D.M. (2011). Oligomerization state of dynamin 2 in cell membranes using TIRF and number and brightness analysis. Biophys. J. *100*, L15–L17.

Roux, A., Koster, G., Lenz, M., Sorre, B., Manneville, J.B., Nassoy, P., and Bassereau, P. (2010). Membrane curvature controls dynamin polymerization. Proc. Natl. Acad. Sci. U. S. A. *107*, 4141–4146.

Sanii, B., Smith, A.M., Butti, R., Brozell, A.M., and Parikh, A.N. (2008). Bending membranes on demand: Fluid phospholipid bilayers on topographically deformable substrates. Nano Lett. *8*, 866–871.

Schindelin, J., Arganda-Carreras, I., Frise, E., Kaynig, V., Longair, M., Pietzsch, T., Preibisch, S., Rueden, C., Saalfeld, S., Schmid, B., et al. (2012). Fiji: An open-source platform for biological-image analysis. Nat. Methods 676–682.

Schmid, S.L., and Frolov, V.A. (2011). Dynamin: Functional Design of a Membrane Fission Catalyst. Annu. Rev. Cell Dev. Biol. *27*, 79–105.

Schmidt, T. (1996). Local stoichiometries determined by counting individual molecules. Anal. Chem. *68*, 4397–4401.

Schmidt, T., Schütz, G.J., Baumgartner, W., Gruber, H.J., and Schindler, H. (1996). Imaging of single molecule diffusion. Proc. Natl. Acad. Sci. U. S. A. *93*, 2926–2929.

Schütz, G.J., Schindler, H., and Schmidt, T. (1997). Single-molecule microscopy on model membranes reveals anomalous diffusion. Biophys. J. *73*, 1073–1080.

Seu, K.J., Pandey, A.P., Haque, F., Proctor, E.A., Ribbe, A.E., and Hovis, J.S. (2007). Effect of surface treatment on diffusion and domain formation in supported lipid bilayers. Biophys. J. *92*, 2445–2450.

Sever, S., Muhlberg, A.B., and Schmid, S.L. (1999). Impairment of dynamin's GAP domain stimulates receptor-mediated endocytosis receptor-mediated endocytosis. Nature *398*, 481–486.

Sever, S., Damke, H., and Schmid, S.L. (2000). Garrotes, springs, ratchets, and whips: Putting dynamin models to the test. Traffic 385–392.

Sever, S., Skoch, J., Newmyer, S., Ramachandran, R., Ko, D., McKee, M., Bouley, R., Ausiello, D., Hyman, B.T., and Bacskai, B.J. (2006). Physical and functional connection between auxilin and dynamin during endocytosis. EMBO J. *25*, 4163–4174.

Shnyrova, A. V, Bashkirov, P. V, Akimov, S. a, Pucadyil, T.J., Zimmerberg, J., Schmid, S.L., and Frolov, V. a (2013). Dynamin-driven membrane fission reveals catalytic principle of membrane remodeling. *339*, 1433–1436.

Shpetner, H.S., and Vallee, R.B. (1989). Identification of dynamin, a novel mechanochemical enzyme that mediates interactions between microtubules. Cell *59*, 421–432.

Shpetner, H.S., and Vallee, R.B. (1992). Dynamin is a GTPase stimulated to high levels of activity by microtubules. Nature *355*, 733–735.

Singh, S., and Bal, N.C. (2017). Membrane biophysics. In Introduction to Biomolecular Structure and Biophysics: Basics of Biophysics, pp. 183–204.

Song, B.D., Yarar, D., and Schmid, S.L. (2004). An Assembly-incompetent Mutant Establishes a Requirement for Dynamin Self-assembly in Clathrin-mediated Endocytosis in Vivo. Mol. Biol. Cell *15*, 2243–2252.

Sonnleitner, A., Schütz, G.J., and Schmidt, T. (1999). Free Brownian motion of individual lipid molecules in biomembranes. Biophys. J. *77*, 2638–2642.

Soumpasis, D.M. (1983). Theoretical analysis of fluorescence photobleaching recovery experiments. Biophys. J. *41*, 95–97.

Stachowiak, J.C., Schmid, E.M., Ryan, C.J., Ann, H.S., Sasaki, D.Y., Sherman, M.B., Geissler, P.L., Fletcher, D.A., and Hayden, C.C. (2012). Membrane bending by protein-protein crowding. Nat. Cell Biol. *14*, 944–949.

Sterling, S.M., Dawes, R., Allgeyer, E.S., Ashworth, S.L., and Neivandt, D.J. (2015). Comparison actin- and glass-supported phospholipid bilayer diffusion coefficients. Biophys. J. *108*, 1946–1953.

Stowell, M.H.B., Marks, B., Wigge, P., and McMahon, H.T. (1999). Nucleotide-dependent conformational changes in dynamin: Evidence for a mechanochemical molecular spring. Nat. Cell Biol. *1*, 27–32.

Subburaj, Y., Cosentino, K., Axmann, M., Pedrueza-Villalmanzo, E., Hermann, E., Bleicken, S., Spatz, J., and García-Sáez, A.J. (2015). Bax monomers form dimer units in the membrane that

further self-assemble into multiple oligomeric species. Nat. Commun. *6*, 8042.

Sundborger, A.C., Fang, S., Heymann, J.A., Ray, P., Chappie, J.S., and Hinshaw, J.E. (2014). A dynamin mutant defines a superconstricted prefission state. Cell Rep. *8*, 734–742.

Sweitzer, S.M., and Hinshaw, J.E. (1998). Dynamin undergoes a GTP-dependent conformational change causing vesiculation. Cell *93*, 1021–1029.

Takeda, T., Kozai, T., Yang, H., Ishikuro, D., Seyama, K., Kumagai, Y., Abe, T., Yamada, H., Uchihashi, T., Ando, T., et al. (2018). Dynamic clustering of dynamin-amphiphysin helices regulates membrane constriction and fission coupled with GTP hydrolysis. Elife *7*, e30246.

Takei, K., McPherson, P.S., Schmid, S.L., and Camilli, P. De (1995). Tubular membrane invaginations coated by dynamin rings are induced by GTP-γS in nerve terminals. Nature *374*, 186–190.

Takei, K., Haucke, V., Slepnev, V., Farsad, K., Salazar, M., Chen, H., and De Camilli, P. (1998). Generation of coated intermediates of clathrin-mediated endocytosis on protein-free liposomes. Cell *94*, 131–141.

Takei, K., Slepnev, V.I., Haucke, V., and De Camilli, P. (1999). Functional partnership between amphiphysin and dynamin in clathrin-mediated endocytosis. Nat. Cell Biol. *1*, 33–39.

Tamm, L.K., and McConnell, H.M. (1985). Supported phospholipid bilayers. Biophys. J. *47*, 105–113.

Traut, T.W. (1994). Physiological concentrations of purines and pyrimidines. Mol. Cell. Biochem. 1–22.

Urrutia, R., Henley, J.R., Cook, T., and McNiven, M.A. (1997). The dynamins: Redundant or distinct functions for an expanding family of related GTPases? Proc. Natl. Acad. Sci. U. S. A. 377–384.

Vámosi, G., Mücke, N., Müller, G., Krieger, J.W., Curth, U., Langowski, J., and Tóth, K. (2016). EGFP oligomers as natural fluorescence and hydrodynamic standards. Sci. Rep. *6*, 33022.

Velasco-Olmo, A., Ormaetxea Gisasola, J., Martinez Galvez, J.M., Vera Lillo, J., and Shnyrova, A.V. (2019a). Combining patch-clamping and fluorescence microscopy for quantitative reconstitution of cellular membrane processes with Giant Suspended Bilayers. Sci. Rep. *9*, 7255.

Velasco-Olmo, A., Ormaetxea Gisasola, J., Martinez Galvez, J.M., Vera Lillo, J., and Shnyrova, A. V. (2019b). Combining patch-clamping and fluorescence microscopy for quantitative

reconstitution of cellular membrane processes with Giant Suspended Bilayers. Sci. Rep. *9*, 7255.

Wang, X., Chen, Z., Mettlen, M., Noh, J., Schmid, S.L., and Danuser, G. (2020). DASC, a sensitive classifier for measuring discrete early stages in clathrin-mediated endocytosis. Elife *9*, e53686.

Warnock, D.E., Hinshaw, J.E., and Schmid, S.L. (1996). Dynamin self-assembly stimulates its GTPase activity. J. Biol. Chem. *271*, 22310–22314.

Van Der Wel, C., Vahid, A., ŠariĆ, A., Idema, T., Heinrich, D., and Kraft, D.J. (2016). Lipid membrane-mediated attraction between curvature inducing objects. Sci. Rep. *6*, 32825.

Yamamoto, E., Akimoto, T., Kalli, A.C., Yasuoka, K., and Sansom, M.S.P. (2017). Dynamic interactions between a membrane binding protein and lipids induce fluctuating diffusivity. Sci. Adv. *3*, e1601871.

Yolcu, C., Haussman, R.C., and Deserno, M. (2014). The Effective Field Theory approach towards membrane-mediated interactions between particles. Adv. Colloid Interface Sci. 89–109.

Yoshida, Y., Kinuta, M., Abe, T., Liang, S., Araki, K., Cremona, O., Di Paolo, G., Moriyama, Y., Yasuda, T., De Camilli, P., et al. (2004). The stimulatory action of amphiphysin on dynamin function is dependent on lipid bilayer curvature. EMBO J. *23*, 3483–3491.

Zacharias, D.A., Violin, J.D., Newton, A.C., and Tsien, R.Y. (2002). Partitioning of lipid-modified monomeric GFPs into membrane microdomains of live cells. Science (80-.). *296*, 913–916.

Zhang, L., and Granick, S. (2005). Lipid diffusion compared in outer and inner leaflets of planar supported bilayers. J. Chem. Phys. *123*, 211104.

Zhang, P., and Hinshaw, J.E. (2001). Three-dimensional reconstruction of dynamin in the constricted state. Nat. Cell Biol. *3*, 922–926.

Zhang, F., Moniz, H.A., Walcott, B., Moremen, K.W., Wang, L., and Linhardt, R.J. (2014). Probing the impact of GFP tagging on Robo1-heparin interaction. Glycoconj. J. *31*, 299–307.

Zhang, R., Lee, D.M., Jimah, J.R., Gerassimov, N., Yang, C., Kim, S., Luvsanjav, D., Winkelman, J., Mettlen, M., Abrams, M.E., et al. (2020). Dynamin regulates the dynamics and mechanical strength of the actin cytoskeleton as a multifilament actin-bundling protein. Nat. Cell Biol. *22*, 674–688.

Ziemba, B.P., and Falke, J.J. (2013). Lateral diffusion of peripheral membrane proteins on supported lipid bilayers is controlled by the additive frictional drags of (1) bound lipids and (2) protein domains penetrating into the bilayer hydrocarbon core. Chem. Phys. Lipids *172–173*,

67–77.

Ziemba, B.P., Knight, J.D., and Falke, J.J. (2012). Assembly of membrane-bound protein complexes: Detection and analysis by single molecule diffusion. Biochemistry *51*, 1638–1647.

Resumen y conclusiones

Introducción

Durante los últimos 30 años se ha estudiado el proceso de fisión de membrana mediada por las dinaminas. De entre todos los miembros de la superfamilia, las más estudiadas son las dinaminas clásicas. En mamíferos existen tres isoformas de las dinaminas clásicas, la dinamina 1, la dinamina 2 y la dinamina 3. Se encuentran distribuidas por todos los tipos celulares. La dinamina 1 se expresa principalmente en neuronas, la dinamina 2 se expresa en todos los tipos celulares y la dinamina 3 se encuentra expresada principalmente en testículos. Entre ellas destaca la dinamina 1, la principal isoforma utilizada para estudiar los procesos de remodelación de membrana y fisión.

Esta proteína actúa, principalmente, en los cuellos lipídicos de membrana que se forman entre la membrana madre y la vesícula naciente. La acción de la dinamina 1 en estas estructuras lipídicas provoca su escisión, liberando la vesícula naciente en el interior celular. De este modo finaliza el proceso conocido como endocitosis.

Desde su descubrimiento, en los años 90, se postuló que dicha proteína se enrolla alrededor de los cuellos tubulares, formando una hélice. Además, la dinamina 1 utiliza la energía proveniente de la hidrólisis del GTP para llevar a cabo un cambio conformacional en su estructura, necesario para finalizar el proceso de fisión.

La explicación para la formación de esta estructura helicoidal es que, para estimular la hidrólisis del GTP, la proteína necesita dimerizar a través de sus dominios GTPasa. Esto ocurre cuando la dinamina realiza una vuelta entera de la hélice.

Muchos modelos se han postulado para explicar el mecanismo por el cuál la dinamina, tras los cambios conformacionales en su estructura, es capaz de escindir los cuellos de membrana. Sin embargo, todos estos modelos presentan una serie de puntos en contra.

La hélice de dinamina también ha sido fundamental para explicar la serie de cambios conformacionales que se dan lugar tras la hidrólisis del GTP.

Aunque la hélice ha sido un gran instrumento para adquirir conocimientos acerca de su forma de actuación, en los últimos años se ha puesto en entredicho su necesidad para producir la fisión de las membranas.

Estudios muy recientes han demostrado que, durante el proceso de remodelación de membrana y cambio en la estructura de la hélice, ésta se ve comprometida. Dicho de otro modo, la hélice se fragmenta en pequeñas estructuras subhelicoidales.

Teniendo en cuenta los últimos descubrimientos acerca de la dinamina 1, los objetivos de la presente tesis fueron:

- Crear y caracterizar membranas lipídicas soportadas, combinadas con nanotecnología, para el estudio de la mecano-química de las unidades no helicoidales de la dinamina.
- Identificar la unidad mecano-química de la dinamina más pequeña.
- Estudiar la acción mecano-química de dichas unidades en membranas modelo tubulares y determinar si son autosuficientes para mediar la fisión de estas estructuras lipídicas.

Modelos lipídicos y determinación de la estequiometría de la proteína

Uno de los problemas que encontramos, a la hora de estudiar la acción no helicoidal de la proteína, fue su tendencia a oligomerizar alrededor de las membranas tubulares, formando grandes estructuras en forma de hélice. Por tanto, optamos por crear una serie de membranas modelo soportadas, inhibiendo de este modo la formación de dichas estructuras. Además, incluimos unas estructuras cilíndricas, los nanotubos peptídicos, en el soporte de las bicapas. De este modo, pudimos crear zonas localizadas de alta curvatura en nuestras membranas modelo. Finalmente, utilizando un sistema, previamente desarrollado en nuestro laboratorio, basado en unas esferas de sílice recubiertas de lípido. Al hacer rodar estas esferas sobre nuestras membranas modelo, conseguimos formar unos tubos lipídicos, imitando los cuellos tubulares alrededor de los cuales la dinamina actúa.

Una vez obtuvimos nuestras membranas modelo, procedimos a caracterizarlas. Una propiedad importante de las membranas lipídicas es su fluidez. Para determinar si nuestros modelos eran o no fluidos empleamos dos técnicas diferentes. La primera de ellas fue la recuperación de la fluorescencia tras el fotoblanqueo, la cual nos informa de la movilidad general del parche de lípido. Por otro lado, utilizamos unas esferas fluorescentes para determinar la movilidad, dentro del parche, de moléculas de lípido individuales. Ambas técnicas revelaron que las membranas modelo eran fluidas.

Finalmente, caracterizamos la topografía de dichas membranas mediante la técnica de microscopía de fuerza atómica. El escaneo de las muestras reveló la presencia de pequeños agujeros en las bicapas. Aunque no afectaron en la realización de los experimentos posteriores, es un factor importante a tener en cuenta para la interpretación de los resultados.

Además, realizamos una calibración de la fluorescencia de una única molécula de GFP, proteína fluorescente utilizada para marcar nuestra proteína de interés. Dicha calibración se realizó mediante diversas estrategias. La primera de ellas consistió en blanquear moléculas individuales de GFP. Para asegurar de que se trataba de moléculas individuales nos fijamos en el perfil de la fluorescencia de las partículas a lo largo del tiempo. El blanqueo de estas moléculas aparece como saltos a lo largo del tiempo. Calculando la fluorescencia total de las moléculas, previo blanqueo, obtuvimos nuestra calibración. También obtuvimos resultados similares de los saltos producidos durante el blanqueo. Por otro lado, tomando como referencia el número de dinaminas por vuelta, calculamos el número total de proteínas en una hélice de longitud conocida. Dividiendo la fluorescencia total de la hélice por el número de dinaminas, obtuvimos también un resultado similar a los previamente mencionados. Esta calibración nos sirvió para determinar el número de dinaminas presente en los experimentos posteriores.

Determinación de la maquinaria de fisión mínima

Como se ha mencionado previamente, la incubación de la proteína con los tubos lipídicos da lugar a la formación de estructuras helicoidales de gran tamaño. Por tanto, introdujimos una serie de cambios en la preparación de dichos tubos y en los tiempos de incubación para obtener oligómeros subhelicoidales. Reduciendo la cantidad de fosfoinositol bifosfato, principal lípido con el que interactúa la dinamina 1, y removiendo el exceso de proteína una vez entra en contacto con las membranas tubulares, pudimos formar dichas estructuras no helicoidales.

Utilizando la calibración, introducido en el apartado anterior, pudimos determinar el número de dinaminas presente en cada oligómero.

Tras la adición del GTP, observamos la ruptura de gran cantidad de tubos. Una vez cuantificado el tamaño de nuestras partículas, vimos que, en un 50% de los casos, estas fisiones fueron llevadas a cabo por complejos inferiores de 26 dinaminas, número mínimo para poder mediar una vuelta de hélice entera.

Autoensamblaje de la dinamina por la interfaz G2

Al tratarse de estructuras con un número menor de 26 dinaminas, estos complejos proteicos no pueden rodear las membranas tubulares, promoviendo la dimerización a través de los dominios GTPasa y estimulando la hidrólisis del GTP, requisito indispensable para poder mediar la ruptura

de los cuellos tubulares. Por tanto, estas estructuras debían presentar una vía alternativa para su autoensamblaje y estimulación de la hidrólisis del GTP.

Para este punto contamos con la colaboración del grupo del Dr. Aleksadr Noy (Livermore, EE. UU.). Mediante la técnica de microscopía de fuerza atómica de alta velocidad, pudieron resolver la formación de pequeñas estructuras de dinamina sobre los nanotubos peptídicos recubiertos de membrana. Cuando añadieron GTP observaron que los oligómeros de dinamina se desprendían de la superficie curva de las membranas soportadas. Al encontrarse inhibida su polimerización helicoidal, estas estructuras debían autoensamblarse por una vía alternativa a la clásica, a través del tallo de la proteína. Por tanto, concluimos que la única vía posible era a través de los propios dominios GTPasa, como los últimos estudios parecen indicar.

Además, dicha reorganización y desprendimiento de los oligómeros, fue observada mediante microscopía de fluorescencia.

Por otro lado, la pérdida de unión con la membrana no era exclusiva de las regiones curvadas de la muestra. También observamos dicho desprendimiento en las regiones planas de las bicapas. El análisis cuantitativo del tamaño de estas partículas reveló que las unidades superiores a los tetrámeros eran capaces de hidrolizar GTP y desprenderse de las membranas. Apoyando nuestras conclusiones previas.

Caracterización de la mecano-química de los oligómeros de dinamina 1

Finalmente, observamos que los oligómeros unidos a las partes planas de las membranas presentaban movilidad. Una característica importante de las dinaminas es la inserción parcial de una región de su dominio de unión en las bicapas. Esta inserción varía a lo largo del ciclo del GTP, siendo máxima en el estado de transición, momento en el cual el GTP se encuentra hidrolizado en GDP y Pi.

Estudios previos, realizados con el dominio de unión a membrana, revelaron que el aumento del número de puntos de contacto y la inserción de dicha región, provocan un aumento de la fricción entre la membrana y las proteínas, dando lugar a una disminución de la movilidad de las partículas. Por tanto, si dichas unidades son capaces de hidrolizar GTP su movilidad en las membranas se verá afectada.

El estudio comparativo de la difusión, de partículas de tamaño similar, en presencia o ausencia de nucleótidos, reveló que la movilidad de los oligómeros era significativamente diferente en

función de nucleótido añadido. Curiosamente, en presencia de un análogo del estado de transición, la movilidad se vio reducida drásticamente. Corroborando, de este modo, nuestra hipótesis previa.

Conclusiones

Las conclusiones del presente trabajo fueron las siguientes:

- El sistema utilizado para crear las membranas modelo permite su rápida y eficiente formación. Además, permite la creación de diferentes curvaturas y topologías en las bicapas.
- El cuanto de fluorescencia, obtenido mediante nuestra calibración a tres bandas, apoya nuestro procedimiento de contaje de moléculas.
- El etiquetado de la dinamina 1 con GFP no altera significativamente sus actividades GTPasa y de remodelación de membrana.
- Los oligómeros de dinamina 1 más pequeños que una vuelta de hélice son capaces de producir la fisión de las membranas.
- La simetría cilíndrica de la dinamina 1 no es necesaria para estimular su actividad GTPasa.
- En presencia de GTP, las subunidades de dinamina 1 pueden dimerizar a través de sus dominios GTPasa, utilizando esta vía alternativa para formar unidades mecano-químicamente activas.
- Nuestros resultados parecen indicar que las unidades de dinamina 1 no helicoidales utilizan el mismo conjunto de cambios conformacionales, descritos para las hélices, para enviar la energía de la hidrólisis del GTP a las membranas.

Acknowledgments

I would like to thank Vadim for his guidance during the first steps of my career as a researcher. I cannot say it has been easy, but your support pushed me to reach limits I could not imagine when I started this journey. I would also like to thank Anna for contributing your ideas during these past 4 years and for showing me that sharing science can be joyful.

I cannot forget Alex and Sergi, who hosted me in their teams. As well as Yuliang and Irene, who taught me during my visit.

I thank Aritz his kind help performing AFM experiments.

Finally, I would like to express my sincere gratitude to all members of the laboratory for their support, from those present when I joined the group to those who have shared this experience with me. Javi, Juanma and Pedro, we are almost done! I wish you all the best in your nearest future. Julene, I think the rest of the guys will agree with me when I say that you are an extremely hard worker. You are a fundamental piece of this group.

Thank you all, it has been a pleasure to be part of this team.